

Dissertation

submitted to the
Combined Faculty of Natural Sciences and Mathematics
of the Ruperto-Carola University of Heidelberg, Germany
for the degree of

Doctor of Natural Sciences

Put forward by

Johannes Sebastian Breitling

born in: Friedrichshafen, Germany

Oral examination: June 15, 2020

MR-based protein imaging of the human brain by means of dualCEST

Referees: Prof. Dr. Peter Bachert
Prof. Dr. Lothar R. Schad

MR-based protein imaging of the human brain by means of dualCEST

Chemical exchange saturation transfer (CEST) is an emerging magnetic resonance imaging (MRI) technique enabling indirect detection of low-concentration cellular compounds in living tissue by their magnetization transfer with water. In particular, protein-attributed CEST signals have been shown to provide valuable diagnostic information for various diseases. While conventional CEST approaches suffer from confounding signals from metabolites and macromolecules, the novel dual-frequency irradiation CEST (dualCEST) technique enables increased protein specificity by selectively detecting the intramolecular spin-diffusion. However, application of this technique has so far been limited to spectroscopic investigations of model solutions at ultrahigh magnetic field strengths.

In this thesis, dualCEST was translated to a clinical whole-body MR scanner, enabling protein imaging of the human brain. To this end, several methodological developments were implemented and optimized: (i) improved dual-frequency pulses for signal preparation, (ii) a fast and robust volumetric image readout, (iii) a weighted acquisition scheme, and (iv) an adaptive denoising technique. The resulting improvements are not limited to dualCEST but are relevant for the research field of CEST-MRI in general. Extensive measurements of biochemical model solutions and volunteers demonstrated the protein specificity and reproducibility of dualCEST-MRI. The clinical applicability was verified in pilot studies with tumor and Alzheimer's patients.

MR-basierte Protein-Bildgebung des menschlichen Gehirns mittels dualCEST

Chemical Exchange Saturation Transfer (CEST) ist eine neuartige Magnetresonanz-Bildgebungstechnik, welche eine indirekte Detektion von niedrig konzentrierten organischen Verbindungen in lebendem Gewebe anhand ihres Magnetisierungstransfers mit Wasser ermöglicht. Insbesondere mit Proteinen in Verbindung gebrachte CEST-Signale konnten dabei bereits wertvolle diagnostische Informationen für etliche Erkrankungen liefern. Während konventionelle CEST-Ansätze durch überlagernde Signale von Metaboliten und Makromolekülen beeinträchtigt werden, erreicht die neue *Dual-Frequency Irradiation CEST* (dualCEST)-Technik eine erhöhte Proteinspezifität mittels selektiver Detektion von intramolekularen Spindiffusionsprozessen. Eine Anwendung der neuen Technik war bisher jedoch nur für spektroskopische Untersuchungen von Modellösungen bei ultrahohen Magnetfeldstärken möglich.

In dieser Arbeit wurde die dualCEST-Technik nun erstmals auf einen klinischen Ganzkörper-tomographen übertragen, so dass eine Proteinbildgebung des menschlichen Gehirns möglich ist. Zu diesem Zwecke wurden methodische Weiterentwicklungen für alle relevanten Teilbereiche der Technik implementiert und optimiert: (i) verbesserte Sättigungspulse für die Signalpräparation, (ii) eine schnelle und robuste 3D Bildauslese, (iii) eine gewichtete Bildaufnahme, sowie (iv) einen Algorithmus zur Rauschunterdrückung. Die erzielten Fortschritte sind dabei nicht auf dualCEST beschränkt, sondern relevant für das CEST-Forschungsfeld im Allgemeinen. Umfangreiche Untersuchungen an biochemischen Modellösungen und Probanden stellten dabei die Spezifität und Reproduzierbarkeit der dualCEST-Bildgebung unter Beweis. Die klinische Anwendbarkeit und Leistungsfähigkeit wurde abschließend im Rahmen erster Pilotstudien von Hirntumor- und Alzheimerpatienten erprobt.

Contents

List of Abbreviations	ix
1 Introduction	1
1.1 MRI	2
1.2 CEST	3
1.3 DualCEST	7
2 Publications	11
Thematic overview over the individual publications	11
I Dual-frequency irradiation CEST-MRI of endogenous bulk mobile proteins	17
II Relaxation-compensated APT and rNOE CEST-MRI of human brain tumors at 3 T	33
III Adaptive denoising for chemical exchange saturation transfer MR imaging	47
IV Optimized dualCEST-MRI for imaging of endogenous bulk mobile proteins in the human brain	65
3 Discussion	79
3.1 Translation from NMR spectrometer to clinical scanner	79
3.2 In vivo application	86
4 Conclusion	93
Appendices	95
A Two-stage denoising of CEST-MRI data by principal component analysis of spectral groups	95
B Steady-state CEST-MRI using a reduced saturation period	99
C Application to patients with Alzheimer's disease	103
Bibliography	107
List of Scientific Contributions	117
Acknowledgements	

List of Abbreviations

B_0	static magnetic field strength
B_1	amplitude of RF field
$CI_{95\%}$	95% confidence interval
t_{sat}	saturation length
T	saturation crosstalk
$T_{protein}$	isolated saturation crosstalk of mobile proteins
T_1	longitudinal relaxation time
T_2	transversal relaxation time
APT	amide proton transfer
AREX	apparent exchange-dependent relaxation rate
CEST	chemical exchange saturation transfer
CSF	cerebral spinal fluid
CT	computed tomography
DC	duty cycle
dualCEST	dual-frequency irradiation CEST
DWI	diffusion weighted MRI
fMRI	functional MRI
GM	gray matter
ICC	intraclass correlation coefficient
MR	magnetic resonance
MRI	magnetic resonance imaging
MRS	in vivo magnetic resonance spectroscopy
NMR	nuclear magnetic resonance
NOE	nuclear Overhauser effect

List of Abbreviations

PCA	principal component analysis
PET	positron emission tomography
RF	radio frequency
rNOE	exchange-relayed nuclear Overhauser effect
SNR	signal-to-noise ratio
SPECT	single-photon emission computed tomography
ssMT	semi-solid magnetization transfer
US	ultrasonography
WM	white matter

1 Introduction

Medical imaging encompasses different imaging modalities and processes to examine the human body in order to diagnose or monitor medical conditions. Each type of technology contributes different information about the examined part of the body, related to possible disease, injury, or the effectiveness of medical treatment.^{1,2} In general and on a rough level they can be divided into primarily anatomical modalities such as computed tomography (CT), ultrasonography (US) and magnetic resonance imaging (MRI), investigating structural and morphological details of the patients body, and functional imaging modalities such as positron emission tomography (PET) and single-photon emission computed tomography (SPECT), providing information about the physiological activity within a certain tissue or organ.

In this context, the distinguishing feature of MRI compared to many other imaging modalities is its multiplicity. Besides the excellent soft-tissue contrast utilized for morphological imaging, MRI provides a wide range of possibilities for functional imaging including the visualization of blood flow and diffusion processes,^{3,4} the mapping of activated brain areas⁵ and the spectroscopic investigation of the chemical composition of tissues.⁶ However, conventional spectroscopic imaging techniques have so far been impeded from entering daily clinical practice due to limitations in the sensitivity, spatial resolution, and scanning time.

Chemical exchange saturation transfer (CEST)-MRI has emerged as an alternative solution for the imaging of low-concentrated organic compounds in living tissue such as proteins, peptides and various other metabolites, e.g. creatine and glutamate.⁷⁻⁹ In particular CEST signals attributed to proteins have been shown to provide valuable diagnostic information for a variety of diseases, in particular cancer and Alzheimer's.¹⁰⁻¹⁵ However, in living tissue, various CEST signals from different cellular compounds such as proteins,^{10,11,16,17} metabolites,¹⁸⁻²² lipids^{12,23} and semi-solid macromolecular structures²⁴⁻²⁶ are superimposing indistinguishably. Moreover, these signals depend on multiple physiological parameters, in particular pH and temperature.^{10,27,28} Although by now several attempts have been made to highlight the signal contribution of proteins by adjusting the CEST pulse scheme, i.e., the saturation amplitude or the pulse timing,²⁹⁻³¹ to date an exclusive assignment of the observed effects to solely proteins is practically impossible.

Recently, dual-frequency irradiation CEST (dualCEST)³² has been introduced as a novel technique to overcome these selectivity limitations. This method enables the selective detection of endogenous proteins in living tissue without contributions of other saturation transfer effects by utilizing the coupling between different CEST signals as a distinguishing feature. In the preceding master thesis³³ the approach was extensively investigated in spectrometer

1 Introduction

measurements of model solutions at ultra-high magnetic fields strengths, confirming the exclusive dependency on the concentration, molecular size and folding state of the mobile proteins. These results substantiate the potential of dualCEST as a promising tool for the detection of aberrant proteomes in vivo, and thus novel diagnostic imaging modality.

The aim of this thesis was therefore the translation of the dualCEST technique to a clinical whole-body scanner (i.e. with a static magnetic field strength $B_0 \leq 3$ T) to enable protein imaging of the human brain. To achieve this goal, several methodological improvements were developed and applied: (i) Implementation of dual-frequency pulses allowed for an improved signal preparation, which was additionally refined by (ii) a newly developed weighted acquisition scheme allowing for an optimal use of the limited examination time. The optimized signal preparation was subsequently combined with (iii) a fast and robust volumetric image readout, which moreover facilitated the application of (iv) a newly developed denoising technique. Following the methodological developments, extensive measurements of biochemical model solutions and volunteers confirmed the protein specificity of dualCEST-MRI and demonstrated its reproducibility. Furthermore, applicability in a clinical setting was demonstrated in pilot studies with brain tumor and Alzheimer's patients.

The following explanations summarize the basic principles of MRI, CEST and dualCEST, introducing the necessary concepts and methodologies for this study and thereby setting the general conceptual framework.

1.1 MRI

Following the discovery of the proton spin in the Stern-Gerlach experiment in 1922,³⁴ Isidor I. Rabi and co-workers³⁵ described and measured in 1938 for the first time nuclear magnetic resonance. By using oscillating magnetic fields they were able to induce transitions between the discrete energy levels in a beam of molecules traversing a static magnetic field. In 1946, based on these observations, the research groups of Felix Bloch³⁶ and Edward M. Purcell³⁷ were – independently of each other – able to demonstrate nuclear magnetic resonance in condensed matter. In the liquid phase, nuclear magnetic resonance (NMR) experiments are well described by the empirical Bloch equations,³⁶ which introduce two important kinetic parameters: the longitudinal relaxation time T_1 and the transversal relaxation time T_2 . The discovery of the chemical environment dependent dispersion of the nuclear spin resonance frequency^{38,39} gave rise to the field of NMR spectroscopy. This important research tool, utilized in physics and biochemistry, allows information about the electronic structure, binding characteristics, functional groups, and chemical environment of molecules to be obtained by analyzing their chemical shifts in the NMR spectrum.

In 1973 Paul C. Lauterbur⁴⁰ and Sir Peter Mansfield⁴¹ demonstrated that by applying additional magnetic field gradients the spatial distribution of nuclear spins can be encoded within the magnetic resonance (MR) signal, hence facilitating imaging. In the following years magnetic resonance imaging, utilizing the dominant NMR signal of free water protons, has proven to be one of the most versatile imaging techniques in particular for

diagnostic medicine and biomedical research. This success can be explained by the beneficial combination of two factors: the very large abundance of water protons in living tissue (e.g. 44 M in human brain grey matter) and the strong dispersion of T_1 and T_2 in different tissues entailing a unique soft tissue contrast. The latter resulted in T_1 - and T_2 -weighted MRI becoming the workhorse for visualizing the human anatomy and detecting pathologic alterations.

In addition to these conventional relaxation-weighted imaging contrasts of free water protons – providing mainly information about structural and macroscopic tissue properties – several other methods have been developed to provide insights on various scales and levels of living tissue. Functional MRI (fMRI) for example uses differences in the magnetic properties of oxygen-rich and oxygen-depleted blood to measure neural activity in the brain.⁵ Another example is diffusion weighted MRI (DWI), which allows the diffusion processes of water molecules to be mapped, revealing microscopic tissue properties such as the cellular environment.^{3,4} Moreover, NMR spectroscopy applied to living tissue (in vivo magnetic resonance spectroscopy, MRS) allows to obtain a manifold of biochemical information such as relative concentrations of organic compounds and metabolic turnover as well as physiological parameters like intra- and extracellular pH.^{6,42} However, as the abundance of the compounds and nuclear spins of interest are so much smaller compared to water protons (i.e. by a factor of 10^6), molecular and non-proton MRI in vivo are challenging in terms of signal-to-noise ratio (SNR), spatial resolution and scanning time.

1.2 CEST

Another alternative technique allowing to assess the molecular and biochemical level in vivo is CEST-MRI,^{7-9,43} which combines the spectral selectivity of MRS with the high spatial resolution and SNR of conventional MRI. To achieve this, the imaging contrast utilizes the chemical exchange process between water protons and protons of nonequivalent chemical environment such as labile protons in molecules. Application of a frequency selective radio frequency (RF) irradiation on-resonant with the solute protons of interest, results in a saturation of the respective spin states, and hence in a destruction of the net magnetization. The perpetual chemical exchange transfers this saturation to the water magnetization resulting in an attenuation of the water signal. In view of the low solute concentration (typically micro- to millimolar) a single transfer of saturation would affect the much larger water proton pool (on the order of 100 M) only insignificantly. However, as the water proton pool is so much larger, each exchanging saturated solute proton is subsequently replaced by an unsaturated water proton, which is in turn again saturated. For a sufficiently fast enough exchanging solute (residence time in milliseconds range) and long enough saturation time t_{sat} (in the range of seconds) this results in an accumulation of the saturation over time and thereby substantial (negative) signal enhancement on the order of the exchange rate (i.e. an amplification factor of 10 to 1000). Subsequent acquisition of the modified water proton signal M_{sat} yields therefore an indirect imaging of the low-concentration solutes (Figure 1A).

1 Introduction

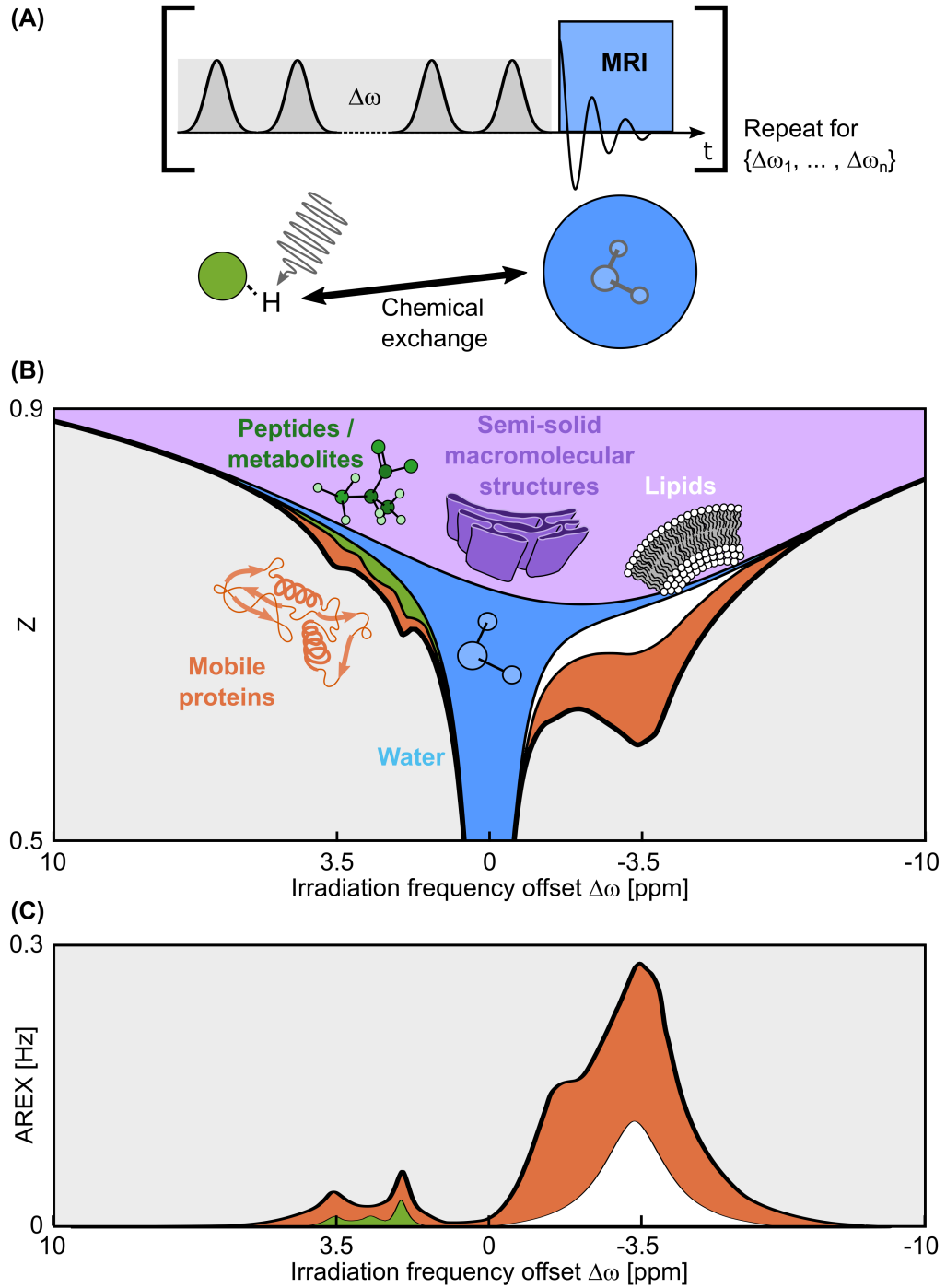


Figure 1: The CEST experiment. (A) Selective RF saturation of the solute and subsequent saturation transfer via the chemical exchange is followed by the acquisition of the modified water signal. (B) Repetition for multiple frequency offsets yields the Z-spectrum, which comprises in vivo contributions of various different cellular compounds. (C) Appropriate evaluation (AREX) allows to some extent isolating CEST signals from other confounding effects. Subfigure B is adapted from [32].

Repetition of the experiment for multiple frequency offsets ($\Delta\omega$) relative to the water Larmor frequency, and normalization with the equilibrium water magnetization M_0 yields a saturation spectrum for each image pixel, the so-called Z-spectrum.

$$Z(\Delta\omega) = \frac{M_{sat}(\Delta\omega)}{M_0} \quad (1)$$

Z-spectra acquired in vivo comprise contributions of various different effects (Figure 1B), which are briefly discussed in the following.

- The most prominent spectral feature is the symmetric collapse of the signal at 0 ppm caused by saturating the water proton pool itself, which is referred to as direct water saturation. The effect is well described by the Bloch equations and decreases rapidly with the off-resonance.^{44,45}
- In the positive frequency range ($\Delta\omega > 0$ ppm) selective resonances of chemical exchange effects can be observed, attributed to the labile protons of functional groups, such as amide (-NH), amine (-NH₂) and hydroxyl (-OH) groups. Although the chemical shift and therefore the resonance frequency is depending on the specific proton site in the molecule, an unambiguous assignment of CEST signals to specific compounds in vivo is impossible. However, prior knowledge about the tissue composition, the expectable exchange rates, chemical shifts and relaxation times allows to a certain degree to correlate the observed effects with the compounds in question.⁴⁵
- The dipolar interactions between close nuclear spins – the so called nuclear Overhauser effect (NOE)⁴⁶ – constitutes another magnetization transfer pathway besides the physical transfer of protons through space. For proteins and other large biomolecules with a high proton density, this coupling results in the transfer of magnetization throughout the whole molecule, referred to as spin diffusion. Moreover, this entails the magnetization transfer from non-exchanging covalent bound protons to protons of a chemically exchanging group. A subsequent inter-molecular exchange can relay the magnetization to the water pool. This sequence of processes is therefore referred to as exchange-relayed nuclear Overhauser effect (rNOE) and is the dominant dipolar-coupling-based exchange with water protons.^{23,47} In the in vivo Z-spectrum the rNOE of aliphatic and aromatic protons can be observed in the range from -2 to -5 ppm and 1 to 4 ppm respectively.
- The semi-solid magnetization transfer (ssMT) is a non-selective effect, which can be observed across a very large frequency range in the Z-spectrum. It summarizes several different magnetization transfer pathways to the protons in free water molecules. The ssMT is mainly attributed to motion restricted water protons bound to the macromolecular matrix, as well as protons bound directly to the surface of these macromolecules.^{25,47} The macromolecular matrix is composed of large and semi-solid components of the cell, e.g. cell membranes, surface proteins and the cytoskeleton. Of note, the strongly broadened resonance corresponds to the short T_2 times, i.e. in the order of a few μ s, resulting from the solid-state-like character of the macromolecular matrix.

1 Introduction

By now CEST imaging has been reported to be able to detect a variety of different diluted solutes including proteins and peptides,^{10,10,11,17} creatine,^{19,48,49} glutamate,¹⁸ lactate,⁵⁰ glucose,^{21,22} myo-inositol,⁵¹ and exogenous contrast agents such as iopamidol.^{52,53} In particular the CEST signals attributed to proteins have been shown to provide valuable diagnostic information – namely the amide proton transfer (APT)¹⁰ signal originating from the amide protons in peptide bonds in the backbone of mobile proteins, resonating at around 3.5 ppm, and the rNOE¹² signal of aliphatic protons, resonating at around -3.5 ppm. Potential applications range from tumor detection,^{54,55} assessment of tumor malignancy,^{56,57} and differentiation of radiation necrosis and tumor progression^{58–60} to the detection of neurodegenerative diseases such as Alzheimer’s,^{14,15} Parkinson’s,⁶¹ and multiple sclerosis.⁶² Although these approaches are very promising, the underlying origin is not completely understood. Exclusive assignment of the observed effects to proteins is prevented by the signal superposition of various cellular compounds in living tissue, i.e. proteins, metabolites and small peptides, lipids and semi-solid macromolecular structures (Figure 1B). These signals are moreover affected by tissue relaxation properties (T_1 and T_2) and depend on the exchange rate, which is in turn determined by physiological conditions, in particular pH and temperature.^{10,27,28} The improvement of specificity has therefore become one of the most important issues in the research field of CEST-MRI.

A first step towards the selective measurement of quantitative CEST signals was induced by deriving a full analytical model of the Z -spectrum. The magnetization dynamics of two coupled spin pools during an RF irradiation are described by the Bloch-McConnell equations.⁶³ In this context, the rotating frame of reference is defined by the off-resonance $\Delta\omega$ and amplitude B_1 of the RF irradiation. Solving the Bloch-McConnell equations by an eigenspace approach and considering only the significant remaining contribution, the smallest eigenvalue λ_1 , allowed the reduction to an one-dimensional system, which can be solved straightforward.^{45,64,65} Moreover, it was shown that λ_1 can be approximated by the longitudinal relaxation rate in the rotating frame $R_{1\rho} \approx -\lambda_1$, which is the sum of the effective relaxation rate due to the direct water saturation R_{eff} and the sum of all exchange-dependent relaxation rates of solute pools i :^{64,65}

$$R_{1\rho}(\Delta\omega) = R_{eff} + \sum_i R_{ex,i} \quad (2)$$

with $R_{eff} = R_1 \cos^2 \theta + R_2 \sin^2 \theta$, the water relaxation rates $R_1 = 1/T_1$ and $R_2 = 1/T_2$, and the tilt angle of the effective field $\theta = \tan^{-1}(\gamma B_1/\Delta\omega)$. In other words, the chemical exchange or dipolar interactions can be understood as an additional spectral selective relaxation pathway in the rotating frame. The Z -spectrum after an irradiation with duration t_{sat} can then be described by

$$Z(\Delta\omega) = Z^{ss} + (Z_{init} - Z^{ss})e^{-t_{sat} \cdot R_{1\rho}} \quad (3)$$

where Z_{init} is the initial magnetization and the steady-state magnetization Z^{ss} is given by

$$Z^{ss}(\Delta\omega) = \frac{R_1 \cos^2 \theta}{R_{1\rho}}. \quad (4)$$

Based on this analytical model, the isolation of individual CEST effects becomes possible by computing the apparent exchange-dependent relaxation rate (AREX):⁶⁶

$$AREX = R_1 \cdot \left(\frac{1}{Z} - \frac{1}{Z_{ref}} \right) = \frac{R_{ex}}{\cos^2 \theta} \quad (5)$$

where Z_{ref} is a reference spectrum containing all contributions but the solute of interest, typically obtained by spectral fitting. Besides the term $\cos^2 \theta$, AREX is a quantitative metric allowing to obtain the relaxation rate of a single CEST effect (Figure 1C), corrected for other influences of the direct water saturation, T_1 relaxation and confounding signal contributions, i.e. ssMT.

Although this sophisticated approach addresses some of the challenges and issues of CEST-MRI, a selective detection of one specific CEST compound without signal contributions from other compounds in vivo is still impossible. The AREX metric depends crucially on obtaining an appropriate reference spectra; however, in living tissue it is typically only possible to take into account the prevalent contributions of the direct water saturation and the ssMT, thus preventing a further isolation of signal contributions (Figure 1C). This is even more critical for a possible application at clinical MR systems with lower magnetic field strength, which do not allow to resolve distinct peaks anymore due to the decreased spectral resolution. In addition, it would be desirable to obtain a protein signal without dependency on physiological parameters, i.e. pH and temperature. This would allow to assign observed changes in disease states to actual alterations of the proteome, i.e. changes in the concentration, folding state or molecular size of proteins. Therefore there is still a need for novel approaches and experiments to enable the selective detection of protein CEST signals.

1.3 DualCEST

Recently a new CEST-based technique was introduced for the detection of endogenous bulk mobile proteins, allowing to overcome the aforementioned specificity limitations by introducing of a novel kind of selectivity: the detection of the coupling between different CEST signals. The dualCEST approach was first mentioned by Steffen Goerke,⁶⁷ subsequently investigated in the preceding master thesis of the author³³ and finally comprehensively presented in Goerke S, Breitling J, et al.³² The latter includes as well the first results of this dissertation. The following explanations summarize the most important findings of these previous works.

The dualCEST approach extends, to this end, the conventional CEST experiment by an additional interleaved RF saturation pulse at a second frequency offset $\Delta\omega_c$ (Figure 2A). In doing so, both frequency offsets are simultaneously saturated. Repetition of the sequence for multiple such frequency offset pairs effectively results in the acquisition of a two-dimensional Z-spectrum $Z(\Delta\omega, \Delta\omega_c)$ (Figure 2B), which features contributions of CEST effects resonating at either one of the two frequency offsets. For this, the measured effect will depend on

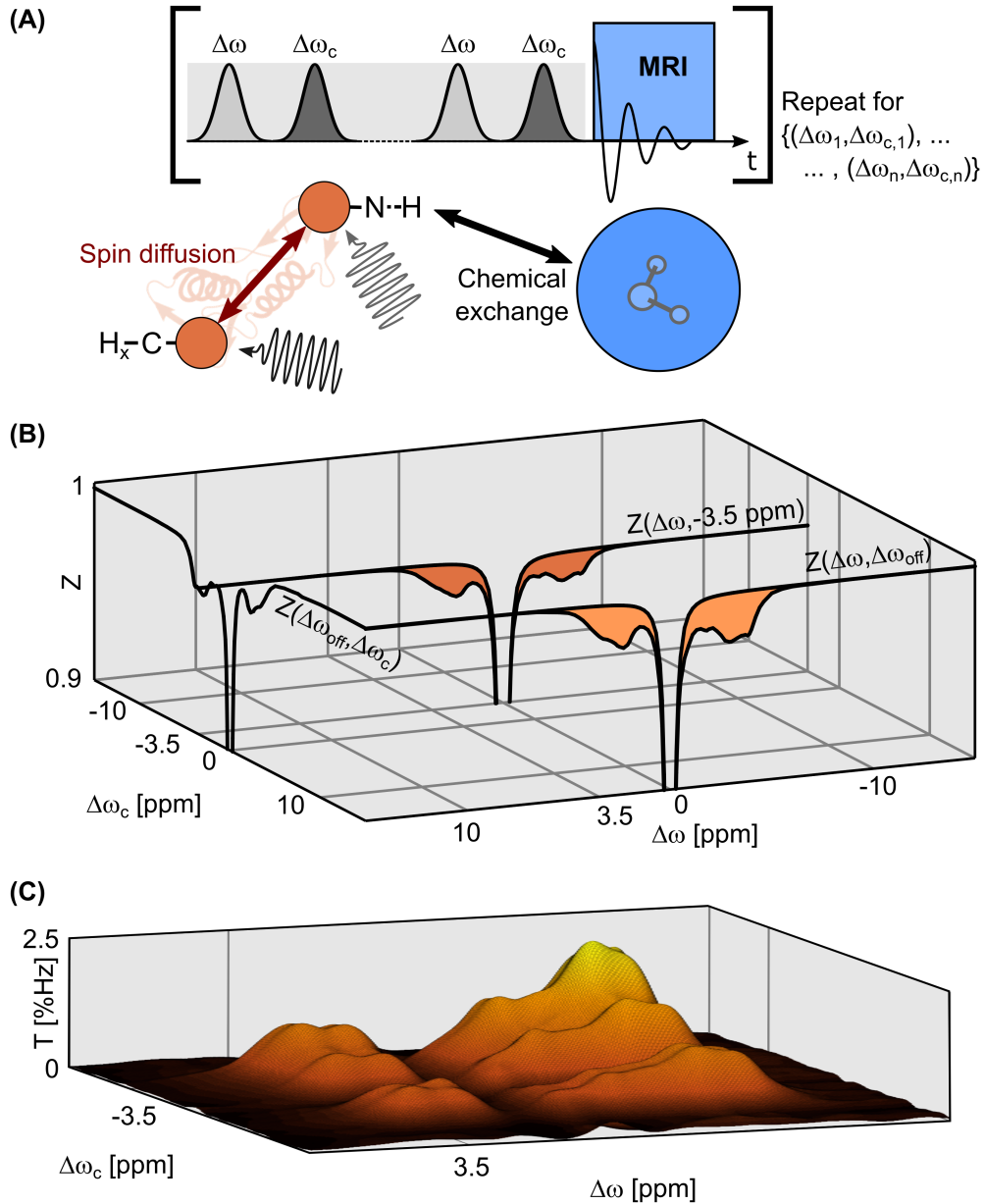


Figure 2: The dualCEST experiment. (A) Extension of the conventional CEST sequence by an additional interleaved saturation pulse with a second frequency allows to simultaneously saturate a pair of frequency offsets. (B) Repetition for multiple pairs yields a two-dimensional Z-spectrum, visualized by three representative profiles, i.e. Z-spectra. The coupling of CEST signals, e.g. the intra-molecular spin diffusion in proteins, results in a reduction of the measured joint CEST effect as compared to uncoupled resonances. (C) The impact of the coupling (T) can be isolated by comparison with the (inverse) sum of the individual CEST effects. Specificity to proteins is ultimately achieved by setting the frequency offsets to the positive and negative frequency range. Subfigure C is adapted from [67].

whether the CEST signals resonating at $\Delta\omega$ and $\Delta\omega_c$ are coupled, i.e. connected by a magnetization transfer pathway, or not. For uncoupled CEST signals the individual effects just add up linearly, for example in the case of lipids and metabolites. In contrast, a coupling of CEST signals results effectively in a reduction of the measured joint CEST effect. For proteins, such a coupling is given by the intra-molecular spin-diffusion underlying the rNOE. As explained earlier, this process is responsible for the magnetization transfer from the non-exchanging covalent bound protons to the chemically exchanging groups, e.g. the amide protons responsible for the APT. In this way, the rNOE resonance at around -3.5 ppm and the APT resonance at around 3.5 ppm are not independent effects but will exhibit a coupled behavior for a simultaneous saturation of both frequencies. Such a coupling can be described on the level of the exchange-dependent relaxation rates as a non-linearity of the CEST effects in question:

$$R_{ex}(\Delta\omega, \Delta\omega_c) \begin{cases} = R_{ex}(\Delta\omega) + R_{ex}(\Delta\omega_c) & : \text{ uncoupled effects} \\ \neq R_{ex}(\Delta\omega) + R_{ex}(\Delta\omega_c) & : \text{ coupled effects} \end{cases} \quad (6)$$

The observed mismatch, termed saturation crosstalk $T = R_{ex}(\Delta\omega) + R_{ex}(\Delta\omega_c) - R_{ex}(\Delta\omega, \Delta\omega_c)$, can be used as a measure for the amount of magnetization transfer, i.e. the coupling strength (Figure 2C). The saturation crosstalk can be quantified by subtracting two AREX spectra: one with the second RF irradiation being far off-resonant or disabled, and the other one with the additional RF irradiation saturating frequency offset $\Delta\omega_c$: $T = AREX(\Delta\omega, \Delta\omega_{\text{off}}) - AREX(\Delta\omega, \Delta\omega_c)$. Moreover, it was shown analytically that the saturation crosstalk can be calculated without the need of a prior AREX evaluation by rearranging the respective mathematical expressions:

$$T(\Delta\omega, \Delta\omega_c) = \frac{R_1}{DC} \left[\frac{1}{Z(\Delta\omega, \Delta\omega_{\text{off}})} + \frac{1}{Z(\Delta\omega_{\text{off}}, \Delta\omega_c)} - \frac{1}{Z(\Delta\omega, \Delta\omega_c)} - \frac{1}{Z(\Delta\omega_{\text{off}}, \Delta\omega_{\text{off}})} \right] \quad (7)$$

where $\Delta\omega_{\text{off}}$ is a frequency offset far off-resonant to any CEST signal, which is synonymous with disabling the saturation. This calculation avoids the necessity of obtaining an appropriate reference spectrum and thereby estimating the direct water saturation and other confounding effects by a fitting procedure. Thus, calculation of the saturation crosstalk between two particular frequency offsets is possible by only acquiring the four corresponding Z-values, which facilitates in general a fast and direct measurement.

In living tissue a comparatively broad saturation crosstalk is observed, exceeding considerably the frequency range of proteins. Hence, the acquired signal comprises, in addition to the signal of proteins, a superimposing signal contribution of semi-solid macromolecular structures. Retrieval of the superimposed protein signal is achieved by subtracting the contribution of the ssMT. The selectivity of the dualCEST approach can be once more utilized for this purpose: shifting one or both the frequency offsets off-resonant from the mobile protein signals while remaining on-resonant to the signal of the ssMT allows to determine and subtract the amplitude of the contribution:

$$T_{\text{protein}}(\Delta\omega, \Delta\omega_c) = T(\Delta\omega, \Delta\omega_c) - \frac{T(\Delta\omega, -\Delta\omega_{\text{ssMT}}) \cdot T(\Delta\omega_{\text{ssMT}}, \Delta\omega_c)}{T(\Delta\omega_{\text{ssMT}}, -\Delta\omega_{\text{ssMT}})} \quad (8)$$

1 Introduction

where $\Delta\omega_{\text{ssMT}}$ is the ssMT specific frequency offset. Of note, this correction method is independent of the actual ssMT lineshape, allowing the removal of both symmetric and asymmetric ssMT contributions. Application of this correction requires in total nine Z -values for the calculation of a protein specific signal without any confounding saturation transfer effects of metabolites, lipids and semi-solid macromolecular structures. Moreover, the signal has been shown to be independent of water relaxation properties and, in the physiological pH range between 7 and 7.4, of changes in the chemical exchange properties.

The resulting opportunity to selectively measure the intra-molecular spin diffusion in proteins is of particular interest as it may provide additional information about the pathological changes of the proteome. This is the case, as the intra-molecular spin diffusion processes depend on the size and the conformation of the involved proteins. The slower tumbling rate (i.e. molecular correlation times) of larger proteins results in a more pronounced spin diffusion, whereas an unfolding of the protein results in an distance increase between the involved nuclei and therefore in a signal decrease.⁶⁸ Indeed, investigations of protein model solutions revealed a distinct dualCEST signal increase as function of the molecular weight, indicating the potential to detect a decomposition of proteins into smaller fragments, and moreover a significant signal decrease was observed upon the unfolding of the proteins, indicating the potential to detect aberrant structural and conformational changes of proteins. The combination of all these properties render dualCEST a promising tool for the detection of aberrant proteomes in vivo and thus a potential novel diagnostic imaging modality for neurodegenerative diseases and cancer.

The aim of this thesis was therefore the translation of the dualCEST technique to a clinical whole-body MR scanner to enable protein imaging of the human brain. The dualCEST approach was up to now restricted to investigations of protein model solutions at NMR spectrometers with ultra-high magnetic field strengths. The required further developments of such a preclinical technique in order to enable patient examinations at a clinical whole-body MR scanner entail overcoming a number of technical and experimental challenges. To mention only a few: (i) the reciprocal interference of CEST preparation and imaging readout, (ii) the considerably worse SNR and spectral resolution of a clinical whole-body MR scanner, (iii) the occurrence of strong spatial B_0 and B_1 inhomogeneities, (iv) subject movement and the resulting motion artifacts, (v) acquisition time constraints of in vivo examinations, as well as (iv) safety and hardware restrictions limiting the saturation parameters.

The methodological further developments to overcome these challenges, the subsequent investigations concerning the specificity and reproducibility of the dualCEST contrast, as well as the first in vivo examinations are the main outcomes of this work. The results of this thesis were published in four scientific journal articles, which are enclosed in the following chapter and complemented by a summary, putting them into an overall context. The thesis is eventually completed by a comprehensive discussion of the results and limitations of this study in chapter 3 and a conclusion in chapter 4.

2 Publications

This thesis is written in cumulative format in accordance with the regulations regarding the conferral of doctoral degrees of the Department of Physics and Astronomy of the Ruperto-Carola University of Heidelberg. It comprises four articles published in internationally acclaimed peer-reviewed journals. Within this thesis the individual manuscripts will be referred to by roman numerals. All articles were written during the PhD project and have not been used in other dissertations. Note, the *in vitro* data of the first publication were topic of the preceding master thesis and are therefore referred to as reference 32, whereas the optimization at the clinical scanner and the *in vivo* experiments are ascribed solely to the doctoral studies and therefore referred to as Publication I. I am first author of Publications I, III and IV — principal author of III and IV, shared authorship for I and III — and co-author of Publication II. The detailed author contributions to each publication are stated in the respective sections. All articles are reproduced with kind permission of JOHN WILEY & SONS.

In addition to the four publications, this cumulative thesis includes three appendices (A, B and C) comprising the most recent methodological developments and applications. Appendices A and B were originally submitted by the author as conference abstracts for the *28th Annual Meeting of the International Society for Magnetic Resonance in Medicine, Paris, France 2020* and the *Joint Annual Scientific Meeting ISMRM-ESMRMB, Paris, France 2018*, respectively, and have been reproduced with kind permission of the INTERNATIONAL SOCIETY FOR MAGNETIC RESONANCE IN MEDICINE.^{69,70}

In the following the individual contributions and results are recapitulated and put into the overall thematic context. The topics covered in this thesis are moreover graphically summarized in figure 3.

Thematic overview over the individual publications

Publication I comprises the *in vitro* experiments presented in the preceding master thesis,³³ as well as the first results of this PhD project — the successful translation of the dualCEST technique from a 14.1 T narrow-bore NMR spectrometer to a 3 T clinical whole-body MR scanner and a first proof-of-concept *in vivo* examination. The translation was based on a comprehensive study and subsequent optimization of diverse technical parameters. As a result of the investigation, lower static magnetic field strengths were found to be beneficial for the dualCEST technique, further encouraging the translation of the approach to clinical

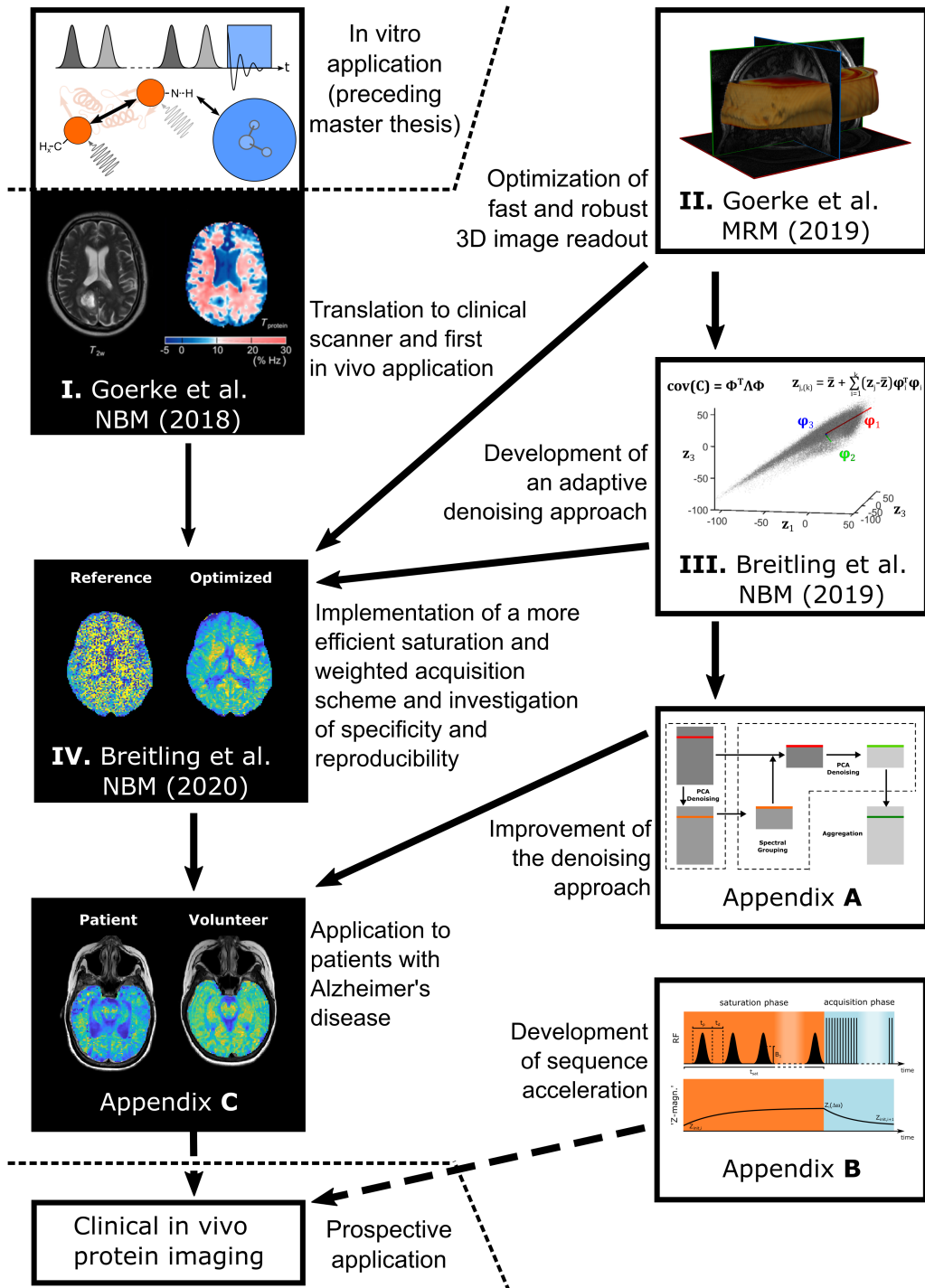


Figure 3: Illustration of the thematic allocation of the four publications (I to IV) and three appendices (A to C), which comprise this cumulative dissertation. Contributions on the right address general problems of CEST-MRI, whereas the left side specifically displays applications and developments for dualCEST. The subfigures are adapted partly from the respective contributions.

field strengths. Furthermore, the broader resonances associated with the lower field strength combined with slightly adjusted saturation frequency offsets render the dualCEST approach insensitive to the B_0 inhomogeneities encountered at a clinical system. The RF saturation pulses were optimized in amplitude, length and timing to maximize the signal while avoiding excessive broadening of the spectral resonances. In the end, the dualCEST approach was applied in a proof-of-concept examination of a patient with glioblastoma. In the necrotic tumor region a significant alteration of the dualCEST contrast was observable, indicating as expected a considerable degeneration of proteins.

Although the presented protocol enabled the first in vivo protein imaging by means of dualCEST, this implementation had some major limitations. (i) The used imaging protocol only enables 2D acquisitions and thereby offers only a small volume coverage. First of all, this reduces the practicality as a diagnostic tool as only a small section of the body can be investigated. And secondly, it effectively prevents the crucial application of a motion correction as a displacement or tilting of the investigated body region out of the imaging slice results in the irreversible loss of information. (ii) The inherently low SNR of the dualCEST approach resulted in the necessity of acquiring multiple averages to achieve a sufficiently good image quality. The resulting comparatively long measurement time prevented, at this point in time, the application in clinical trials.

To overcome the first set of limitations, the aim was to combine the dualCEST approach with a suitable fast and robust 3D image-readout – namely the snapshot-CEST sequence.⁷¹ This gradient echo-based acquisition scheme has been specifically developed for CEST imaging and is tailored to its particular requirements. In the second publication, the snapshot-CEST readout was utilized for a state-of-the-art conventional CEST acquisition protocol. The study included among other things a thorough investigation and optimization of the imaging parameters, e.g. parallel acceleration factor and readout bandwidth, to maximize the SNR and volume coverage while at the same time avoiding contrast deviations. With regard to the topic of this thesis, the obtained optimal imaging parameters are not only valid for the presented conventional CEST approach, but – as they were determined with the same setup and 3T whole-body MR-scanner as intended for dualCEST studies – also for the application together with the dualCEST technique. In addition, the imaging protocol presented in Publication II, with its optimized readout and fitting routines, represents a state-of-the-art conventional protein CEST approach and is therefore in what follows an ideal reference for the comparison with the dualCEST technique.

In addition to the obtained volume coverage and being more SNR-efficient, a 3D image readout generates tens of thousands of CEST spectra in a single measurement, raising the possibility for statistical denoising. The basis to this end is the identification of spectral redundancies allowing to separate noise-like characteristics from meaningful spectral features. In the third publication a novel denoising technique is presented that allows an effective and robust denoising of CEST data. The approach combines a principal component analysis (PCA)⁷² with an appropriate data-driven identification of the relevant information.^{73–75} PCA is a well-established technique for reducing the dimensionality of data sets, while preserving most of the contained information. For this purpose the data is transformed into

2 Publications

a new basis, which is obtained by identifying and exploiting linear correlations. The information content of the data set, i.e. the variance, concentrates on only a few of these new components with the others describing mainly noise.⁷⁶ Therefore, reducing the dimensionality of the data set by retaining only the relevant components will remove noise. In the presented approach, the PCA is applied in conjunction with data-driven methods to identify the relevant components. The latter is essential for the final outcome as retaining too few components will result in the loss of actual information, whereas too many components will diminish the denoising effect. In the publication, the proposed method was thoroughly examined and validated on synthesized data, generated by adding artificial noise to fitted *in vivo* Z-spectra. Furthermore, the approach was applied to data of seven healthy volunteers acquired at clinical or ultra-high field whole-body scanners. For conventional CEST data the denoising capability was quantified to be comparable or even superior to the averaging of six measurements. The application of the proposed denoising algorithm is not restricted to conventional CEST data sets but can be applied to any other CEST-related approach providing a spectral dimension to exploit redundancies. For dualCEST-MRI this opens up the possibility to overcome the inherently low SNR.

In the fourth and last publication all further developments were brought together to form a dualCEST-MRI protocol enabling protein imaging in a clinically-relevant time frame. To this end, the previous results – i.e. the initial investigations of Publication I, the fast and robust volumetric image readout of Publication II and the adaptive denoising technique of Publication III – were complemented by two additional methodological advances: (i) improved dual-frequency pulses and (ii) a weighted acquisition scheme. The implementation and optimization of cosine-modulated dual-frequency presaturation pulses^{77,78} enabled a simultaneous irradiation at both frequency offsets and thereby a significantly improved saturation efficiency compared to the previous alternating RF irradiation scheme. Development of a weighted acquisition scheme furthermore allowed for an optimal use of the limited examination time. This is based on the remaining necessity to acquire multiple averages of each frequency offset pair to achieve a satisfying image quality for dualCEST-MRI. In the calculation of the dualCEST contrast certain frequency offset pairs have ultimately a larger impact on the quality image than others, and hence should be averaged more often. The idea was therefore to determine the optimal measurement distribution for the acquisition scheme, which minimizes the overall measurement error for an analytical model of the error propagation. This approach thereby results in an improved image quality while maintaining the same number of total repetitions. Overall, the application of optimized saturation, sampling scheme, readout with motion correction and denoising algorithm resulted in an SNR gain by a factor of eight compared to the initial imaging protocol presented in Publication I.

To assess the potential applicability in a clinical setting, Publication IV comprised furthermore investigations concerning the protein specificity, repeatability, and sensitivity to pathological alterations. Preserved specificity of the dualCEST technique despite the translation to a clinical whole-body MR scanner was confirmed in extensive measurements of biochemical model solutions. Furthermore, repeated volunteer examinations demonstrated a good-to-excellent reproducibility⁷⁹ of the imaging protocol and allowed to estimate the smallest

resolvable contrast change. Finally, a first proof-of-principle examination with this protocol showed alterations in the tumor region of a patient with glioblastoma, indicating a significant pathological modification of mobile proteins. Altogether the proposed imaging protocol enables prospectively the examination of larger patient cohorts, and thus assessment of the potential diagnostic value of dualCEST-MRI.

With this well-established imaging protocol at hand the prospective aims are twofold: investigation of the diagnostic value for various pathologies and a further acceleration of the technique to enable the incorporation into standard clinical protocols. The Appendices A, B and C present the most recent advances for both objectives.

An acceleration of dualCEST-MRI, i.e. a reduction of the overall examination time, can in principle be realized in two ways: increasing the SNR of each repetition to reduce the necessary number of averages, or to shorten the time for one repetition. In Appendix A a further developed denoising approach is presented allowing to effectively increase the SNR by an additional 14% compared to the previous technique. To achieve this, the algorithm combines the formation of subsets of similar spectra with a subsequent PCA. Exploiting only the subtle remaining spectral differences of the reduced data set allows for a better identification and isolation of the obscured spectral features.

The second possibility is exploited in Appendix B. DualCEST as most other quantitative CEST techniques relies on the steady-state signal, which entails a long enough saturation period in the order of 3 – 5 times T_1 .⁴⁵ The proposed method allows to bypass this obstacle by calculating the steady-state signal from an experiment using only a reduced saturation period. To this end, the analytical description of the signal evolution (Equation 3) is numerically solved for the steady-state magnetization. For dualCEST-MRI this would allow to reduce the saturation period by up to 75%, at however the cost of slightly reduced SNR.

Finally, Appendix C comprises the first preliminary results of a forthcoming pilot study concerning Alzheimer's disease. The dualCEST examinations of two patients and two age-matched healthy volunteers revealed considerable changes for one of the two patients and, interestingly, no apparent abnormalities for the other. This difference in the contrast behavior might actually be related to a genuine difference in the stage of the disease progression. In this case, dualCEST-MRI could be used to avoid other invasive modalities to monitor the disease progression. As a result, examinations could be performed on a more regular and frequent basis, resulting in an improved level of patient care. However, the study size is yet too small to draw any final conclusions and more participants will have to be included to ultimately assess the potential of dualCEST-MRI as a diagnostic tool.

Publication I

Dual-frequency irradiation CEST-MRI of endogenous bulk mobile proteins

Authors: Steffen Goerke[†], **Johannes Breitling**[†], Moritz Zaiss, Johannes Windschuh, Patrick Kunz, Patrick Schuenke, Daniel Paech, Dario L. Longo, Karel D. Klika, Mark E. Ladd, and Peter Bachert

[†] both authors contributed equally to this work

Journal reference: NMR in Biomedicine. 2018;31:e3920.




DOI: 10.1002/nbm.3920

Author contributions: SG conceived together with MZ and JW the idea of the dualCEST approach. SG and **JB** designed together the study with consultation of PK for the in vitro experiments. **JB** performed, with minor exceptions, all data acquisition, processing and analysis. In addition **JB** conceived the correction approach necessary for the in vivo application. PS integrated the dualCEST approach into the imaging sequence. DP was responsible for the recruitment and medical supervision of the patient examination. DLL provided the investigated protein-free brain lipids. KDK provided technical support for the NMR spectrometer. SG drafted and revised the manuscript with support of **JB** and critical review by all co-authors.

Remark: The in vitro experiments of this publication were topic of the preceding master thesis. The optimization at the clinical scanner and the in vivo experiments are ascribed to the doctoral studies.

RESEARCH ARTICLE

Dual-frequency irradiation CEST-MRI of endogenous bulk mobile proteins

Steffen Goerke¹  | Johannes Breitling¹ | Moritz Zaiss^{1,2}  | Johannes Windschuh¹ | Patrick Kunz³ | Patrick Schuenke¹ | Daniel Paech⁴ | Dario L. Longo⁵  | Karel D. Klika⁶ | Mark E. Ladd^{1,7,8} | Peter Bachert^{1,7}¹Division of Medical Physics in Radiology, German Cancer Research Center (DKFZ), Heidelberg, Germany²Department of High-field Magnetic Resonance, Max-Planck-Institute for Biological Cybernetics, Tübingen, Germany³Division of Functional Genome Analysis, German Cancer Research Center (DKFZ), Heidelberg, Germany⁴Department of Radiology, German Cancer Research Center (DKFZ), Heidelberg, Germany⁵Institute of Biostructure and Bioimaging (IBB), National Research Council (CNR), Torino, Italy⁶Molecular Structure Analysis, German Cancer Research Center (DKFZ), Heidelberg, Germany⁷Department of Physics and Astronomy, University of Heidelberg, Heidelberg, Germany⁸Faculty of Medicine, University of Heidelberg, Heidelberg, Germany**Correspondence**

S. Goerke, Division of Medical Physics in Radiology, German Cancer Research Center (DKFZ), Im Neuenheimer Feld 280, 69120 Heidelberg, Baden-Württemberg, Germany. Email: s.goerke@dkfz.de

A novel MRI contrast is proposed which enables the selective detection of endogenous bulk mobile proteins *in vivo*. Such a non-invasive imaging technique may be of particular interest for many diseases associated with pathological alterations of protein expression, such as cancer and neurodegenerative disorders. Specificity to mobile proteins was achieved by the selective measurement of intramolecular spin diffusion and the removal of semi-solid macromolecular signal components by a correction procedure. For this purpose, the approach of chemical exchange saturation transfer (CEST) was extended to a radiofrequency (RF) irradiation scheme at two different frequency offsets (dualCEST). Using protein model solutions, it was demonstrated that the dualCEST technique allows the calculation of an image contrast which is exclusively sensitive to changes in concentration, molecular size and the folding state of mobile proteins. With respect to application in humans, dualCEST overcomes the selectivity limitations at relatively low magnetic field strengths, and thus enables examinations on clinical MR scanners. The feasibility of dualCEST examinations in humans was verified by a proof-of-principle examination of a brain tumor patient at 3 T. With its specificity for the mobile fraction of the proteome, its comparable sensitivity to conventional water proton MRI and its applicability to clinical MR scanners, this technique represents a further step towards the non-invasive imaging of proteomic changes in humans.

KEYWORDS

cancer, CEST, magnetization transfer, MRI, proteins, spin diffusion

Abbreviations used: AREX, apparent exchange-dependent relaxation; B_0 , magnetic field strength; B_1 , RF amplitude; BSA, bovine serum albumin; CEST, chemical exchange saturation transfer; CSF, cerebrospinal fluid; DC, duty cycle; dualCEST, dual-frequency irradiation CEST; M_0 , equilibrium water magnetization; M_{sat} , water magnetization after pre-saturation; MW, molecular weight; off, far off-resonant frequency offset; PBS, phosphate-buffered saline; R_{1obs} , observed longitudinal relaxation rate of water; RF, radiofrequency; rNOE, relayed nuclear Overhauser effect; SAR, specific absorption rate; SDS, sodium dodecyl sulfate; SNR, signal-to-noise ratio; ssMT, semi-solid magnetization transfer; T_{1obs} , observed longitudinal relaxation time of water; $T_{\Delta\omega c}(\Delta\omega)$, saturation crosstalk; t_p , pulse length; t_d , interpulse delay; t_{sat} , saturation length; $T_{protein}$, isolated saturation crosstalk of mobile proteins; T_{ssMT} , isolated saturation crosstalk of semi-solid macromolecular structures; Z, Z-spectrum; Z_{ref} , reference Z-spectrum; $\Delta\omega$, frequency offset; $\Delta\omega_c$, constant frequency offset. Steffen Goerke and Johannes Breitling contributed equally to this work.

1 | INTRODUCTION

Chemical exchange saturation transfer (CEST) MRI has emerged as an important contrast mechanism for the detection of low concentration solutes, such as proteins or small metabolites in living tissue.¹⁻⁵ CEST exploits the spontaneous chemical exchange of protons in order to indirectly detect the solutes via the abundant water proton signal. This is realized by a frequency-selective pre-saturation of chemically exchanging protons in solutes and a subsequent fast MRI readout of the water signal. The indirect detection generates a signal amplification enabling, in principle, high-resolution imaging of solutes with a sensitivity comparable to normal water proton MRI.

However, in living tissue diverse CEST signals of different cellular compounds, such as proteins,⁶⁻⁹ small metabolites,¹⁰⁻¹⁵ lipids^{16,17} and semi-solid macromolecular structures,¹⁸⁻²⁰ spectrally overlap in the Z-spectrum (Figure 1B). Moreover, CEST signals depend on the rate of chemical exchange, which in turn is determined by various physiological parameters, in particular pH and temperature.^{3,21-23} On the one hand, this multi-parametric dependence makes CEST a valuable imaging technique with the potential to depict a wide range of physiological processes, but, on the other, the numerous parameters are also a strong drawback in terms of specificity. Although specific adjustments of the CEST pulse scheme (e.g. tuning of the pre-saturation amplitude B_1 or the interpulse delay t_d) allow the design of exchange rate filters²⁴⁻²⁶ that highlight the signal component of one specific compound, to date a selective detection without contributions from other cellular compounds has not been possible. The introduction of specificity has become one of the most important issues in the research field of CEST-MRI.

Here, we present a novel CEST-based technique – dual-frequency irradiation CEST (dualCEST) – that allows the selective detection of endogenous bulk mobile proteins *in vivo*. Specificity of the dualCEST signal is achieved by the introduction of a novel dimension of selectivity: the detection of the coupling between different CEST signals (Figure 1B). As only mobile proteins possess individual resonances of significant amplitude on both sides of the Z-spectrum that are coupled via a magnetization transfer pathway, exceptional specificity can be achieved by taking advantage of this trait. Signal contributions from the comparatively broad resonance of the semi-solid magnetization transfer (ssMT) can be removed by a correction procedure. Pre-saturation at two different frequency offsets, $\Delta\omega$ and $\Delta\omega_C$, was realized by an alternating radiofrequency (RF) irradiation scheme (Figure 1A).

The terminology 'bulk mobile proteins' is a combination of the specificity of the dualCEST technique to the collective signal of all proteins and the separation of MR signals by their mobility (for a detailed explanation, see the Discussion section). The bulk mobile protein signal comprises mainly cytosolic proteins, many endoplasmic reticulum proteins and secreted proteins.⁸ Although the detection of specific protein species is not feasible by this means, the bulk mobile protein signal is expected to be a valuable marker for diseases that are associated with profound alterations of the proteome. Bulk mobile proteins are generally assumed to be the main source of the prominent amide proton resonance at

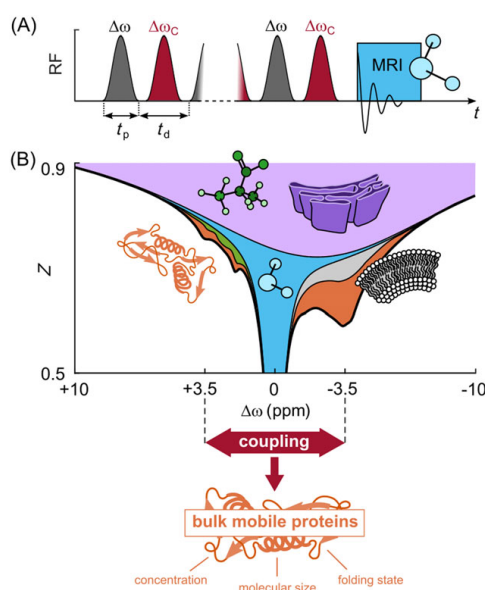


FIGURE 1 The dual-frequency irradiation chemical exchange saturation transfer (dualCEST) approach. (A) Scheme of the pulse sequence. (B) Z-spectrum of *ex vivo* porcine brain tissue homogenate ($B_1 = 0.75 \mu\text{T}$, $B_0 = 14.1 \text{ T}$). The subdivision of the Z-spectrum into contributions of different cellular compounds is an estimation. dualCEST detects the coupling of different CEST signals, allowing the selection of signals of bulk mobile proteins (orange) from the background of other cellular compounds: metabolites (green), lipids (gray), semi-solid macromolecular structures (purple) and water (blue)

$\Delta\omega = +3.5$ ppm or the relayed nuclear Overhauser effect (rNOE)-CEST signal of aliphatic protons at around $\Delta\omega = -3.5$ ppm.^{6-8,16,17,27-32} These two signals have already been shown to allow the diagnosis of several diverse diseases and to provide decisive information for ongoing therapy. Especially with respect to cancer, CEST imaging at $\Delta\omega = \pm 3.5$ ppm has enabled the assessment of tumor malignancy,³³ the differentiation between radiation necrosis and tumor progression^{34,35} and the detection of disrupted blood-brain barriers without the application of contrast media.⁹ Although the value of the amide and aliphatic proton signal has been demonstrated in diverse studies, nevertheless, the underlying origin of the contrast is not completely understood. The technique of dualCEST represents a unique opportunity to determine the actual contribution of mobile proteins to CEST signal changes in pathological tissue, which may lead to new insights into diseases on a molecular level.

This study comprises the introduction of the dualCEST contrast mechanism, a comprehensive optimization of technical parameters, an analytical model of the observed signal, an experimental verification of its specificity to mobile proteins *in vitro* and a proof-of-principle demonstration of its applicability *in vivo*. A detailed analysis of the diagnostic value of the method will be addressed in a future study. With respect to examinations in humans, the exceptional specificity of the presented technique evades the ultra-high static magnetic field strengths $B_0 \geq 7$ T that are required for the adequate separation of individual resonances in conventional CEST-MRI, thus allowing its straightforward application on clinical MR scanners ($B_0 \leq 3$ T). Hence, dualCEST enables the selective detection of endogenous bulk mobile proteins at clinical magnetic field strength, providing the potential to be a valuable diagnostic tool to detect aberrant proteomes *in vivo*.

2 | MATERIALS AND METHODS

2.1 | Model solutions

In total, 42 model solutions containing varying amounts of globular proteins, sodium dodecyl sulfate (SDS), creatine, carnosine, lipids and tissue homogenates were prepared. A detailed list of all experimental parameters is presented in Supporting Information Table S1. Unless otherwise specified, model solutions were buffered at pH 7 using phosphate-buffered saline (PBS). Final pH values were checked by means of a calibrated pH electrode, and deviations from pH 7 (e.g. in the case of high solute concentrations) were corrected using NaOH or HCl. All model solutions were pipetted from highly concentrated stock solutions to ensure the precise adjustment of different concentrations. Samples containing *ex vivo* tissue components were continuously chilled on ice before measurement. Protein-free brain lipids were extracted from mouse brain tissue with tetrahydrofuran, filtered and lyophilized for liposome preparation (size, 120 nm) throughout sonication. Tissue homogenates were obtained from white matter porcine brain tissue and prepared as described in previous studies.⁹

2.2 | Subjects

One 57-year-old male patient with newly diagnosed and histopathologically proven glioblastoma (grade IV) was examined before therapy. This study was approved by the local ethics committee of the Medical Faculty of the University of Heidelberg and is in accordance with the relevant guidelines and regulations. Written informed consent was received from the patient prior to the examination.

2.3 | CEST spectroscopy

Model solutions were examined on 14.1-T (600 MHz for ^1H) Avance II and 9.4-T (400 MHz for ^1H) Avance III narrow-bore spectrometers (Bruker BioSpin, Karlsruhe-Rheinstetten, Germany). A 5-mm or 8-mm probe was used for RF irradiation and signal acquisition. To avoid radiation damping, the probes were operated detuned. The temperature of the samples was stabilized at 25 or 37°C using the internal heating and cooling device. For conventional CEST measurements, pre-saturation at $\Delta\omega$ was achieved by Gaussian-shaped RF pulses of mean amplitude $B_1 = \text{flip angle}/(\gamma \cdot t_p)$, length t_p and duty cycle $\text{DC} = t_p/(t_p + t_d)$. In the case of dualCEST, an additional Gaussian-shaped RF pulse ($\Delta\omega_c$) of the same amplitude and length was centered in the middle of the interpulse delay t_d (Figure 1A). A detailed list of all experimental parameters is presented in Table S1. The overall duration of the pre-saturation period t_{sat} complied with the criterion for steady-state measurements, $t_{\text{sat}} > 3-4 \cdot T_{1\text{obs}}$, with the observed longitudinal relaxation time of water $T_{1\text{obs}}$.²⁰ Z-values were calculated by integration of the water resonance in the range of ± 0.45 ppm (M_{sat}) and normalized with the equilibrium magnetization (M_0): $Z = M_{\text{sat}}/M_0$. To compensate for systematic signal fluctuations (i.e. caused by the signal amplifier or receiver), M_0 was acquired at different time points and interpolated to obtain an individual M_0 for each pre-saturation cycle. Conventional Z-spectra were sampled at 118 frequency offsets in unequal steps between ± 150 ppm. Isolated CEST signals, compensated for direct water saturation effects (spillover dilution), ssMT and water relaxation properties, were calculated at each frequency offset $\Delta\omega$ using the apparent exchange-dependent relaxation (AREX) evaluation³⁶: $\text{AREX}(\Delta\omega) = \frac{R_{1\text{obs}}}{\text{DC}} \cdot \left(\frac{1}{Z(\Delta\omega)} - \frac{1}{Z_{\text{ref}}(\Delta\omega)} \right)$. The observed longitudinal relaxation rate of water

$R_{1\text{obs}} = \frac{1}{T_{1\text{obs}}}$ was measured using a saturation-recovery sequence. The reference spectrum Z_{ref} was estimated by a multi-parametric fit: $Z_{\text{ref}} = 1 - \sum_i L_i$, where L_i are Lorentzian-shaped functions representing the direct water saturation and ssMT. To avoid contributions from CEST signals, as well as to take into account the broadening of the direct water saturation as a result of a pulsed pre-saturation, data points in the range from ± 10 to ± 0.5 ppm and in between ± 0.2 ppm were excluded from the fitting procedure. Conventional asymmetry analysis (based on non-fitted

data) was performed by: $MTR_{\text{asym}}(\Delta\omega) = Z(-\Delta\omega) - Z(\Delta\omega)$. Depending on the CEST signal strength of the respective evaluation method, measurements were repeated several times (Table S1).

2.4 | DualCEST MRI

In vivo measurements were performed on a 3-T (123.26 MHz for ^1H) whole-body MR-PET tomograph (Biograph mMR; Siemens Healthcare GmbH, Erlangen, Germany) using a custom-developed CEST pulse sequence based on a two-dimensional Half Fourier Acquisition Single Shot Turbo Spin Echo (HASTE) readout and a 16-channel Siemens mMR Head/Neck A Tim Coil. M_{sat} images (matrix, 128×102 ; resolution, $1.88 \times 1.88 \times 5 \text{ mm}^3$) were acquired after pre-saturation with 84 pairs of Gaussian-shaped RF pulses at $\Delta\omega$ and $\Delta\omega_{\text{C}}$ of $B_1 = 2 \mu\text{T}$, $t_p = 20 \text{ ms}$ and DC = 28%, leading to $t_{\text{sat}} = 6 \text{ s}$. All images were corrected for motion artifacts by an intensity-based image registration. Analogous to CEST spectroscopy, several M_0 images were acquired at different time points and interpolated to yield an individual M_0 for each Z-image. To increase the signal-to-noise ratio (SNR), Z-images were averaged over 18 acquisitions and smoothed by a Gaussian kernel ($\sigma = 1 \text{ pixel}$). The final dualCEST contrast (Equation 2) was corrected for B_1 inhomogeneities by means of the one-point 'contrast-correction' method as described in a previous study.³⁷ B_0 and B_1 were determined by the simultaneous mapping of the water shift and B_1 (WASABI)³⁸ approach using the same CEST pulse sequence with adjusted pre-saturation parameters. $T_{1\text{obs}}$ mapping was achieved by fitting $T_{1\text{obs}}$ -weighted images of a saturation recovery HASTE sequence. In total, the overall measurement time was approximately 22 min, comprising 18 min of dualCEST, 2 min of WASABI and 2 min of $T_{1\text{obs}}$ mapping.

To investigate the influence of B_0 , the same dualCEST pulse sequence was implemented on a 7-T whole-body MR tomograph (MAGNETOM 7 T; Siemens Healthcare GmbH), but based on a two-dimensional gradient echo (GRE) readout.

3 | RESULTS

3.1 | The dualCEST approach

To demonstrate the concept of the dualCEST approach, a mobile protein solution containing bovine serum albumin (BSA) was investigated. DualCEST detects the MR signal of water after alternating RF irradiation at two different frequency offsets, $\Delta\omega$ and $\Delta\omega_{\text{C}}$ (Figure 1A). This allows the simultaneous sampling of the conventional Z-spectrum as a function of $\Delta\omega$ while constantly saturating CEST signals at $\Delta\omega_{\text{C}}$ (Figure 2A). For a

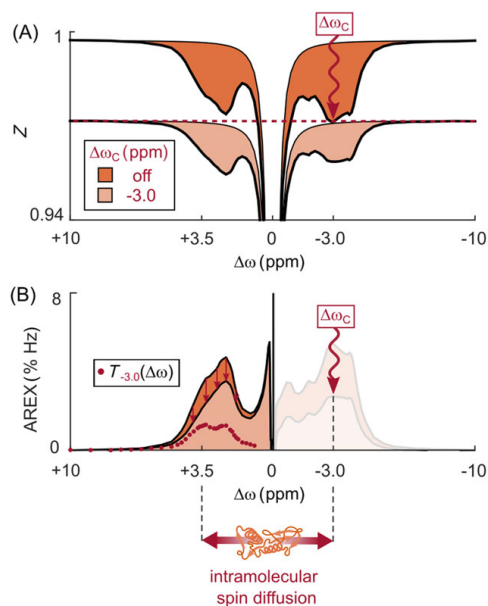


FIGURE 2 Isolation of the saturation crosstalk. (A) Z-spectra of a mobile protein solution containing BSA ($B_1 = 0.45 \mu\text{T}$, $B_0 = 14.1 \text{ T}$) with and without constant saturation at $\Delta\omega_{\text{C}}$. (B) Isolated CEST signals calculated by the AREX evaluation. The saturation crosstalk $T_{\Delta\omega_{\text{C}}}(\Delta\omega)$ (red dots) is defined by the difference between the two AREX spectra

detailed analysis of the influence of the constant saturation, the CEST signals of proteins were separated from the direct water saturation ($\Delta\omega = 0$ ppm) by the AREX evaluation³⁶ (Figure 2B). Constant saturation at $\Delta\omega_c = -3.0$ ppm led to a significant reduction in protein CEST signals on the opposite side of the water resonance ($\Delta\omega > 0$ ppm). Hence, protein CEST signals in the positive and negative frequency region are coupled via a magnetization transfer pathway. The amount of magnetization transfer between two particular frequency offsets – in the following, termed as saturation crosstalk $T_{\Delta\omega_c}(\Delta\omega)$ – can be quantified by subtraction of the AREX spectra. Quantification by simple subtraction of the two spectra is justified because of the linearity of CEST signals using the AREX evaluation. Remarkably, for mobile proteins, the saturation crosstalk is on the order of 30–40% of the conventional AREX spectrum, demonstrating the potential for its application *in vivo*. The observed saturation crosstalk is attributed to intramolecular spin diffusion³⁹ between dipolar-coupled protons. Spin diffusion is also known to mediate the intramolecular magnetization transfer of rNOE-CEST signals, which have been studied extensively in the past few years.^{16,17,26,40}

Rearrangement of the mathematical expression for T allows the calculation of the saturation crosstalk without the need for prior AREX evaluation (Supporting Information Figure S1):

$$T_{\Delta\omega_c}(\Delta\omega) = \frac{R_{1\text{obs}}}{\text{DC}} \cdot \left[\frac{1}{Z_{\text{off}}(\Delta\omega)} + \frac{1}{Z_{\Delta\omega_c}(\text{off})} - \frac{1}{Z_{\Delta\omega_c}(\Delta\omega)} - \frac{1}{Z_{\text{off}}(\text{off})} \right] \quad (1)$$

where $Z_{\Delta\omega_c}(\Delta\omega)$ is the Z -value after saturation at $\Delta\omega$ and $\Delta\omega_c$, and the far off-resonant frequency offset, $\text{off} = 150$ ppm, which is synonymous with disabling of the saturation. This calculation has the advantage that $T_{\Delta\omega_c}(\Delta\omega)$ can be determined without the need for the estimation of the direct water saturation by a fitting procedure. Consequently, the saturation crosstalk between two particular frequency offsets is characterized by only four Z -values (Equation 1), allowing a fast and direct acquisition which is crucial for application *in vivo*.

In order to maximize the dualCEST signal, its dependence on several technical parameters was investigated. T monotonically increases as a function of the saturation duration and reaches steady state at $t_{\text{sat}} \approx 3 \cdot T_{1\text{obs}}$ (Figure 3B). Furthermore, T is effectively independent of the DC (Figure 3D), in compliance with the AREX evaluation. An unexpected observation is the increase in T for shorter pulse lengths t_p (Figure 3F), which thereby provides a simple means to amplify the dualCEST signal. A detailed explanation of this effect is provided in the Discussion section. Remarkably, an increase in T can also be observed for decreasing magnetic field strengths (Figure 3J), thus enabling the application of the dualCEST technique on clinical MR scanners. In addition, B_1 can be increased to amplify the dualCEST signal (Figure 3H). The monotonic increase is again in coherence with the AREX evaluation. For further investigations on the 14.1-T MR spectrometer, $t_p = 7.8$ ms and $B_1 = 1.5$ μT were used, which are optimal in terms of maximizing the signal strength while avoiding an excessive broadening of signals.

The advantage of the dualCEST approach in comparison to conventional CEST is that it provides a novel dimension of selectivity. As dualCEST detects the coupling between two different CEST signals, selectivity to compounds that exhibit more than one resonance in the Z -spectrum can be achieved. Consequently, by setting the two frequency offsets to the positive and negative regions ($\Delta\omega > 0$ and $\Delta\omega_c < 0$ ppm), the dualCEST signal is selective to mobile proteins because only mobile proteins offer individual resonances of significant amplitude on both sides of the Z -spectrum (Figure 1B). However, as the comparatively broad resonance of ssMT also ranges from positive to negative frequency offsets, a contribution to the dualCEST signal from macromolecular structures can be expected. To retrieve the isolated signal of mobile proteins, a correction method has to be applied.

3.2 | Correction for signals of semi-solid macromolecular structures

To investigate the dualCEST signal of mobile proteins in the presence of semi-solid macromolecular structures, an *ex vivo* tissue homogenate derived from porcine brain was prepared. The corresponding dualCEST spectrum obtained with similar sequence parameters as in Figure 2 ($\Delta\omega_c = -3.5$ ppm) exhibits a comparatively broad saturation crosstalk with a spectral width larger than 10 ppm (Figure 4B, red line). Hence, the acquired signal comprises, in addition to signals of mobile proteins, a component originating from semi-solid macromolecular structures. To extract the superimposed signal of mobile proteins T_{protein} , the selectivity of the dualCEST approach was utilized (Figure 4A): By shifting the constant saturation frequency off-resonance from mobile protein signals while remaining on-resonance for the ssMT ($\Delta\omega_c = -10$ ppm), the spectral profile of the underlying ssMT component can be sampled in an isolated manner (Figure 4B, magenta line). The actual amplitude of the isolated saturation crosstalk of semi-solid macromolecular structures T_{ssMT} (Figure 4B, black line) is determined by scaling the spectral profile by the factor $T_{-3.5(+10)}/T_{-10(+10)}$ (Figure 4B, gray circles). This calculation is not an estimation but can be derived analytically (Supporting Information Figure S2). It is important to note that the correction method is also independent of the ssMT line shape, allowing application even in the case of an asymmetric ssMT. Overall, the isolated signal of mobile proteins in the presence of semi-solid macromolecular structures can be determined by:

$$T_{\text{protein}}(\Delta\omega) = T_{-3.5}(\Delta\omega) - \underbrace{\frac{T_{-3.5(+10)}}{T_{-10(+10)}}}_{T_{\text{ssMT}}} \cdot T_{-10}(\Delta\omega) \quad (2)$$

Equation 2 enables the application of the dualCEST approach to investigate alterations of bulk mobile proteins in living organisms. For the calculation of T_{protein} , altogether nine Z -values are required, which leads to about a doubling in the acquisition time compared with the uncorrected signal (Equation 1). However, a fitting procedure is still not required, allowing the fast determination of T_{protein} *in vivo* without the need

to sample an entire spectrum at various $\Delta\omega$. The absence of signals T_{protein} at frequency offsets larger than 10 ppm (Figure 4B, orange line) indicates proper functioning of the proposed correction procedure. It is worth noting the presence of an asymmetric ssMT in this experiment (Figure 4A, purple region) which does not distract from proper functioning of the correction method. However, to unambiguously verify the assignment of the dualCEST signal to mobile proteins, different cellular compounds were added successively to a protein model solution.

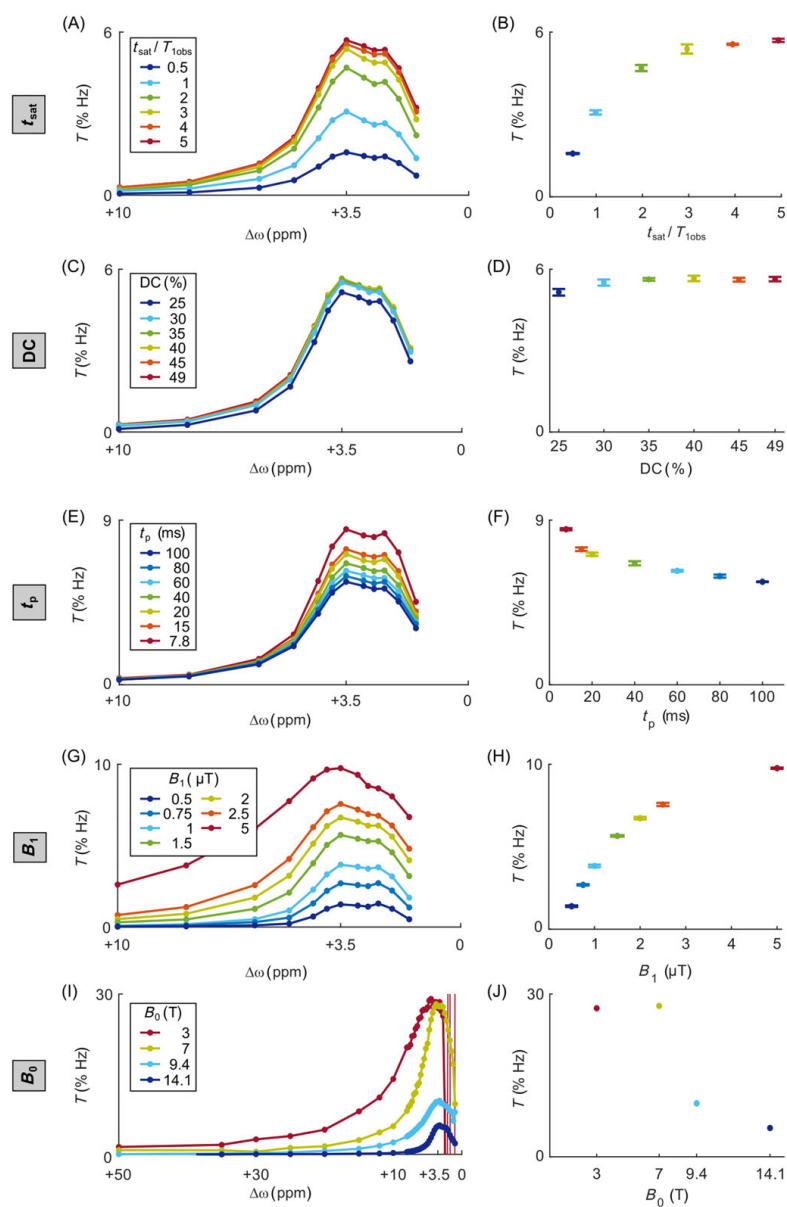


FIGURE 3 Dependence of the dualCEST signal on technical parameters. T -spectra of BSA ($\Delta\omega_{\text{C}} = -3.5$ ppm, $B_1 = 1.5$ μT , $B_0 = 14.1$ T) for different saturation lengths t_{sat} (A), duty cycles (DC) (C), pulse lengths t_p (E), B_1 (G) and B_0 (I). (B, D, F, H, J) Percentage variation of T at $\Delta\omega = +3.5$ ppm. Signal dependences allow the optimization of the pulse sequence in terms of SNR. Displayed errors are the standard deviation of repeated measurements (Table S1)

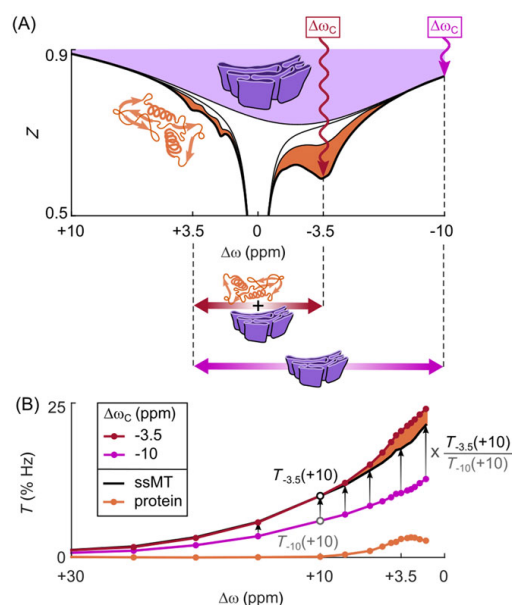


FIGURE 4 The semi-solid magnetization transfer (ssMT) correction procedure. (A) Z-spectrum of *ex vivo* porcine brain tissue homogenate ($B_1 = 0.75 \mu\text{T}$, $B_0 = 14.1 \text{ T}$). The subdivision of the Z-spectrum into contributions from different cellular compounds is an estimation. By the choice of $\Delta\omega_C$, selectivity of the dualCEST signal to different cellular compounds can be achieved. (B) Scaling of the spectral profile of signals originating from semi-solid macromolecular structures $T_{-10}(\Delta\omega)$ (magenta line) allows the retrieval of the isolated signal of mobile proteins T_{protein} (orange line)

3.3 | Characterization of the dualCEST signal

As is commonly known, signals of different cellular compounds spectrally overlap in Z-spectra *in vivo* (Figure 1B). To mimic this situation, mobile protein solutions were prepared containing: (i) BSA, as well as varying amounts of (ii) metabolites (i.e. carnosine and creatine) and (iii) lipids purified from mouse brain tissue (Figure 5). In addition to the CEST signals of BSA in the positive and negative frequency regions (Figure 5B, orange line), individual resonances of carnosine, creatine and tissue-lipids are resolved around $\Delta\omega = +3.5$, $+2.0$ and -3.5 ppm, respectively (Figure 5B). In addition, a broad asymmetric ssMT of tissue-lipids is also present (Figure 5A, blue lines), completing the imitated *in vivo* Z-spectrum. The asymmetry of the ssMT can be seen in the MTR_{asym} spectra, which leads to negative values (Figure 5C). Remarkably, although Z-spectra and MTR_{asym} spectra strongly depend on the added cellular compounds, the dualCEST signal remains constant (Figure 5D). This verifies the assignment of T_{protein} to originate exclusively from mobile proteins. Furthermore, T_{protein} is compensated for changes in water signal relaxation (Figure 5E), enabling an independent investigation of bulk mobile proteins in living organisms.

To identify the physiological parameters that affect the amplitude of the dualCEST signal, mobile protein solutions were investigated under various conditions (i.e. concentration, molecular size, folding state and pH). As these model solutions did not contain any semi-solid macromolecular structures, the dualCEST signal T was evaluated without the ssMT correction procedure being applied (Equation 1). As expected, T increases as a function of mobile protein concentration (Figure 6A). The deviation from a linear increase at high concentrations, $c > 10\%$ (w/v), most likely originates from crowding effects that influence the mobility of BSA molecules.⁴¹ In addition to its obvious dependence on concentration, a considerable variation in T as a function of the molecular size, and also the protein folding state (i.e. conformation), is expected. This is the case, as the dualCEST signal arises from intramolecular spin diffusion processes that are stronger with slower tumbling of the molecules (i.e. molecular correlation time) and are weaker with increasing distances between the involved nuclei.³⁹ Indeed, a distinct increase in T as a function of the molecular weight (MW, i.e. molecular size) is observed (Figure 6B), demonstrating the potential of dualCEST to detect a decomposition of proteins into smaller fragments. For different MWs the mass concentration (i.e. protein mass per unit volume) was kept constant to exclude concentration effects. In addition, effects from different folding states of the proteins are negligible because all of the investigated proteins belong to the same class of globular proteins, which are spherical in shape. Following previous studies,⁴²⁻⁴⁴ the equilibrium unfolding transition of BSA was examined using the detergent SDS as a denaturant and monitored by fluorescence spectroscopy (Figure 6F). Indeed, a good correlation between T and the protein folding state is observed. This illustrates the potential of dualCEST to image aberrant structural and conformational changes of proteins. Finally, the pH dependence was investigated in order to demonstrate the robustness of the dualCEST signal against changes in the chemical

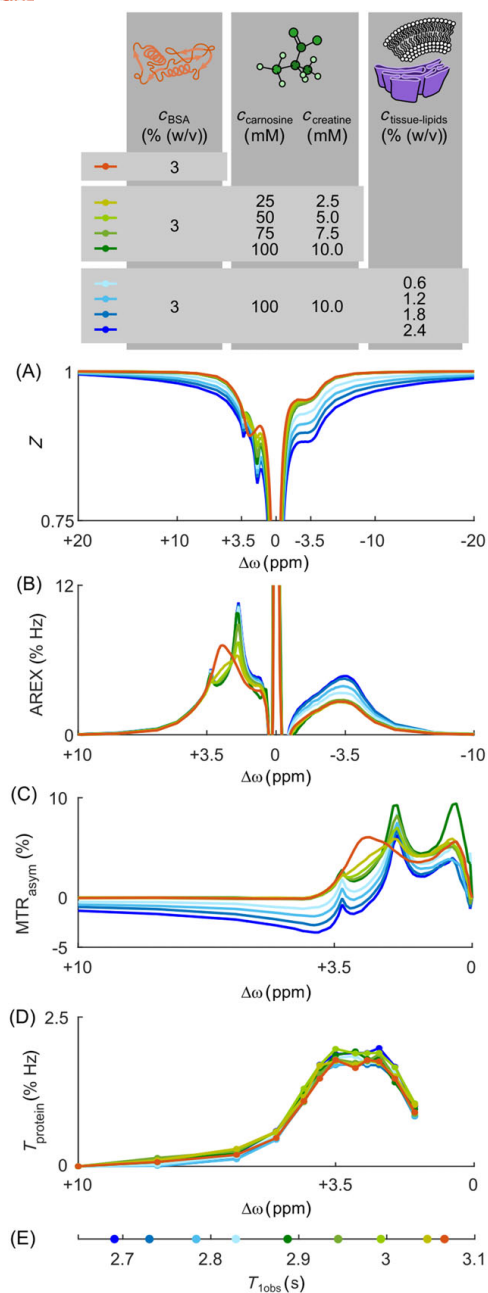


FIGURE 5 Assignment of the dualCEST signal to mobile proteins. Z- (A), AREX (B), MTR_{asym} (C) and T-spectra (D) of BSA for varying concentrations of cellular compounds ($\Delta\omega_{\text{C}} = -3.5$ ppm, $B_1 = 1.5$ μT , $B_0 = 14.1$ T). In contrast to conventional CEST, the signal T_{protein} can unambiguously be assigned to mobile proteins. (E) With an increasing concentration of compounds, the observed longitudinal relaxation time of water $T_{1\text{obs}}$ is reduced

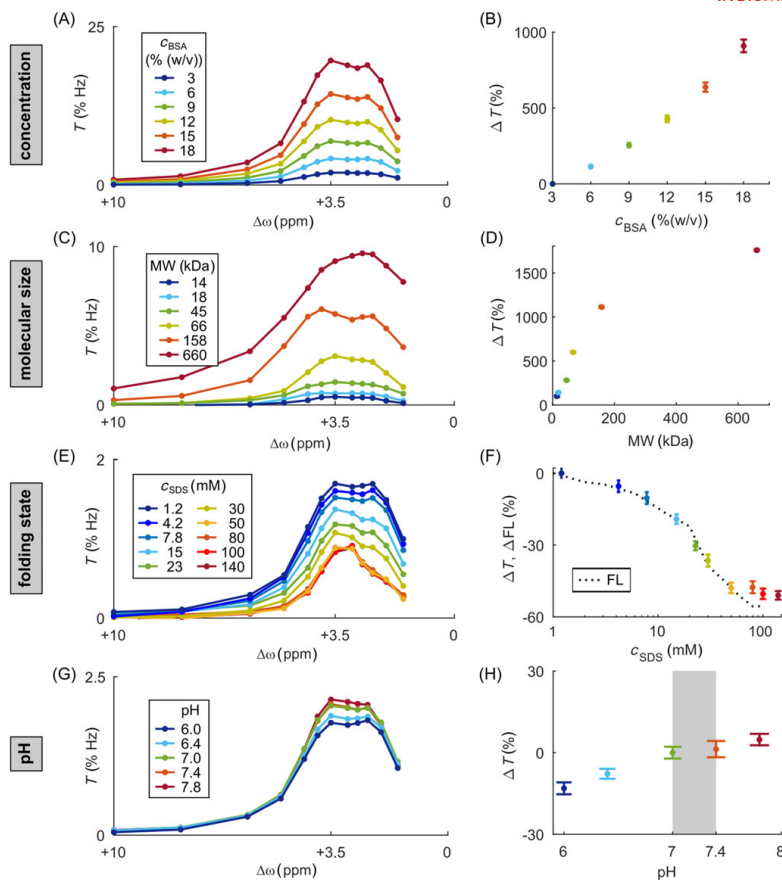


FIGURE 6 Dependence of the dualCEST signal on physiological parameters. T spectra of BSA ($\Delta\omega_C = -3.5$ ppm, $B_1 = 1.5$ μ T, $B_0 = 14.1$ T) for different concentrations (A), folding states (E) and pH (G). (C) T spectra of various globular proteins of different molecular weights (i.e. molecular sizes). (B, D, F, H) Percentage variation of T at $\Delta\omega = +3.5$ ppm. (F) As a reference, the protein folding state was monitored by fluorescence spectroscopy (FL). Signal dependencies demonstrate that variations in T can be attributed to changes in the concentration, molecular size or folding state of mobile proteins. Displayed errors are the standard deviation of repeated measurements (Table S1)

exchange properties (i.e. exchange rate). T remains constant in the physiological range between pH 7 and 7.4 (Figure 6H, gray-shaded area), but seems to be slightly affected by a decreasing pH. Consequently, for example, pH < 7 in the extracellular tumor environment can have an influence on the dualCEST signal of secreted proteins. Deviations at acidic pH values might be a result of either the pH dependence of the chemical exchange between exchangeable protons in BSA and water,^{3,44} or the overall BSA conformation which is also dependent on pH.^{41,45}

Thus, in the physiological pH range, the dualCEST signal exclusively depends on the concentration, molecular size and folding state of the mobile proteins. Contributions from other cellular compounds, water relaxation properties or changes in the chemical exchange properties can be excluded. With this knowledge in hand, the dualCEST approach was utilized to investigate alterations of the mobile fraction of the proteome in a glioblastoma brain tumor.

3.4 | Application of dualCEST *in vivo*

For examinations in humans, the dualCEST pulse sequence was implemented on a clinical 3-T MR scanner. Transfer of the dualCEST approach to lower B_0 , while maintaining its specificity to mobile proteins, is enabled by the newly introduced dimension of selectivity. As for the NMR spectrometer (Figure 3), pre-saturation parameters were optimized for the MR scanner to maximize the signal strength T , while avoiding excessive broadening of the signals. $t_p = 20$ ms and $B_1 = 2$ μ T were found to be optimal at $B_0 = 3$ T. In addition, the dualCEST signal is approximately linear

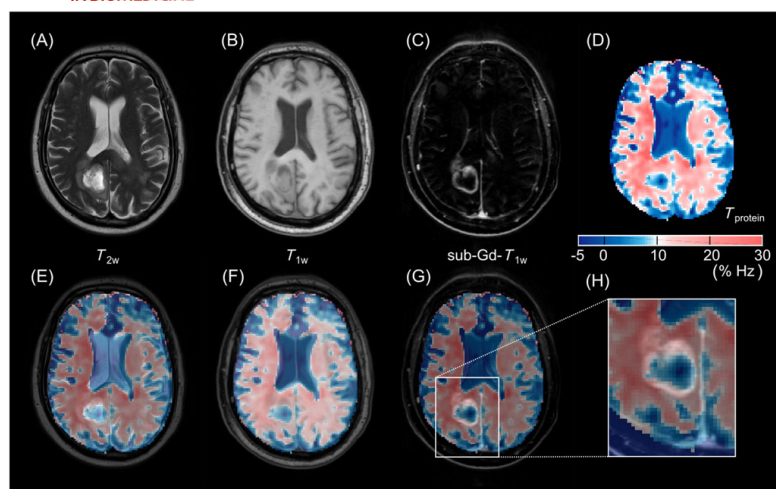


FIGURE 7 *In vivo* dualCEST examination at $B_0 = 3$ T. Multi-modal MR images of a patient with glioblastoma. (A–C) Conventional MR contrasts: T_2 -weighted (T_{2w}), T_1 -weighted (T_{1w}) and subtracted gadolinium contrast-enhanced T_1 -weighted (sub-Gd- T_{1w}) MR images. (D) The selective dualCEST signal of mobile proteins T_{protein} , showing substantial alterations of the mobile fraction of the proteome in the tumor region. (E–H) Fusion of conventional MR contrasts and the dualCEST image

as a function of B_1 for the aforementioned parameters (Supporting Information Figure S3), allowing for a simple correction of B_1 inhomogeneities in living tissue. However, a correction for B_0 inhomogeneities is not necessary because of the comparatively broad plateau of the dualCEST resonance at 3 T around its maximum (Figure 3I, red line). To maximize the range of tolerable B_0 inhomogeneities, the frequency offsets for mobile protein signals in Equation 2 were adjusted from ± 3.5 to ± 5 ppm. Moreover, the frequency offsets for ssMT signals were adjusted from ± 10 to ± 30 ppm to allow an isolated sampling of the ssMT component without contributions from mobile protein signals also at 3 T (Figure 3). Finally, the far off-resonant frequency offset in Equation 1 was adjusted from 150 to 300 ppm.

Isolated endogenous bulk mobile protein MRI of a patient with glioblastoma shows a significantly reduced signal T_{protein} in the necrotic tumor region compared with normal-appearing white matter (Figure 7H). Edges are clearly defined and show a good correlation with the inner part of the ring enhancement in the contrast media-enhanced image. The amplitude of T_{protein} in necrotic tissue is comparable with the values in cerebrospinal fluid (CSF), suggesting a considerable degeneration of the mobile fraction of the proteome in the tumor core. The specificity to mobile proteins allows the assignment of the observed signal drop to a reduced concentration, a reduced average molecular size or a denatured global folding state of bulk mobile proteins. Correct functioning of the dualCEST measurement is confirmed by signal values around zero in the CSF, where a negligible concentration of proteins can be assumed. Anatomical structures between brain matter and peripheral CSF show a good correlation with T_{protein} . In a region of interest analysis, differences in T_{protein} between gray and white matter are marginal, confirming the absence of contributions from lipids to the dualCEST signal. The equivalent signal in these two tissues is in line with data from MR spectroscopy when analyzing macromolecular resonances that are associated with bulk mobile proteins,⁴⁶ as well as rNOE-CEST signals evaluated by the variable delay multi-pulse (VDMP) method.⁴⁷ Overall, the presented *in vivo* image data verify the feasibility of dualCEST examinations in humans, enabling further investigations of the mobile fraction of the proteome in diverse pathologies.

4 | DISCUSSION

In this study, a novel MRI contrast is proposed, enabling the selective detection of endogenous bulk mobile proteins in living organisms. By contrast, in conventional Z-spectra *in vivo*, the CEST signals of mobile proteins spectrally overlap with signals originating from other cellular compounds (Figure 1B). Several attempts have been made in the past to overcome this obstacle and to highlight the signal component of mobile proteins. Ideas range from multi-parametric fitting,^{17,32,48–50} to the incorporation of several types of exchange rate filters,^{24–26,47,51–53} to the suppression of confounding signals by simultaneous pre-saturation at various frequency offsets.^{30,54–56} Although these approaches work appropriately and allow the isolation of the prominent amide proton resonance at $\Delta\omega = +3.5$ ppm or the rNOE-CEST signal of aliphatic protons at around $\Delta\omega = -3.5$ ppm, the assignment of these signals exclusively to mobile proteins remains questionable. With respect to the amide proton signal, a considerable part originates from small peptides and various metabolites.⁵⁷ In addition, the aliphatic rNOE-CEST signal comprises contributions from other mobile macromolecules, e.g. lipids or saccharides.^{16,17} In both cases, magnetization transfer rates to water are comparable with the rates occurring in mobile

proteins, thus preventing separation by exchange rate filtering. Here, we introduce a novel dimension of selectivity which is based on the cross magnetization transfer between two particular CEST signals – termed saturation crosstalk $T_{\Delta\omega_c}(\Delta\omega)$. For this purpose, the conventional CEST technique was extended to an RF irradiation scheme at two different frequency offsets. Incorporation of a saturation at an additional frequency offset was introduced for the first time in 2010.⁵⁴ In the following year, saturation with frequency-alternating RF irradiation (SAFARI) was proposed to avoid signal contributions from direct water saturation and ssMT.³⁰ In our study, an identical pre-saturation pulse scheme, but with different combinations of the two frequency offsets, is used to selectively detect the coupling between different CEST signals. The detection of the coupling between the CEST signal of amide and aliphatic protons provides a unique specificity to mobile proteins. In contrast, immobile proteins, such as cytoskeletal or membrane proteins, do not contribute to T_{protein} , as immobile proteins show comparatively broad signals with linewidths of several 10 ppm,⁵⁷ which are suppressed by the proposed ssMT correction method. As is commonly known, proton transversal relaxation times (T_2) of immobile solid-like structures are very short (on the order of 10 μ s) in comparison with the T_2 values of mobile molecules (several 10 ms). As the linewidths of CEST signals inversely depend on T_2 ,⁵⁸ proteins can be roughly classified by their mobility into two types – mobile and immobile.⁸ The specificity of the dualCEST signal to mobile proteins was verified experimentally by the successive addition of different cellular compounds to a protein model solution (Figure 5). Moreover, we demonstrated that the dualCEST signal is intrinsically corrected for changes in water relaxation (i.e. $T_{1\text{obs}}$, Figure 5D), as well as robust against changes in the chemical exchange properties in the physiologically relevant range (i.e. pH, Figure 6H). Parameters that affect the amplitude of the dualCEST signal are the concentration, molecular size and folding state of mobile proteins (Figure 6), making dualCEST a valuable diagnostic tool to detect aberrant proteomes *in vivo*.

The largest drawback of the method is the inherently smaller SNR in comparison with conventional CEST. The reason for this is the quite large number of nine Z-values required for the calculation of the isolated mobile protein signal T_{protein} (Equation 2). However, the newly introduced dimension of selectivity opens up new possibilities to overcome this limitation. As the specificity of the dualCEST signal to mobile proteins relies on the coupling of two signals, rather than on the resolution of individual resonances, high spectral resolutions are not required. This allows the application of high B_1 values to increase the signal strength without a loss of specificity (Figure 3H). In contrast, the spectral selectivity clearly deteriorates when acquiring conventional Z-spectra using high B_1 because of extensive peak broadening. Other possibilities to further amplify the dual CEST signal were found to be the reduction in t_p (Figure 3F) and B_0 (Figure 3J). The signal amplification at shorter t_p can be attributed to the expansion of the spectral bandwidth of the pre-saturation pulses and the concomitant incorporation of more protons from neighboring chemical shifts into the measurement procedure. This is because, in proteins, the chemical shift of identical proton types (e.g. amides) is dispersed, depending on their location inside the protein and the respective chemical environment.⁵⁹ In a similar manner, the number of saturated protons, and thus the signal strength, is also increased by reducing the spectral resolution (i.e. reducing B_0). Consequently, the dualCEST signal profits from lower magnetic field strengths, paving the way for dualCEST examinations on clinical MR scanners. In this study, *in vivo* measurements were performed at a magnetic field strength of 3 T and optimized to maximize the signal amplitude, while avoiding an excessive broadening of the signals. Linewidths broader than the distance between the two frequency offsets $\Delta\omega$ and $\Delta\omega_c$ might cause a direct saturation of CEST signals at one frequency offset induced by pulses applied at the other. This might influence the signal preparation, leading to disturbed dualCEST signals. However, the utilized distance of 10 ppm at 3 T between $\Delta\omega$ and $\Delta\omega_c$ should be sufficient to avoid such influences, assuming that the linewidths of the individual CEST pools do not exceed 20 ppm. These features should have allowed the acquisition of dualCEST images with adequate SNR. However, there were technical limitations of the MR scanner used in this work which prevented a pre-saturation with an ideal DC of 50% (please note: these limitations were caused by the restricted amplifier performance and not the specific absorption rate, SAR). Instead, only a DC of approximately half the desired value could be realized, which is why several repetitions were required to acquire a reliable dualCEST image *in vivo*.

For repeated measurements, the dualCEST approach profits from a fast and direct acquisition. By 'direct', we mean that $T_{\Delta\omega_c}(\Delta\omega)$ can be calculated from unprocessed data without the application of any fitting procedure to approximate the direct water saturation or ssMT. This allows a fast determination of the dualCEST signal without the need for the sampling of an entire spectrum, leading to a considerable saving in acquisition time. Exclusion of the fitting procedure was enabled by an analytical description based on the AREX³⁶ evaluation (Figure S1). In this theory, $T_{\Delta\omega_c}(\Delta\omega)$ is a correction term – considering the exchange of magnetization between two different CEST pools – which is added to the longitudinal relaxation rate in the rotating frame R_{1p} of a multi-pool system.^{58,60,61} The validity of the analytical model requires a saturation length in compliance with the criterion for steady state (Figure 3B). In addition, the tilt angle θ of the effective field and the z-axis must be small in

compliance with: $\cos^2\theta = \frac{\Delta\omega^2}{\Delta\omega^2 + (\gamma B_1)^2} \approx 1$.^{21,36,58} This limits the evaluation of signals at small $\Delta\omega$ when applying comparatively high B_1 . Violation

of this assumption leads to strong signal distortions, as observed at $\Delta\omega < 2.75$ ppm when acquiring signals at $B_0 = 3$ T and $B_1 = 2$ μ T (Figure 3I, red line). The saving in acquisition time allowed the repetition of the acquisitions to accumulate sufficient SNR for dualCEST examinations of a brain tumor patient without impractical lengthening of the measurement time.

The dualCEST approach allows the identification of pathological modifications of the mobile fraction of the proteome *in vivo*. Significant changes in the isolated mobile protein signal T_{protein} were detected in the necrotic region of a human brain tumor (Figure 7). Necrotic tissue is known to consist of decomposing or dead cells, verifying the ability of the dualCEST signal to detect aberrant proteomes in living organisms. In the future, whole cohorts of patients will need to be examined to reliably determine the actual contribution of mobile proteins to CEST signal changes in different pathologies, and to further investigate the diagnostic value of the presented method. As T_{protein} is a quantitative value, a comparison between different subjects is possible. Applications range from staging and follow-up studies of cancer treatment to the diagnosis of neurodegenerative diseases associated with the accumulation of pathogenic protein plaques, e.g. Alzheimer's disease. In addition, the dualCEST

approach should be particularly suitable for the selective detection of binding mechanisms of mobile proteins, as its specificity relies on the coupling of different CEST signals. In this context, selective imaging of small exogenous CEST agents binding to mobile proteins is plausible because of the immobilization of the small molecules and the resulting intermolecular magnetization transfer pathway.⁶²

5 | CONCLUSIONS

A novel MRI technique – termed dualCEST – is proposed, allowing the selective detection of endogenous bulk mobile proteins in humans. In this study, for the first time, the coupling of different CEST signals mediated by intramolecular spin diffusion is exploited to introduce an exceptional specificity into the CEST experiment. The specificity of the dualCEST signal to bulk mobile proteins was verified experimentally by the investigation of different cellular compounds under different physiological conditions. A fast and direct acquisition of the dualCEST signal was enabled by an analytical description of the dualCEST signal. With regard to applications in humans, the dualCEST signal was maximized by a comprehensive study of diverse technical parameters. Remarkably, it was found that the dualCEST signal profits from lower magnetic field strengths, allowing a straightforward implementation of dualCEST examinations on clinical MR scanners. The applicability of the dualCEST technique for examinations in humans was verified in a proof-of-principle study of a brain tumor patient at 3 T.

ACKNOWLEDGEMENTS

We cordially thank Enza di Gregorio and Francesca Garello from the Department of Molecular Biotechnology and Health Sciences at the University of Turin in Italy for the extraction of lipids and liposome preparation. The authors declare no conflicts of interest.

ORCID

Steffen Goerke  <http://orcid.org/0000-0002-0684-2423>

Moritz Zaiss  <http://orcid.org/0000-0001-9780-3616>

Dario L. Longo  <http://orcid.org/0000-0002-6906-9925>

REFERENCES

1. Wolff SD, Balaban RS. NMR imaging of labile proton exchange. *J Magn Reson.* 1990;86:164-169.
2. Ward KM, Balaban RS. Determination of pH using water protons and chemical exchange dependent saturation transfer (CEST). *Magn Reson Med.* 2000;44:799-802.
3. Zhou J, van Zijl PCM. Chemical exchange saturation transfer imaging and spectroscopy. *Prog Nucl Magn Reson Spectrosc.* 2006;48:109-136.
4. McMahon MT, Gilad AA, Bulte JWM, van Zijl PCM. *Chemical Exchange Saturation Transfer Imaging: Advances and Applications.* 1st ed. Singapore: Pan Stanford Publishing Pte Ltd; 2017.
5. van Zijl PCM, Lam WW, Xu J, Knutsson L, Stanisz GJ. Magnetization transfer contrast and chemical exchange saturation transfer MRI. Features and analysis of the field-dependent saturation spectrum. *NeuroImage.* 2017;168:222-241.
6. Zhou J, Payen J-F, Wilson DA, Traystman RJ, van Zijl PCM. Using the amide proton signals of intracellular proteins and peptides to detect pH effects in MRI. *Nat Med.* 2003;9:1085-1090.
7. Zhou J, Lal B, Wilson DA, Laterra J, van Zijl PCM. Amide proton transfer (APT) contrast for imaging of brain tumors. *Magn Reson Med.* 2003;50:1120-1126.
8. Yan K, Fu Z, Yang C, et al. Assessing amide proton transfer (APT) MRI contrast origins in 9 L gliosarcoma in the rat brain using proteomic analysis. *Mol Imaging Biol.* 2015;17:479-487.
9. Zaiss M, Windschuh J, Goerke S, et al. Downfield-NOE-suppressed amide-CEST-MRI at 7 Tesla provides a unique contrast in human glioblastoma. *Magn Reson Med.* 2017;77:196-208.
10. Cai K, Haris M, Singh A, et al. Magnetic resonance imaging of glutamate. *Nat Med.* 2012;18:302-307.
11. Haris M, Nanga RPR, Singh A, et al. Exchange rates of creatine kinase metabolites: feasibility of imaging creatine by chemical exchange saturation transfer MRI. *NMR Biomed.* 2012;25:1305-1309.
12. Rerich E, Zaiss M, Korzowski A, Ladd ME, Bachert P. Relaxation-compensated CEST-MRI at 7 T for mapping of creatine content and pH – preliminary application in human muscle tissue *in vivo.* *NMR Biomed.* 2015;28:1402-1412.
13. Chan KWY, McMahon MT, Kato Y, et al. Natural D-glucose as a biodegradable MRI contrast agent for detecting cancer. *Magn Reson Med.* 2012;68:1764-1773.
14. Walker-Samuel S, Ramasawmy R, Torrealdea F, et al. In vivo imaging of glucose uptake and metabolism in tumors. *Nat Med.* 2013;19:1067-1072.
15. Schuenke P, Paech D, Koehler C, et al. Fast and quantitative T1ρ-weighted dynamic glucose enhanced MRI. *Sci Rep.* 2017;7:42093.
16. van Zijl PCM, Zhou J, Mori N, Payen J-F, Wilson D, Mori S. Mechanism of magnetization transfer during on-resonance water saturation. a new approach to detect mobile proteins, peptides, and lipids. *Magn Reson Med.* 2003;49:440-449.
17. Jones CK, Huang A, Xu J, et al. Nuclear Overhauser enhancement (NOE) imaging in the human brain at 7 T. *Neuroimage.* 2013;77:114-124.
18. Henkelman RM, Stanisz GJ, Graham SJ. Magnetization transfer in MRI: a review. *NMR Biomed.* 2001;14:57-64.
19. Henkelman RM, Huang X, Xiang Q-S, Stanisz GJ, Swanson SD, Bronskill MJ. Quantitative interpretation of magnetization transfer. *Magn Reson Med.* 1993;29:759-766.
20. Zaiss M, Zu Z, Xu J, et al. A combined analytical solution for chemical exchange saturation transfer and semi-solid magnetization transfer. *NMR Biomed.* 2015;28:217-230.

21. Goerke S, Zaiss M, Bachert P. Characterization of creatine guanidinium proton exchange by water-exchange (WEX) spectroscopy for absolute-pH CEST imaging in vitro. *NMR Biomed.* 2014;27:507-518.
22. Liepinsh E, Otting G. Proton exchange rates from amino acid side chains—implications for image contrast. *Magn Reson Med.* 1996;35:30-42.
23. Bai Y, Milne JS, Mayne L, Englander SW. Primary structure effects on peptide group hydrogen exchange. *Proteins Struct Funct Genet.* 1993;17:75-86.
24. Friedman JI, McMahon MT, Stivers JT, van Zijl PCM. Indirect detection of labile solute proton spectra via the water signal using frequency-labeled exchange (FLEX) transfer. *J Am Chem Soc.* 2010;132:1813-1815.
25. Zu Z, Janve VA, Xu J, Does MD, Gore JC, Gochberg DF. A new method for detecting exchanging amide protons using chemical exchange rotation transfer. *Magn Reson Med.* 2013;69:637-647.
26. Xu J, Yadav NN, Bar-Shir A, et al. Variable delay multi-pulse train for fast chemical exchange saturation transfer and relayed-nuclear Overhauser enhancement MRI. *Magn Reson Med.* 2014;71:1798-1812.
27. Jones CK, Schlosser MJ, van Zijl PCM, Pomper MG, Golay X, Zhou J. Amide proton transfer imaging of human brain tumors at 3T. *Magn Reson Med.* 2006;56:585-592.
28. Wen Z, Hu S, Huang F, et al. MR imaging of high-grade brain tumors using endogenous protein and peptide-based contrast. *Neuroimage.* 2010;51:616-622.
29. Jia G, Abaza R, Williams JD, et al. Amide proton transfer MR imaging of prostate cancer: a preliminary study. *J Magn Reson Imaging.* 2011;33:647-654.
30. Scheidegger R, Vinogradov E, Alsop DC. Amide proton transfer imaging with improved robustness to magnetic field inhomogeneity and magnetization transfer asymmetry using saturation with frequency alternating RF irradiation. *Magn Reson Med.* 2011;66:1275-1285.
31. Zhou J, Yan K, Zhu H. A simple model for understanding the origin of the amide proton transfer MRI signal in tissue. *Appl Magn Reson.* 2012;42:393-402.
32. Zaiss M, Windschuh J, Paech D, et al. Relaxation-compensated CEST-MRI of the human brain at 7 T: unbiased insight into NOE and amide signal changes in human glioblastoma. *Neuroimage.* 2015;112:180-188.
33. Heo H-Y, Jones CK, Hua J, et al. Whole-brain amide proton transfer (APT) and nuclear Overhauser enhancement (NOE) imaging in glioma patients using low-power steady-state pulsed chemical exchange saturation transfer (CEST) imaging at 7T. *J Magn Reson Imaging.* 2016;44:41-50.
34. Zhou J, Tryggstad E, Wen Z, et al. Differentiation between glioma and radiation necrosis using molecular magnetic resonance imaging of endogenous proteins and peptides. *Nat Med.* 2011;17:130-134.
35. Mehrabian H, Desmond KL, Soliman H, Sahgal A, Stanisz GJ. Differentiation between radiation necrosis and tumor progression using chemical exchange saturation transfer. *Clin Cancer Res.* 2017;23:3667-3675.
36. Zaiss M, Xu J, Goerke S, et al. Inverse Z-spectrum analysis for spillover-, MT-, and T1-corrected steady-state pulsed CEST-MRI – application to pH-weighted MRI of acute stroke. *NMR Biomed.* 2014;27:240-252.
37. Windschuh J, Zaiss M, Meissner J-E, et al. Correction of B1-inhomogeneities for relaxation-compensated CEST imaging at 7 T. *NMR Biomed.* 2015;28:529-537.
38. Schuenke P, Windschuh J, Roeloffs V, Ladd ME, Bachert P, Zaiss M. Simultaneous mapping of water shift and B1 (WASABI)—application to field-inhomogeneity correction of CEST MRI data. *Magn Reson Med.* 2017;77:571-580.
39. Neuhaus D, Williamson MP. *The Nuclear Overhauser Effect in Structural and Conformational Analysis.* New York: Wiley; 1989.
40. van Zijl PCM, Yadav NN. Chemical exchange saturation transfer (CEST): what is in a name and what isn't? *Magn Reson Med.* 2011;65:927-948.
41. Barbosa LRS, Ortore MG, Spinozzi F, Mariani P, Bernstorff S, Itri R. The importance of protein-protein interactions on the pH-induced conformational changes of bovine serum albumin: a small-angle X-ray scattering study. *Biophys J.* 2010;98:147-157.
42. Zaiss M, Kunz P, Goerke S, Radbruch A, Bachert P. MR imaging of protein folding in vitro employing nuclear-Overhauser-mediated saturation transfer. *NMR Biomed.* 2013;26:1815-1822.
43. Longo DL, Gregorio ED, Abategiovanni R, et al. Chemical exchange saturation transfer (CEST): an efficient tool for detecting molecular information on proteins' behaviour. *Analyst.* 2014;139:2687-2690.
44. Goerke S, Zaiss M, Kunz P, et al. Signature of protein unfolding in chemical exchange saturation transfer imaging. *NMR Biomed.* 2015;28:906-913.
45. Lin VJC, Koenig JL. Raman studies of bovine serum albumin. *Biopolymers.* 1976;15:203-218.
46. Snoussi K, Gillen JS, Horska A, et al. Comparison of brain gray and white matter macromolecule resonances at 3 and 7 Tesla. *Magn Reson Med.* 2015;74:607-613.
47. Xu X, Yadav NN, Zeng H, et al. Magnetization transfer contrast-suppressed imaging of amide proton transfer and relayed nuclear Overhauser enhancement chemical exchange saturation transfer effects in the human brain at 7T. *Magn Reson Med.* 2016;75:88-96.
48. Desmond KL, Moosvi F, Stanisz GJ. Mapping of amide, amine, and aliphatic peaks in the CEST spectra of murine xenografts at 7 T. *Magn Reson Med.* 2013;71:1841-1853.
49. Heo H-Y, Zhang Y, Lee D-H, Hong X, Zhou J. Quantitative assessment of amide proton transfer (APT) and nuclear Overhauser enhancement (NOE) imaging with extrapolated semi-solid magnetization transfer reference (EMR) signals: application to a rat glioma model at 4.7 tesla. *Magn Reson Med.* 2016;75:137-149.
50. Zhou IY, Wang E, Cheung JS, Zhang X, Fulci G, Sun PZ. Quantitative chemical exchange saturation transfer (CEST) MRI of glioma using Image Downsampling Expedited Adaptive Least-squares (IDEAL) fitting. *Sci Rep.* 2017;7:84.
51. Zu Z, Janve VA, Li K, Does MD, Gore JC, Gochberg DF. Multi-angle ratiometric approach to measure chemical exchange in amide proton transfer imaging. *Magn Reson Med.* 2012;68:711-719.
52. Xu J, Chan KWY, Xu X, Yadav N, Liu G, van Zijl PCM. On-resonance variable delay multipulse scheme for imaging of fast-exchanging protons and semisolid macromolecules. *Magn Reson Med.* 2017;77:730-739.
53. Lin C-Y, Yadav NN, Friedman JI, Ratnakar J, Sherry AD, van Zijl PCM. Using frequency-labeled exchange transfer to separate out conventional magnetization transfer effects from exchange transfer effects when detecting ParaCEST agents. *Magn Reson Med.* 2012;67:906-911.
54. Närväinen J, Hubbard PL, Kauppinen RA, Morris GA. Z-spectroscopy with alternating-phase irradiation. *J Magn Reson.* 2010;207:242-250.
55. Lee J-S, Regatte RR, Jerschow A. Isolating chemical exchange saturation transfer contrast from magnetization transfer asymmetry under two-frequency rf irradiation. *J Magn Reson.* 2012;215:56-63.

56. Friedman JI, Xia D, Regatte RR, Jerschow A. Transfer rate edited experiment for the selective detection of chemical exchange via saturation transfer (TRE-CEST). *J Magn Reson.* 2015;256:43-51.
57. Goerke S, Milde KS, Bukowiecki R, et al. Aggregation-induced changes in the chemical exchange saturation transfer (CEST) signals of proteins. *NMR Biomed.* 2017;30:e3665.
58. Zaiss M, Bachert P. Chemical exchange saturation transfer (CEST) and MR Z-spectroscopy in vivo: a review of theoretical approaches and methods. *Phys Med Biol.* 2013;58:R221-R269.
59. Wüthrich K. *NMR of Proteins and Nucleic Acids.* New York: John Wiley & Sons; 1986.
60. Zaiss M, Bachert P. Exchange-dependent relaxation in the rotating frame for slow and intermediate exchange – modeling off-resonant spin-lock and chemical exchange saturation transfer. *NMR Biomed.* 2013;26:507-518.
61. Trott O, Palmer AG III. Theoretical study of R1 ρ rotating-frame and R2 free-precession relaxation in the presence of n-site chemical exchange. *J Magn Reson.* 2004;170:104-112.
62. Yadav NN, Yang X, Li Y, Li W, Liu G, Zijl PCM. Detection of dynamic substrate binding using MRI. *Sci Rep.* 2017;7:10138.

SUPPORTING INFORMATION

Additional Supporting Information may be found online in the supporting information tab for this article.

How to cite this article: Goerke S, Breitling J, Zaiss M, et al. Dual-frequency irradiation CEST-MRI of endogenous bulk mobile proteins. *NMR in Biomedicine.* 2018;31:e3920. <https://doi.org/10.1002/nbm.3920>

Publication II

Relaxation-compensated APT and rNOE CEST-MRI of human brain tumors at 3 T






Authors: Steffen Goerke, Yannick Soehngen, Anagha Deshmane, Moritz Zaiss, **Johannes Breitling**, Philip S. Boyd, Kai Herz, Ferdinand Zimmermann, Karel D. Klika, Heinz-Peter Schlemmer, Daniel Paech, Mark E. Ladd, and Peter Bachert

Journal reference: Magnetic Resonance in Medicine. 2019;82:622-632.

DOI: 10.1002/mrm.27751

Author contributions: SG designed the study together with **JB**. AD, MZ and KH provided the utilized MR sequence. YS performed the experiments with support of PSB and evaluated the data. SG, YS and **JB** interpreted the results and optimized accordingly the imaging parameters and the utilized fit model. KDK provided technical support for the NMR spectrometer experiments. DP was responsible for the patient enrollment and medical supervision during the study. SG drafted and revised the manuscript with critical review from all co-authors.

Relaxation-compensated APT and rNOE CEST-MRI of human brain tumors at 3 T

Steffen Goerke¹  | Yannick Soehngen^{1,2} | Anagha Deshmane³  | Moritz Zaiss³  | Johannes Breitling^{1,2,4}  | Philip S. Boyd^{1,2} | Kai Herz³ | Ferdinand Zimmermann^{1,2} | Karel D. Klika⁵ | Heinz-Peter Schlemmer^{6,7} | Daniel Paech⁶  | Mark E. Ladd^{1,2,7} | Peter Bachert^{1,2}

¹Division of Medical Physics in Radiology, German Cancer Research Center, Heidelberg, Germany

²Faculty of Physics and Astronomy, University of Heidelberg, Heidelberg, Germany

³Department of High-Field Magnetic Resonance, Max-Planck-Institute for Biological Cybernetics, Tübingen, Germany

⁴Max-Planck-Institute for Nuclear Physics, Heidelberg, Germany

⁵Molecular Structure Analysis, German Cancer Research Center, Heidelberg, Germany

⁶Department of Radiology, German Cancer Research Center, Heidelberg, Germany

⁷Faculty of Medicine, University of Heidelberg, Heidelberg, Germany

Correspondence

Steffen Görke, Division of Medical Physics in Radiology, German Cancer Research Center, Im Neuenheimer Feld 223, 69120 Heidelberg, Baden-Württemberg, Germany. Email: s.goerke@dkfz.de

Purpose: Relaxation-compensated CEST-MRI (i.e., the inverse metrics magnetization transfer ratio and apparent exchange-dependent relaxation) has already been shown to provide valuable information for brain tumor diagnosis at ultrahigh magnetic field strengths. This study aims at translating the established acquisition protocol at 7 T to a clinically relevant magnetic field strength of 3 T.

Methods: Protein model solutions were analyzed at multiple magnetic field strengths to assess the spectral widths of the amide proton transfer and relayed nuclear Overhauser effect (rNOE) signals at 3 T. This prior knowledge of the spectral range of CEST signals enabled a reliable and stable Lorentzian-fitting also at 3 T where distinct peaks are no longer resolved in the Z-spectrum. In comparison to the established acquisition protocol at 7 T, also the image readout was extended to three dimensions.

Results: The observed spectral range of CEST signals at 3 T was approximately ± 15 ppm. Final relaxation-compensated amide proton transfer and relayed nuclear Overhauser effect contrasts were in line with previous results at 7 T. Examination of a patient with glioblastoma demonstrated the applicability of this acquisition protocol in a clinical setting.

Conclusion: The presented acquisition protocol allows relaxation-compensated CEST-MRI at 3 T with a 3D coverage of the human brain. Translation to a clinically relevant magnetic field strength of 3 T opens the door to trials with a large number of participants, thus enabling a comprehensive assessment of the clinical relevance of relaxation compensation in CEST-MRI.

KEYWORDS

APAT, cancer, CEST, MRI, proteins, rNOE

1 | INTRODUCTION

Chemical exchange saturation transfer (CEST)^{1,2} is an emerging MRI technique for the detection of organic compounds present in low concentration in living tissue such as proteins and peptides³⁻⁵ or various metabolites (e.g., glucose,⁶⁻⁸ creatine,⁹⁻¹² glutamate¹³⁻¹⁵). The potential to obtain information at the molecular level with a spatial resolution comparable to conventional MRI makes CEST a promising imaging technique for the detection of a diversity of diseases and especially for cancer.

The most commonly used CEST technique for tumor imaging is amide proton transfer (APT) imaging,^{3,16,17} which uses the asymmetry analysis (MTR_{asym}) to correct for symmetric direct water saturation (DS) effects and to detect the CEST signal of amide protons located in the backbone of proteins and peptides. APT-CEST-MRI at 3 T has already been shown to provide information of high clinical relevance, like tumor grading,^{18,19} or differentiation of radiation necrosis and tumor progression.^{20,21} However, over the past few years, concerns about concomitant effects competing with the actual APT signal have arisen. Investigations at higher magnetic field strengths (B_0) identified superimposing contributions originating from the relayed nuclear Overhauser effect^{22,23} (rNOE) as well as from semisolid magnetization transfer^{23,24} (ssMT). In addition, theoretical descriptions showed that CEST signals are intrinsically diluted by spillover effects leading to an interfering dependence on the water relaxation properties (i.e., the longitudinal and transversal relaxation rate of water R_1 and R_2).²⁵⁻²⁷

Relaxation-compensated CEST-MRI (i.e., the inverse metrics MTR_{Relax} ^{25,26} and $AREX$ ²⁷) (Equations 2 and 3) in combination with a multipool Lorentzian-fit analysis to separate the individual CEST signals (e.g., APT, rNOE) provides a means to evade such spillover effects.^{28,29} The unraveling of the different CEST signals and compensation for competing relaxation effects is particularly promising with regard to an increase in specificity for the identification of new biomarkers. At 7 T, relaxation-compensated CEST-MRI of the APT and rNOE signals has already been shown to provide additional features that are not visible in uncorrected CEST images or conventional MRI.^{29,30} Moreover, relaxation-compensated CEST-MRI at 7 T has recently been applied to various neuro-oncological clinical questions, which demonstrated the potential to differentiate histologic and genetic subtypes of glioma,³¹ as well as to allow early assessment³² and prognostication³³ of treatment response in patients with

glioblastoma. Although similar clinical questions have also been reported to be accessible by uncorrected CEST-MRI at 3 T,³⁴⁻³⁷ it appears that relaxation-compensated CEST-MRI provides higher diagnostic accuracy. Nevertheless, the actual clinical relevance of relaxation compensation in CEST-MRI remains to be investigated in detail. Thus, the aim of this study was to translate the established acquisition protocol for relaxation-compensated CEST-MRI at 7 T²⁹ to a clinically relevant magnetic field strength of 3 T. This would open the door to clinical trials with larger patient cohorts, thus enabling a comprehensive assessment of the clinical relevance of relaxation compensation in CEST-MRI. In addition, the translation to 3 T would also allow excluding magnetic field-dependent biases for comparison to APT-weighted MRI.³⁴

At 3 T, distinct peaks for the APT and rNOE signals are not resolved in the Z-spectrum.³⁷⁻³⁹ Consequently, a strong variability of fit parameters is observed when applying a multipool Lorentzian-fit procedure. In this study, reliable and stable fitting of the APT and rNOE signals at 3 T has been realized by adjusting the fit parameters (i.e., start values and borders) of the spectral widths of CEST signals to significantly larger values in comparison to previous reports.³⁸⁻⁴⁰ This is based on an investigation of protein model solutions at multiple magnetic field strengths (i.e., $B_0 = 3$ T, 7 T, and 14.1 T) demonstrating a spectral range of CEST signals at 3 T of approximately ± 15 ppm (Figure 1A).

In comparison to the established acquisition protocol for relaxation-compensated CEST-MRI at 7 T, the image readout was extended to three dimensions using the snapshot-CEST approach,^{39,41} which allows adequate coverage of the tumor volume. The feasibility of applying this acquisition protocol in a clinical setting is demonstrated by examination of a patient with newly diagnosed glioblastoma. Similar CEST contrasts to those obtained at ultrahigh magnetic field strengths were observed.²⁹ Overall, we were able to successfully translate relaxation-compensated CEST-MRI to a clinically relevant magnetic field strength of 3 T, thereby allowing a comprehensive assessment of relaxation compensation in CEST-MRI.

2 | METHODS

2.1 | CEST metrics

The Z-spectrum is defined as the normalized water magnetization (M_{sat}) after presaturation at a frequency offset ($\Delta\omega$):

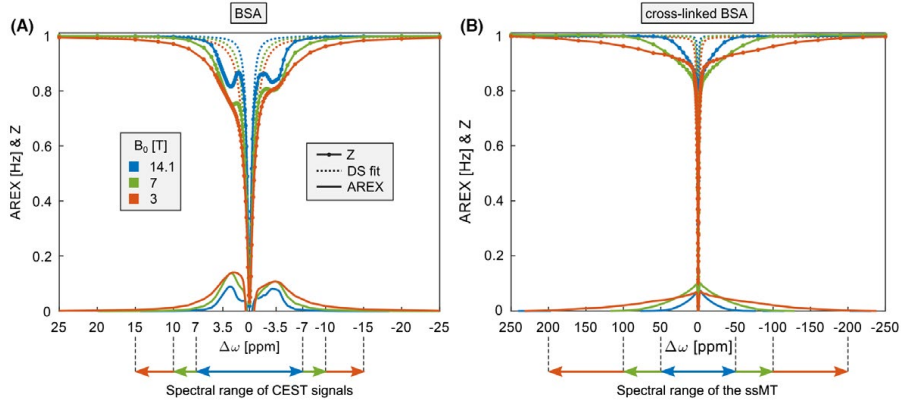


FIGURE 1 Z-spectra and AREX spectra ($B_1 = 0.75 \mu\text{T}$) of bovine serum albumin (BSA) (A) and cross-linked BSA (B) at multiple B_0 . As B_0 decreases, the spectral range of CEST signals and semisolid magnetization transfer (ssMT) broadens substantially (colored arrows). The direct water-saturation (DS) fits for calculation of the AREX spectra are indicated with dashed lines

$Z(\Delta\omega) = \frac{M_{sat}(\Delta\omega)}{M_0}$, where M_0 is the equilibrium water magnetization. Application of a multipool Lorentzian-fit procedure allows defining a labeled Z-spectrum (Z_{lab}) and a reference Z-spectrum (Z_{ref}) for each individual pool.²⁹ Z_{lab} consists of all fitted pools, whereas the pool of interest is excluded for Z_{ref} . Consequently, calculation of a CEST effect of interest is, in principle, possible by calculating the Lorentzian difference (LD)²³:

$$LD = Z_{ref} - Z_{lab} \quad (1)$$

However, subtraction of the Z-values in Equation 1 does not account for spillover effects that dilute the actual CEST effect, depending on the vertical position of the Z-values along the Z-axis.^{25,26} Consequently, LD depends not only on the actual CEST effect, but also on the water relaxation properties (i.e., R_1 and R_2 of water) as well as on other magnetization transfer signals that are present in the spectral region of interest (e.g., ssMT). In the steady state (i.e., saturation duration $t_{sat} \gg T_1$), a compensation for such spillover effects can be achieved by using the inverse magnetization transfer ratio (MTR_{Rex})^{25,26}:

$$MTR_{Rex} = \frac{1}{Z_{lab}} - \frac{1}{Z_{ref}} \quad (2)$$

In addition, a compensation for the scaling of all CEST effects by the T_1 relaxation of water is possible by the apparent exchange-dependent relaxation ($AREX$)²⁷:

$$AREX = R_1 \cdot MTR_{Rex} \quad (3)$$

2.2 | In vivo CEST-MRI

2.2.1 | Subjects

One patient with newly diagnosed glioblastoma (WHO grade IV) was examined before therapy. In addition, one healthy volunteer was examined several times for optimization of the pulse-sequence parameters. Examinations were approved by the local ethics committee of the Medical Faculty of the University of Heidelberg and are in accordance with the relevant guidelines and regulations. Written informed consent was received from the subjects before the examination.

2.2.2 | MRI acquisition

In vivo CEST-MRI was performed on a 3T whole-body MR scanner (MAGNETOM Prisma; Siemens Healthineers, Erlangen, Germany) using a 3D spiral-centric-reordered gradient-echo acquisition (i.e., snapshot CEST^{39,41}) and a 64-channel receive head/neck coil.

Image-readout parameters were adapted from literature³⁹ and were found to be optimal for FOV = $220 \times 179 \times 48 \text{ mm}^3$, matrix = $128 \times 104 \times 16$, resolution = $1.7 \times 1.7 \times 3 \text{ mm}^3$, GRAPPA acceleration factor = 2, TE = 2.75 ms, TR = 5.5 ms, bandwidth = 340 Hz/pixel, flip angle = 7° , and elongation factor = 0.5. The acquisition duration (t_{acq}) for one 3D image was 3.6 seconds. For optimization of the image-readout parameters, SNR maps were calculated by the ratio of $M_{sat}(-3.5 \text{ ppm})$ and the SD of $M_{sat}(-3.5 \text{ ppm})$ in an empty image area.

Presaturation was achieved by a train of 148 Gaussian-shaped RF pulses of mean amplitude $B_1 = \text{flip angle}/(\gamma \cdot t_p) = 0.6 \mu\text{T}$ or $0.9 \mu\text{T}$, length $t_p = 20$ ms, and duty cycle = 80%, resulting in an overall duration of $t_{\text{sat}} = 3.7$ seconds. The Z-spectra were sampled at 57 frequency offsets in unequal steps between ± 250 ppm (the complete list of frequency offsets is provided in the Supporting Information). For normalization, M_0 was acquired at the beginning and at the end of the CEST-image series and interpolated to obtain an individual M_0 for each presaturation cycle. The acquisition duration for collecting CEST data at two B_1 values was 7:36 minutes each.

For correction purposes, a B_0 map and a B_1 map were acquired by the WASABI⁴² (simultaneous mapping of water shift and B_1) approach and a T_1 map by the saturation recovery sequence. For both techniques, the same image-readout parameters were used as for the acquisition of CEST data. The acquisition durations for WASABI data and T_1 data were 3:41 minutes and 1:58 minutes, respectively.

2.2.3 | Data processing

All images (i.e., CEST, WASABI, and T_1 data) were co-registered using an intensity-based rigid registration algorithm in the Medical Imaging Interaction Toolkit.⁴³ To correct for B_0 inhomogeneities, Z-spectra were shifted along the $\Delta\omega$ dimension according to the acquired B_0 map and denoised using principal component analysis as previously described.³⁹

The resulting Z-spectra were fitted pixel-wise using a 4-pool Lorentzian-fit model representing the APT, rNOE, ssMT, and DS. The Lorentzian function of the DS was adjusted by a constant plateau around 0 ppm to account for the broadening of the DS due to pulsed presaturation.³⁹ A detailed description of the fit model and the optimized fit parameters (i.e., start values and borders) can be found in the Supporting Information.

The fitted Z-spectra were used for calculation of the different CEST contrasts defined in Equations 1-3. For the APT and rNOE pools, the contrasts were calculated at +3.5 and -3.5 ppm, respectively. Final CEST contrasts were corrected for B_1 inhomogeneities by means of the 2-point “contrast-correction” method as previously described⁴⁴ (reconstructed $B_1 = 0.7 \mu\text{T}$).

2.3 | In vitro CEST measurements

2.3.1 | Model systems

Two model solutions containing 15% weight-per-volume bovine serum albumin (BSA) were prepared. The solutions were buffered at pH 7 using phosphate-buffered saline. Both model solutions were prepared from highly concentrated stock solutions to ensure precise attainment of the desired concentration. In one sample, BSA was cross-linked using 30 μL per

milliliter of a 25% weight-per-weight aqueous glutaraldehyde solution. To ensure homogenous cross-linking, stock solutions were continuously stirred and chilled on ice during mixing.

2.3.2 | MRI acquisition

In vitro CEST measurements were performed at three magnetic field strengths (i.e., $B_0 = 3$ T, 7 T, and 14.1 T). For measurements at 3 T, the same setup as for in vivo measurements was used. Measurements at 7 T were also performed on a whole-body MR scanner (MAGNETOM 7 T; Siemens Healthineers) using a setup that was established in previous studies.^{29,44} Measurements at 14.1 T were performed on a narrow bore Avance II spectrometer (Bruker BioSpin, Karlsruhe-Rheinstetten, Germany) using a setup also established in previous studies.^{5,45,46} The aforementioned references also provide details for the B_0 , B_1 , and T_1 -mapping techniques used at each magnetic field strength.

The sample temperatures were stabilized at 25°C using a thermos flask containing 1.8 L water or the internal heating device for the whole-body MR scanner and the MR spectrometer, respectively.

Presaturation was achieved by a train of 84 Gaussian-shaped RF pulses of mean amplitude $B_1 = 0.75 \mu\text{T}$, $t_p = 100$ ms, and duty cycle = 56%, resulting in $t_{\text{sat}} = 15$ seconds. The Z-spectra were sampled at 107 frequency offsets in unequal steps between ± 250 ppm. Analogous to in vivo measurements, M_0 was acquired at several time points and interpolated to obtain an individual M_0 for each presaturation cycle.

2.3.3 | Data processing

The Z-spectra were corrected for B_0 inhomogeneities and fitted pixel-wise by a 1-pool Lorentzian-fit model representing the DS. To avoid contributions from CEST signals, as well as to take into account the broadening of the DS due to a pulsed presaturation for the BSA sample, data points in the range of ± 25 ppm to ± 0.6 ppm and between ± 0.3 ppm were excluded from the fitting procedure. For cross-linked BSA, data points in the range from ± 220 ppm, ± 150 ppm, or ± 80 ppm to ± 0.8 ppm at $B_0 = 14.1$ T, 7 T and 3 T, respectively, and between ± 0.3 ppm were excluded. A detailed description of the fit model can be found in Ref 5.

The fitted and acquired Z-spectra were used as Z_{ref} and Z_{lab} , respectively, for calculation of the AREX spectra defined in Equation 3. Final AREX spectra were selected from regions with homogenous B_1 and apparent values equal to the nominal B_1 .

3 | RESULTS

To assess the spectral range of CEST signals at 3 T, a protein model solution was analyzed at multiple B_0 over a broad

range of frequency offsets (Figure 1A). At 14.1 T, several individual CEST signals were observed, whereas at 3 T distinct peaks were not resolved in the Z-spectrum. Separation of the CEST signals from the DS by the AREX evaluation revealed a substantial signal broadening with decreasing B_0 . The observed spectral range of CEST signals was approximately ± 7 ppm, ± 10 ppm, and ± 15 ppm at $B_0 = 14.1$ T, 7 T and 3 T, respectively. The steady increase of the spectral range of CEST signals, as well as of the fitted DS (Figure 1A, dashed lines), verified the correct separation of CEST signals at 3 T. In addition, the observed continuous increase of the CEST signal amplitudes in the AREX spectra with decreasing B_0 is in line with previous reports,^{5,30,47} which has been attributed to the saturation of an increasing number of spectrally neighboring proton species. To further validate the observed signal broadening with decreasing B_0 , in addition, a cross-linked protein model solution was analyzed (Figure 1B). The resulting ssMT provides a means to investigate signals far off-resonance from the DS, and thus independent of the applied fitting procedure. Likewise, a substantial broadening of the spectral range of the ssMT was found. The observed spectral range was approximately ± 50 ppm, ± 100 ppm, and ± 200 ppm at $B_0 = 14.1$ T, 7 T and 3 T, respectively. In comparison to untreated BSA, the percentage broadening of the

ssMT was in the approximate range, as was the case for the CEST signals (Figure 1A, B, colored arrows).

Before the acquisition of the in vivo CEST data, the bandwidth and GRAPPA acceleration factor of the 3D-image readout was optimized to maximize SNR, while minimizing t_{acq} (Figure 2). The flip angle of the image readout was adjusted according to the Ernst angle,⁴¹ depending on the resulting TR at different bandwidths and GRAPPA acceleration factors. For calculation of the SNR maps, presaturated images $M_{sat}(-3.5$ ppm) were used to optimize the image-readout parameters for the acquisition of actual CEST data. The optimum was achieved for bandwidth = 340 Hz/px and a GRAPPA acceleration factor of 2, leading to a t_{acq} of 3.6 seconds. Note that the two outer slices on each side could not be evaluated meaningfully due to aliasing artifacts in the slice direction (data not shown), resulting in an effective number of 12 slices.

The optimized 3D-image readout was used to investigate in detail the CEST signals observable at 3 T in the human brain. Acquisition of densely sampled Z-spectra over a broad range of frequency offsets and at multiple B_1 revealed a spectral range for the ssMT of approximately ± 200 ppm (Figure 3A, B), in line with findings for the in vitro measurements at 3 T (Figure 1B). In addition, distinct

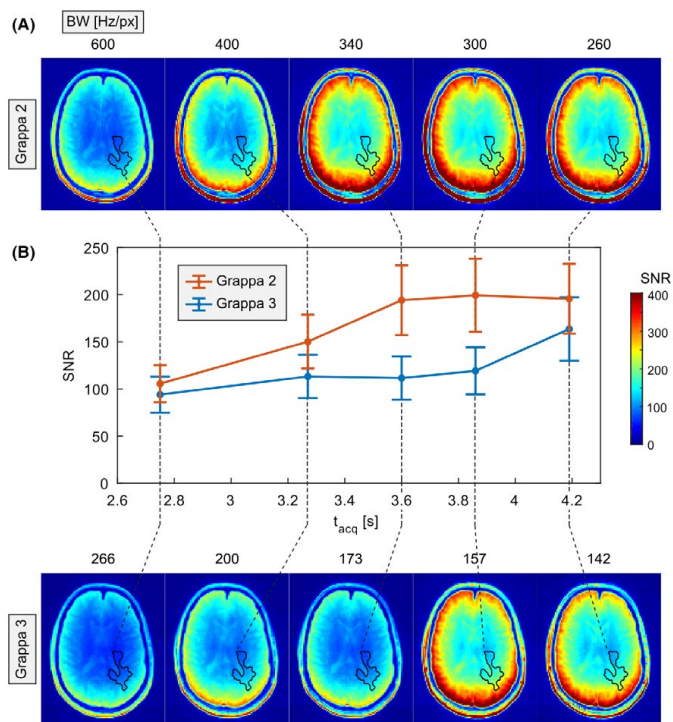


FIGURE 2 SNR maps (slice 8 of 16) for various bandwidths (BW) and GRAPPA acceleration factors at 3 T. Maximum SNR, while minimizing the t_{acq} , was obtained for bandwidth of 340 Hz/px and a GRAPPA acceleration factor of 2, yielding $t_{acq} = 3.6$ seconds. Regions of interest in white matter (A) were used to calculate the SNR illustrated in (B)

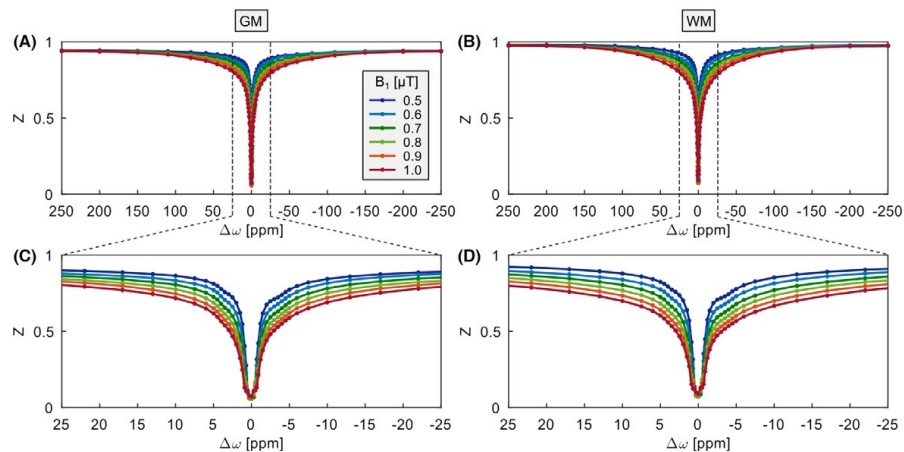


FIGURE 3 Z-spectra for gray matter (GM) (A,C) and white matter (WM) (B,D) of a healthy volunteer for multiple B_1 at 3 T. Besides the dominant signal of the DS and the ssMT (A,B), distinct peaks were not resolved and only slight dips of the amide proton transfer (APT) and relayed nuclear Overhauser effect (rNOE) signals could be observed at approximately +3.5 ppm and -3.5 ppm, respectively (C,D)

peaks for the APT and rNOE signals were also not resolved in living tissue (Figure 3C, D). Even though slight dips were observable for B_1 less than 0.7 μT at around +3.5 ppm and -3.5 ppm, these do not constitute the complete CEST signals, as was demonstrated in vitro (Figure 1A). The Z-values close to 1 at far off-resonance frequency offsets (Figure 3A, B, $\Delta\omega = \pm 250$ ppm) verify compliance with the steady-state criterion (Equation 2).

The prior knowledge about the actual spectral range of CEST signals at 3 T (i.e., approximately ± 15 ppm) was used to specify the fit parameters (i.e., start values and borders, Supporting Information Tables S1 and S2) of the 4-pool Lorentzian fit in vivo (Figure 4). In addition, the spectral positions of the Lorentzian functions were fixed to +3.5 ppm, -3.5 ppm, and -2.5 ppm for the APT, rNOE and ssMT, respectively. The resulting spectral range of the fitted APT and rNOE signals was in line with the range obtained in the measurement of the protein model solution (Figures 1A and 4A, orange arrows). Reliability and stability of the fit was verified by the evenly distributed values in the histograms of the resulting fit parameters without being restricted by the fit borders (Figure 4B). Furthermore, in compliance with expectations for all fitted pools, an increase in the average FWHM as a function of B_1 was observed.

Final CEST contrasts of a healthy volunteer at 3 T were in line with previous results at 7 T,²⁹ showing a hyperintense APT signal for the LD and MTR_{Relax} -metric in gray matter (Figure 5D, E) and a hyperintense rNOE signal in white matter (Figure 5G, H). The AREX maps of the APT and rNOE signals were similar, but interestingly showed substantial differences in the gray matter of the putamen (Figure 5F, I, pink arrows). In addition, all CEST contrasts were independent of

B_0 and B_1 inhomogeneities (Figure 5B, C), demonstrating the functionality of the applied field-correction methods.

To demonstrate the applicability of the acquisition protocol in a clinical setting, a patient with newly diagnosed glioblastoma was investigated (Figure 6). The relaxation-compensated MTR_{Relax} and AREX images of the APT and rNOE signals showed distinct changes in the tumor region, highlighting several different morphological features. For example, in the AREX-rNOE images, a consistent signal drop was observed within the tumor area, whereas the MTR_{Relax} -APT contrast showed increased signal intensity within the dorso-lateral tumor area (Figure 6, pink arrows). Acquisition of 3D data enabled an investigation of specific contrast features over several slices in the tumor region, and therefore a more reliable assignment of these features to morphological changes. However, for a conclusive assessment of the observed contrast changes to clinical questions, a sufficiently large cohort has to be investigated.

4 | DISCUSSION

In this study, the established acquisition protocol for relaxation-compensated CEST-MRI at 7 T has been translated to a clinically relevant magnetic field strength of 3 T. The implementation at 3 T is based on the central finding of a spectral range of CEST signals of approximately ± 15 ppm (Figure 1A). In contrast, CEST signals at this magnetic field strength are generally assumed to be present only in the range of about ± 6 ppm.^{18,38-40} The actual spectral range of CEST signals at 3 T is not readily assessable, as at low magnetic field strengths distinct peaks are no longer resolved in the

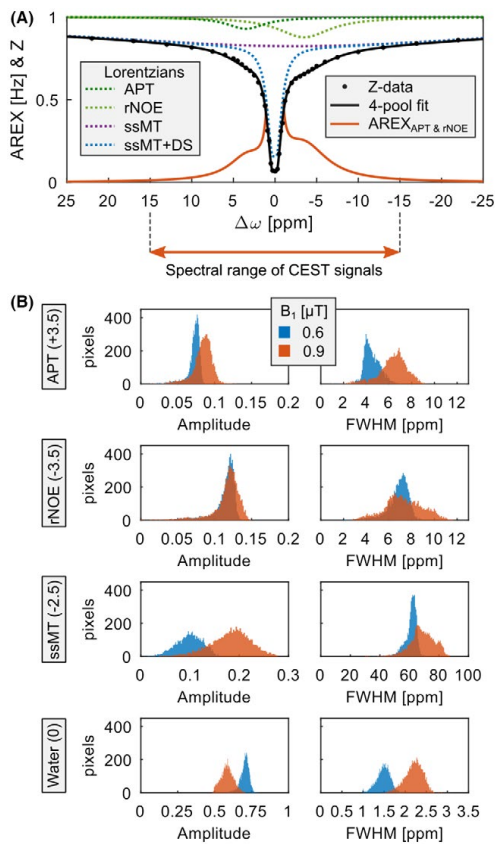


FIGURE 4 A, Z-spectra and AREX spectra ($B_1 = 0.6 \mu\text{T}$) of a representative voxel in white matter at 3 T. The spectral range of CEST signals (orange arrow) is the same as for protein model solutions (compare with Figure 1A). B, Histograms of the resulting parameters of a 4-pool Lorentzian-fit analysis in one slice of a healthy volunteer. The illustrated values at two different B_1 belong to the CEST images of the same subject and slice as in Figure 5

Z-spectrum. Nonetheless, investigation of gradual signal changes as a function of B_0 in this study (Figure 1) provides a means to more reliably distinguish between actual CEST signals and competing background effects (i.e., DS). The observed broadening of CEST signals with decreasing B_0 is in line with common observations in MR spectroscopy⁴⁷ and is based on the illustration of MR spectra as a function of the chemical shift in units of ppm, whereas the spectral width of MR signals is constant for units of Hz. CEST signals with a spectral range larger than ± 6 ppm were also recently observed by chemical exchange rotation transfer⁴⁸ and dualCEST⁵ experiments at 3 T, which also provide a means to effectively remove DS and ssMT effects. This prior knowledge about the spectral range of CEST signals enabled a reliable and

stable Lorentzian fitting also at 3 T without the need for more advanced approaches, such as multistep fitting procedures or special lineshapes for the ssMT.^{38-40,49} With respect to previous approaches,^{38-40,49} adjustment of the measurement protocols according to the observed findings in this study (i.e., increasing the sampling range of frequency offsets as well as the fitting range for the widths of the CEST signals) will not change the fundamental CEST contrasts. The advantage in applying these new conditions is the stabilization of the fit and the improvement of the contrast to noise ratio, as more of the actual CEST signals would be employed.

Due to the extensive broadening of CEST signals at 3 T, the number of pools for the established Lorentzian-fit model at 7 T was reduced from 5 to 4 pools. Consequently, the pool at +3.5 ppm represents the collective signal of all chemically exchanging protons resonating downfield from the water signal (i.e., amide, amine, guanidinium, and hydroxyl). However, due to the applied low-power saturation (i.e., $B_1 < 1 \mu\text{T}$) and the evaluation at +3.5 ppm, this pool can primarily be associated with the amide proton signal,³⁷ which is why it was termed APT. In addition, a compensation for underlying downfield-rNOE signals is possible by the dnsAPT metric.^{30,31} Following previous findings,^{5,23,29} the ssMT was set to be asymmetric around the DS and to resonate at approximately -2.5 ppm.

Application of relaxation-compensated CEST-MRI for quantitative analyses (i.e., using Equation 3 to measure the exchange-dependent relaxation rate: $AREX = R_{ex}^{50}$) is, in principle, also possible at 3 T. However, this requires, in addition to the steady-state criterion ($t_{sat} \gg T_1$, Equation 2), compliance with the large-shift limit ($\Delta\omega \gg \gamma B_1$).^{26,27} For the applied saturation powers in this study, in which B_1 is less than $1 \mu\text{T}$, the large-shift limit is fulfilled for frequency offsets $\Delta\omega > 1.45$ ppm (i.e., $\cos^2\theta = \frac{\Delta\omega^2}{\Delta\omega^2 + (\gamma B_1)^2} > 0.95$, where θ is the tilt angle of the effective field), and thus does not need to be considered for the evaluation of the APT and rNOE signal (Figure 4A, orange line). For evaluation of frequency offsets closer to the water signal or for application of higher B_1 amplitudes, the relaxation-compensated metrics in Equations 2 and 3 need to be extended to $MTR_{Relax} = \cos^2\theta \left(\frac{1}{Z_{lab}} - \frac{1}{Z_{ref}} \right)$.^{26,27,51} This allows relaxation-compensated CEST-MRI to also be applicable for high- B_1 approaches or imaging of CEST agents resonating close to the water signal.

With regard to application in a clinical setting, the presented acquisition protocol for relaxation-compensated CEST-MRI at 3 T is ready for use. Final CEST contrasts at 3 T were found to be in line with previous results at 7 T.²⁹ The overall acquisition duration is 20 minutes, including the two required CEST scans at different B_1 , as well as B_0 , B_1 , and T_1 mapping for correction of field inhomogeneities and relaxation compensation. Thus, the required time is approximately the same as for conventional ¹H-MRSI, which has already

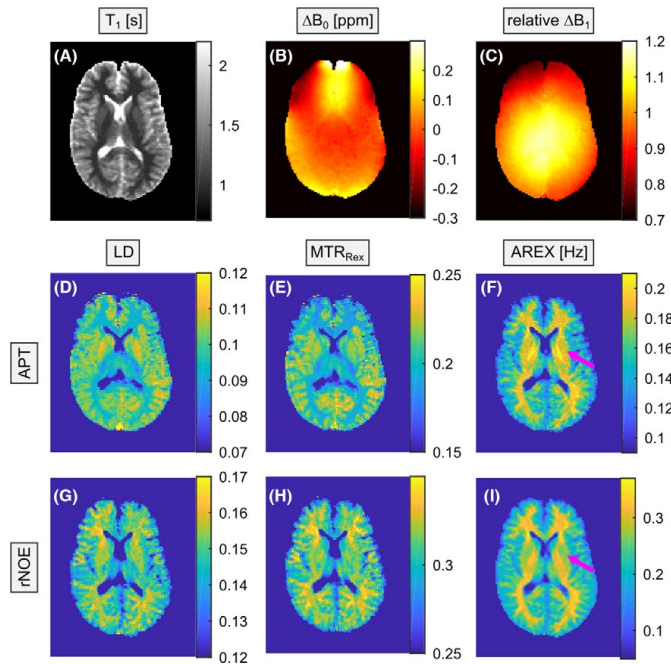


FIGURE 5 CEST image data of a healthy volunteer at 3 T ($B_1 = 0.7 \mu\text{T}$, slice 6 of 16). A-C, T_1 maps and field maps required for correction of the CEST images. Final APT (D-F) and rNOE (G-I) contrasts for all three metrics of Lorentzian difference (D,G), inverse magnetization transfer ratio (MTR_{Rex}) (E,H), and AREX (F,I) are in line with previous results at 7 T. The pink arrows indicate the putamen brain region. The CEST images were calculated from the fit parameters illustrated in Figure 4

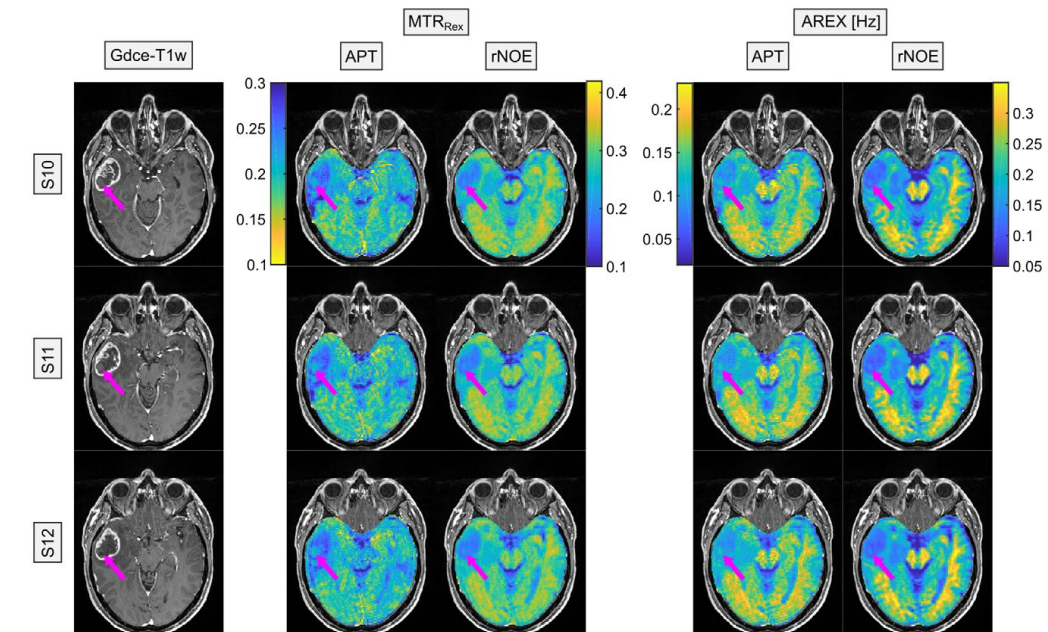


FIGURE 6 Relaxation-compensated CEST-MRI ($B_1 = 0.7 \mu\text{T}$, slices 10-12 of 16) of a patient with newly diagnosed glioblastoma (WHO grade IV) examined at 3 T. The tumor volume can be seen in the co-registered gadolinium contrast-enhanced T_1 -weighted (Gdce- T_1w) images. The pink arrows indicate a hyperintense region, which most likely corresponds to a blood clot within the tumor

been demonstrated to be applicable in a clinical routine. To further improve the current acquisition protocol, a real-time frequency drift correction as recently proposed for the MTR_{asym} analysis⁵²⁻⁵⁴ could be included, although it was not required in this work because the small changes in B_0 at 3 T of about 0.02 ppm⁵⁵ during a 20-minute examination are compensated for by the Lorentzian fitting. For the next step, this acquisition protocol will be used to comprehensively assess the actual clinical relevance of relaxation compensation in CEST-MRI for various neuro-oncological clinical questions. In particular, the translation to 3 T enables investigation of the controversially discussed overcompensation of T_1 at this magnetic field strength using the AREX approach (Equation 3).⁵⁶⁻⁵⁸ The unravelling of the different CEST signals and compensation for competing relaxation effects by the presented acquisition protocol can also enable obtaining more detailed information on the origin of CEST contrast in vivo. For general recommendations regarding acquisition parameters for CEST-MRI at 3 T, we refer to the APT-weighted approach of Zhou and van Zijl et al,⁵⁹⁻⁶¹ as they have collected a sizeable amount of clinical evidence up until now. Note that the saturation power of 0.7 μT used in this study generates a different CEST contrast and cannot be directly compared with APT-weighted MRI using 2 μT .

5 | CONCLUSIONS

The established acquisition protocol for relaxation-compensated CEST-MRI at ultrahigh magnetic field strengths was successfully translated to a clinically relevant magnetic field strength of 3 T. Reliable and stable Lorentzian fitting of the APT and rNOE signals at 3 T, where distinct peaks are not resolved in the Z-spectrum, was enabled by obtaining prior knowledge about the spectral range of CEST signals at multiple magnetic field strengths. In addition, the image readout was extended to three dimensions, allowing adequate coverage of the tumor volume. The overall acquisition duration, including all required data for relaxation compensation, was 20 minutes, making the acquisition protocol applicable in a clinical setting. Examination of a patient with glioblastoma revealed similar CEST contrasts at 3 T as was obtained at ultrahigh magnetic field strengths. With this acquisition protocol at hand, the clinical relevance of relaxation compensation in CEST-MRI can now be assessed in larger patient cohorts.

ACKNOWLEDGMENT

We thank the medical-technical radiology assistants from the German Cancer Research Center for their help in conducting the patient examination.

ORCID

Steffen Goerke  <https://orcid.org/0000-0002-0684-2423>
 Anagha Deshmane  <https://orcid.org/0000-0003-0697-0895>
 Moritz Zaiss  <https://orcid.org/0000-0001-9780-3616>
 Johannes Breitling  <https://orcid.org/0000-0001-8003-5382>
 Daniel Paech  <https://orcid.org/0000-0001-5755-6833>

REFERENCES

- McMahon MT, Gilad AA, Bulte J, et al. *Chemical exchange saturation transfer imaging: advances and applications*. 1st ed. Singapore: Pan Stanford Publishing Pte Ltd; 2017.
- van Zijl P, Yadav NN. Chemical exchange saturation transfer (CEST): What is in a name and what isn't? *Magn Reson Med*. 2011;65:927-948.
- Zhou J, Payen J-F, Wilson DA, Traystman RJ, van Zijl PCM. Using the amide proton signals of intracellular proteins and peptides to detect pH effects in MRI. *Nat Med*. 2003;9:1085-1090.
- Yan K, Fu Z, Yang C, et al. Assessing amide proton transfer (APT) MRI contrast origins in 9 L gliosarcoma in the rat brain using proteomic analysis. *Mol Imaging Biol*. 2015;17:479-487.
- Goerke S, Breitling J, Zaiss M, et al. Dual-frequency irradiation CEST-MRI of endogenous bulk mobile proteins. *NMR Biomed*. 2018;31:e3920.
- Chan K, McMahon MT, Kato Y, et al. Natural D-glucose as a biodegradable MRI contrast agent for detecting cancer. *Magn Reson Med*. 2012;68:1764-1773.
- Xu X, Yadav NN, Knutsson L, et al. Dynamic glucose-enhanced (DGE) MRI: translation to human scanning and first results in glioma patients. *Tomogr J Imaging Res*. 2015;1:105-114.
- Paech D, Schuenke P, Koehler C, et al. T1p-weighted dynamic glucose-enhanced MR imaging in the human brain. *Radiology*. 2017;285:914-922.
- Haris M, Nanga RPR, Singh A, et al. Exchange rates of creatine kinase metabolites: feasibility of imaging creatine by chemical exchange saturation transfer MRI. *NMR Biomed*. 2012;25:1305-1309.
- Haris M, Singh A, Cai K, et al. A technique for in vivo mapping of myocardial creatine kinase metabolism. *Nat Med*. 2014;20:209-214.
- Goerke S, Zaiss M, Bachert P. Characterization of creatine guanidinium proton exchange by water-exchange (WEX) spectroscopy for absolute-pH CEST imaging in vitro. *NMR Biomed*. 2014;27:507-518.
- Chen L, Barker PB, Weiss RG, van Zijl PCM, Xu J. Creatine and phosphocreatine mapping of mouse skeletal muscle by a polynomial and Lorentzian line-shape fitting CEST method. *Magn Reson Med*. 2019;81:69-78.
- Cai K, Haris M, Singh A, et al. Magnetic resonance imaging of glutamate. *Nat Med*. 2012;18:302-307.
- Haris M, Nath K, Cai K, et al. Imaging of glutamate neurotransmitter alterations in Alzheimer's disease. *NMR Biomed*. 2013;26:386-391.
- Roalf DR, Nanga RPR, Rupert PE, et al. Glutamate imaging (GluCEST) reveals lower brain GluCEST contrast in patients on the psychosis spectrum. *Mol Psychiatry*. 2017;22:1298-1305.

16. Jones CK, Schlosser MJ, van Zijl PCM, Pomper MG, Golay X, Zhou J. Amide proton transfer imaging of human brain tumors at 3T. *Magn Reson Med*. 2006;56:585–592.
17. Wen Z, Hu S, Huang F, et al. MR imaging of high-grade brain tumors using endogenous protein and peptide-based contrast. *NeuroImage*. 2010;51:616–622.
18. Togao O, Yoshiura T, Keupp J, et al. Amide proton transfer imaging of adult diffuse gliomas: correlation with histopathological grades. *Neuro-Oncol*. 2014;16:441–448.
19. Takayama Y, Nishie A, Togao O, et al. Amide proton transfer MR imaging of endometrial adenocarcinoma: association with histologic grade. *Radiology*. 2017;286:909–917.
20. Zhou J, Tryggestad E, Wen Z, et al. Differentiation between glioma and radiation necrosis using molecular magnetic resonance imaging of endogenous proteins and peptides. *Nat Med*. 2011;17:130–134.
21. Mehrabian H, Desmond KL, Soliman H, Sahgal A, Stanisz GJ. Differentiation between radiation necrosis and tumor progression using chemical exchange saturation transfer. *Clin Cancer Res*. 2017;23:3667–3675.
22. van Zijl PCM, Zhou J, Mori N, Payen J-F, Wilson D, Mori S. Mechanism of magnetization transfer during on-resonance water saturation. A new approach to detect mobile proteins, peptides, and lipids. *Magn Reson Med*. 2003;49:440–449.
23. Jones CK, Huang A, Xu J, et al. Nuclear Overhauser enhancement (NOE) imaging in the human brain at 7 T. *NeuroImage*. 2013;77:114–124.
24. Desmond KL, Stanisz GJ. Understanding quantitative pulsed CEST in the presence of MT. *Magn Reson Med*. 2012;67:979–990.
25. Zaiss M, Bachert P. Exchange-dependent relaxation in the rotating frame for slow and intermediate exchange—modeling off-resonant spin-lock and chemical exchange saturation transfer. *NMR Biomed*. 2013;26:507–518.
26. Zaiss M, Bachert P. Chemical exchange saturation transfer (CEST) and MR Z-spectroscopy in vivo: a review of theoretical approaches and methods. *Phys Med Biol*. 2013;58:R221–R269.
27. Zaiss M, Xu J, Goerke S, et al. Inverse Z-spectrum analysis for spillover-, MT-, and T1-corrected steady-state pulsed CEST-MRI—application to pH-weighted MRI of acute stroke. *NMR Biomed*. 2014;27:240–252.
28. Zaiß M, Schmitt B, Bachert P. Quantitative separation of CEST effect from magnetization transfer and spillover effects by Lorentzian-line-fit analysis of z-spectra. *J Magn Reson*. 2011;211:149–155.
29. Zaiss M, Windschuh J, Paech D, et al. Relaxation-compensated CEST-MRI of the human brain at 7 T: unbiased insight into NOE and amide signal changes in human glioblastoma. *NeuroImage*. 2015;112:180–188.
30. Zaiss M, Windschuh J, Goerke S, et al. Downfield-NOE-suppressed amide-CEST-MRI at 7 Tesla provides a unique contrast in human glioblastoma. *Magn Reson Med*. 2017;77:196–208.
31. Paech D, Windschuh J, Oberhollenzer J, et al. Assessing the predictability of IDH mutation and MGMT methylation status in glioma patients using relaxation-compensated multipool CEST MRI at 7.0 T. *Neuro-Oncol*. 2018;20:1661–1671.
32. Meissner J-E, Korzowski A, Regnery S, et al. Early response assessment of glioma patients to definitive chemoradiotherapy using chemical exchange saturation transfer imaging at 7 T. *J Magn Reson Imaging*. 2019. doi:https://doi.org/10.1002/jmri.26702
33. Regnery S, Adeberg S, Dreher C, et al. Chemical exchange saturation transfer MRI serves as predictor of early progression in glioblastoma patients. *Oncotarget*. 2018;9:28772–28783.
34. Jiang S, Zou T, Eberhart CG, et al. Predicting IDH mutation status in grade II gliomas using amide proton transfer-weighted (APT_w) MRI. *Magn Reson Med*. 2017;78:1100–1109.
35. Jiang S, Rui Q, Wang Yu, et al. Discriminating MGMT promoter methylation status in patients with glioblastoma employing amide proton transfer-weighted MRI metrics. *Eur Radiol*. 2018;28:2115–2123.
36. Desmond KL, Mehrabian H, Chavez S, et al. Chemical exchange saturation transfer for Predicting response to stereotactic radiosurgery in human brain metastasis. *Magn Reson Med*. 2016;78:1110–1120.
37. Mehrabian H, Myrehaug S, Soliman H, Sahgal A, Stanisz GJ. Evaluation of glioblastoma Response to therapy with chemical exchange saturation transfer. *Int J Radiat Oncol*. 2018;101:713–723.
38. Heo H-Y, Zhang Y, Jiang S, et al. Quantitative assessment of amide proton transfer (APT) and nuclear overhauser enhancement (NOE) imaging with extrapolated semisolid magnetization transfer reference (EMR) signals. II: Comparison of three EMR models and application to human brain glioma at 3 Tesla. *Magn Reson Med*. 2016;75:1630–1639.
39. Deshmane A, Zaiss M, Lindig T, et al. 3D gradient echo snapshot CEST MRI with low power saturation for human studies at 3T. *Magn Reson Med*. 2019;81:2412–2423.
40. Zhang J, Zhu W, Tain R, Zhou XJ, Cai K. Improved differentiation of low-grade and high-grade gliomas and detection of tumor proliferation using APT contrast fitted from Z-Spectrum. *Mol Imaging Biol*. 2018;20:623–631.
41. Zaiss M, Ehse P, Scheffler K. Snapshot-CEST: optimizing spiral-centric-reordered gradient echo acquisition for fast and robust 3D. *NMR Biomed*. 2018;31:e3879.
42. Schuenke P, Windschuh J, Roeloffs V, et al. Simultaneous mapping of water shift and B1 (WASABI)—application to field-inhomogeneity correction of CEST MRI data. *Magn Reson Med*. 2017;77:571–580.
43. Nolden M, Zelzer S, Seitel A, et al. The Medical Imaging Interaction Toolkit: challenges and advances. *Int J Comput Assist Radiol Surg*. 2013;8:607–620.
44. Windschuh J, Zaiss M, Meissner J-E, et al. Correction of B1-inhomogeneities for relaxation-compensated CEST imaging at 7 T. *NMR Biomed*. 2015;28:529–537.
45. Goerke S, Zaiss M, Kunz P, et al. Signature of protein unfolding in chemical exchange saturation transfer imaging. *NMR Biomed*. 2015;28:906–913.
46. Goerke S, Milde KS, Bukowiecki R, et al. Aggregation-induced changes in the chemical exchange saturation transfer (CEST) signals of proteins. *NMR Biomed*. 2017;30:e3665.
47. van Zijl PCM, Lam WW, Xu J, Knutsson L, Stanisz GJ. Magnetization transfer contrast and chemical exchange saturation transfer MRI. Features and analysis of the field-dependent saturation spectrum. *NeuroImage*. 2017;168:222–241.
48. Lin EC, Li H, Zu Z, et al. Chemical exchange rotation transfer (CERT) on human brain at 3 Tesla. *Magn Reson Med*. 2018;80:2609–2617.
49. Mehrabian H, Lam WW, Myrehaug S, Sahgal A, Stanisz GJ. Glioblastoma (GBM) effects on quantitative MRI of contralateral normal appearing white matter. *J Neurooncol*. 2018;139:97–106.
50. Meissner J-E, Goerke S, Rerich E, et al. Quantitative pulsed CEST-MRI using Ω -plots. *NMR Biomed*. 2015;28:1196–1208.
51. Zhang X-Y, Wang F, Xu J, et al. Increased CEST specificity for amide and fast-exchanging amine protons using exchange-dependent relaxation rate. *NMR Biomed*. 2018;31:e3863.

52. Windschuh J, Zaiss M, Ehses P, Lee J-S, Jerschow A, Regatte RR. Assessment of frequency drift on CEST MRI and dynamic correction: application to gagCEST at 7 T. *Magn Reson Med*. 2019;81:573–582.
53. Simegn GL, Van der Kouwe AJW, Robertson FC, Meintjes EM, Alhamud A. Real-time simultaneous shim and motion measurement and correction in glycoCEST MRI using double volumetric navigators (DvNavs). *Magn Reson Med*. 2019;81:2600–2613.
54. Liu R, Zhang H, Niu W, et al. Improved chemical exchange saturation transfer imaging with real-time frequency drift correction. *Magn Reson Med*. 2019;81:2915–2923.
55. Zaiss M, Herz K, Deshmane A, et al. Possible artifacts in dynamic CEST MRI due to motion and field alterations. *J Magn Reson*. 2019;298:16–22.
56. Lee D-H, Heo H-Y, Zhang K, et al. Quantitative assessment of the effects of water proton concentration and water T1 changes on amide proton transfer (APT) and nuclear overhauser enhancement (NOE) MRI: the origin of the APT imaging signal in brain tumor. *Magn Reson Med*. 2017;77:855–863.
57. Khlebnikov V, Polders D, Hendrikse J, et al. Amide proton transfer (APT) imaging of brain tumors at 7 T: the role of tissue water T1-relaxation properties. *Magn Reson Med*. 2017;77:1525–1532.
58. Zu Z. Towards the complex dependence of MTRasym on T1w in amide proton transfer (APT) imaging. *NMR Biomed*. 2018;31:e3934.
59. Zhou J, Blakeley JO, Hua J, et al. Practical data acquisition method for human brain tumor amide proton transfer (APT) imaging. *Magn Reson Med*. 2008;60:842–849.
60. Zhou J, Zhu He, Lim M, et al. Three-dimensional amide proton transfer MR imaging of gliomas: initial experience and comparison with gadolinium enhancement. *J Magn Reson Imaging*. 2013;38:1119–1128.
61. Joo B, Han K, Choi YS, et al. Amide proton transfer imaging for differentiation of benign and atypical meningiomas. *Eur Radiol*. 2018;28:331–339.

SUPPORTING INFORMATION

Additional supporting information may be found online in the Supporting Information section at the end of the article.

TABLE S1 Fit parameters of the 4-pool Lorentzian fit (part 1 of 2). The parameters are presented in the following order: lower border / start value / upper border

TABLE S2 Fit parameters of the 4-pool Lorentzian fit (part 2 of 2). The parameters are presented in the following order: lower border / start value / upper border

How to cite this article: Goerke S, Soehngen Y, Deshmane A, et al. Relaxation-compensated APT and rNOE CEST-MRI of human brain tumors at 3 T. *Magn Reson Med*. 2019;82:622–632. <https://doi.org/10.1002/mrm.27751>

Publication III

Adaptive denoising for chemical exchange saturation transfer MR imaging

Authors: Johannes Breitling[†], Anagha Deshmane[†], Steffen Goerke, Andreas Korzowski, Kai Herz, Mark E. Ladd, Klaus Scheffler, Peter Bachert, and Moritz Zaiss

[†] both authors contributed equally to this work

Journal reference: NMR in Biomedicine. 2019;32:e4133.

DOI: 10.1002/nbm.4133

Author contributions: **JB** conceived the presented approach upon discussion with **MZ**, worked out the conceptual and practical details with consultation of **AK**, performed all simulations and evaluated and interpreted all data. **AD** conducted together with **MZ** and **KH** the volunteer measurements in Tuebingen and prepared the corresponding data. **SG** performed the in vivo measurements in Heidelberg. **JB** drafted and revised the manuscript with support from **AD** and critical review from all co-authors.

RESEARCH ARTICLE

Adaptive denoising for chemical exchange saturation transfer MR imaging

Johannes Breitling^{1,2,3}  | Anagha Deshmane⁴  | Steffen Goerke¹  |Andreas Korzowski¹ | Kai Herz^{4,5} | Mark E. Ladd^{1,3,6} | Klaus Scheffler^{4,7} | Peter Bachert^{1,3} | Moritz Zaiss⁴ ¹Division of Medical Physics in Radiology, German Cancer Research Center (DKFZ), Heidelberg, Germany²Max-Planck-Institute for Nuclear Physics, Heidelberg, Germany³Faculty of Physics and Astronomy, University of Heidelberg, Heidelberg, Germany⁴Department of High-field Magnetic Resonance, Max-Planck-Institute for Biological Cybernetics, Tuebingen, Germany⁵IMPRS for Cognitive and Systems Neuroscience, University of Tuebingen, Tuebingen, Germany⁶Faculty of Medicine, University of Heidelberg, Heidelberg, Germany⁷Department of Biomedical Magnetic Resonance, University of Tuebingen, Germany**Correspondence**Moritz Zaiss, Max-Planck-Institute for Biological Cybernetics, Max-Planck-Ring 11, 72076 Tuebingen, Germany.
Email: moritz.zaiss@tuebingen.mpg.de**Funding information**

Horizon 2020 Framework Programme, Grant/Award Number: 667510; German Research Foundation, Grant/Award Number: ZA 814/2-1

High image signal-to-noise ratio (SNR) is required to reliably detect the inherently small chemical exchange saturation transfer (CEST) effects in vivo. In this study, it was demonstrated that identifying spectral redundancies of CEST data by principal component analysis (PCA) in combination with an appropriate data-driven extraction of relevant information can be used for an effective and robust denoising of CEST spectra. The relationship between the number of relevant principal components and SNR was studied on fitted in vivo Z-spectra with artificially introduced noise. Three different data-driven criteria to automatically determine the optimal number of necessary components were investigated. In addition, these criteria facilitate straightforward assessment of data quality that could provide guidance for CEST MR protocols in terms of SNR. Insights were applied to achieve a robust denoising of highly sampled low power Z-spectra of the human brain at 3 and 7 T. The median criterion provided the best estimation for the optimal number of components consistently for all three investigated artificial noise levels. Application of the denoising technique to in vivo data revealed a considerable increase in image quality for the amide and rNOE contrast with a considerable SNR gain. At 7 T the denoising capability was quantified to be comparable or even superior to an averaging of six measurements. The proposed denoising algorithm enables an efficient and robust denoising of CEST data by combining PCA with appropriate data-driven truncation criteria. With this generally applicable technique at hand, small CEST effects can be reliably detected without the need for repeated measurements.

KEYWORDS

amide, CEST, denoising, MRI, principal component analysis, rNOE, singular value decomposition

Abbreviations used: $\Delta\omega$, frequency offset; B_0 , magnetic field strength; B_1 , presaturation amplitude; CEST, chemical exchange saturation transfer; DC, duty cycle; FA, flip angle; GM, gray matter; LD, Lorentzian difference; MAE, mean absolute error; M_0 , equilibrium water magnetization; M_{sat} , water magnetization after presaturation; MRI, magnetic resonance imaging; PC, principal component; PCA, principal component analysis; PSNR, peak signal-to-noise ratio; RF, radiofrequency; rNOE, relayed nuclear Overhauser effect; SNR, signal-to-noise ratio; t_p , pulse length; t_{sat} , saturation duration; WM, white matter; Z, Z-spectrum; Z_{ref} , reference Z-spectrum

1 | INTRODUCTION

Chemical exchange saturation transfer (CEST) allows for the indirect detection of diluted molecules through transfer of their saturation to the abundant water pool.¹⁻³ Many different diluted solutes have been reported to be detectable with CEST, including peptides and proteins,³⁻⁶ with dependency on protein conformation,⁷⁻⁹ creatine^{10,11} and glutamate,^{12,13} as well as injected solutes such as iopamidol,¹⁴⁻¹⁶ glucose¹⁷⁻²⁰ and glucose derivatives.^{21,22}

Several CEST applications involve the fitting of spectrally selective CEST effects related to proteins, including isolation of amide, amine and relayed nuclear Overhauser effects (rNOE), as well as smaller peaks potentially related to creatine and choline-containing phospholipids.^{10,11,23,24} Due to recent reports of spatial correlations between isolated amide CEST and gadolinium ring enhancement,^{5,6} changes in rNOE with correlation to histology,²⁵⁻²⁸ and the ability of these contrasts to measure and predict brain tumor therapy response,²⁹⁻³² spatial correlations of spectrally selective protein CEST effects are also garnering increased clinical interest. Furthermore, novel experiments that target CEST signals specifically originating from bulk mobile proteins³³ are being investigated to identify altered states of proteins under conditions of disease.

As CEST effects are inherently small in magnitude, much effort is typically made to optimize saturation parameters for spectral selectivity and CEST effect size, in addition to optimizing imaging readouts. Experiments are often performed at ultra-high field strengths to take advantage of the inherent high signal-to-noise ratio (SNR). Still, both at clinical field strengths³⁴ and at ultra-high field,^{4,23} these spectrally selective CEST effects are small and difficult to detect reliably. This is true not only for multi-Lorentzian fitting approaches,^{5,35} which can have dozens of free parameters and depend on initial and boundary conditions, but also for simpler approaches like the three-point method,³⁶ where noise in the baseline points can lead to noise in the contrast. When saturation and imaging parameters are already optimized, further gains in SNR are usually achieved by averaging. However, this approach increases scan time and frequently comes at the cost of reduced resolution or volume coverage, neither of which is ideal for clinical applications. An alternative approach is iterative downsampling in the image domain to gradually improve estimates of fitting parameters,³⁷ but this method increases postprocessing times and can introduce aliasing artifacts into reconstructed images.

In addition to being more SNR-efficient than conventional 2D imaging, volumetric acquisitions such as the snapshot CEST approach³⁸ also generate tens of thousands of Z-spectra in a single experiment, opening up the possibility of statistical denoising. A common method to exploit data redundancy for denoising is to use a low-rank approximation of structured signals, of which the main features can be identified using singular value decomposition³⁹ or principal component analysis (PCA).⁴⁰ Low-rank approximations of Z-spectra have been used to improve SNR in hyper-CEST images,⁴¹ as well as for iterative motion correction of creatine CEST spectra in skeletal muscle.⁴² However, in both applications, few spectral peaks are present compared with the feature-rich *in vivo* Z-spectra acquired in CEST experiments with low saturation powers.

The aim of the present work is to improve the effective SNR of spectrally selective Z-spectra acquired in low-power CEST experiments. In this study, the use of PCA and low-rank approximations are investigated for denoising of fitted *in vivo* Z-spectra with artificially introduced noise (termed synthesized data from here on), and *in vivo* experiments at 3 and 7 T. In particular, we examine the relationship between the number of relevant principal components (PCs) and SNR, and investigate three possible criteria for determining the number of PCs to retain *in vivo*.

2 | METHODS

2.1 | PCA

PCA is a technique to reduce the dimensionality of data, while retaining the essence of its contained information. By identifying and exploiting the linear correlations in the observations of a dataset, it extracts a new set of uncorrelated variables called PCs and ranks them according to the proportion of data variability for which they account for.⁴⁰ The variance (ie information content of a signal) will concentrate in the first few PCs, whereas the noise is spread evenly over the dataset.⁴³ Therefore, preserving only the first few PCs can remove noise from the dataset.

The PCA denoising approach proposed for CEST imaging data is summarized in Figure 1. For a CEST experiment, each saturation frequency offset functions as a variable with the corresponding Z-value of each voxel being a different observation. The single CEST image $Z(\Delta\omega_i)$ of spatial dimensions $u \times v \times y$, can be rearranged into a vector $\mathbf{z}(\Delta\omega_i)$ of length $m \leq u \cdot v \cdot y$. Here, m is the number of actually considered voxels, which can be smaller than the total number of voxels due to the exclusion of regions outside the brain or dominated by fat. The full dataset consisting of n images for the saturation frequency offsets $\{\Delta\omega_1, \dots, \Delta\omega_n\}$ is then reshaped into a Casorati matrix \mathbf{C} of size $m \times n$ (Figure 1, step 1).

$$\mathbf{C} = (\mathbf{z}(\Delta\omega_1) \mathbf{z}(\Delta\omega_2) \dots \mathbf{z}(\Delta\omega_n)) = \begin{pmatrix} z_1(\Delta\omega_1) & z_1(\Delta\omega_2) & \dots & z_1(\Delta\omega_n) \\ z_2(\Delta\omega_1) & z_2(\Delta\omega_2) & \dots & z_2(\Delta\omega_n) \\ \vdots & \vdots & \ddots & \vdots \\ z_m(\Delta\omega_1) & z_m(\Delta\omega_2) & \dots & z_m(\Delta\omega_n) \end{pmatrix} \quad (1)$$

where each column represents a complete segmented image for one saturation frequency offset and each row represents the Z-spectrum of one

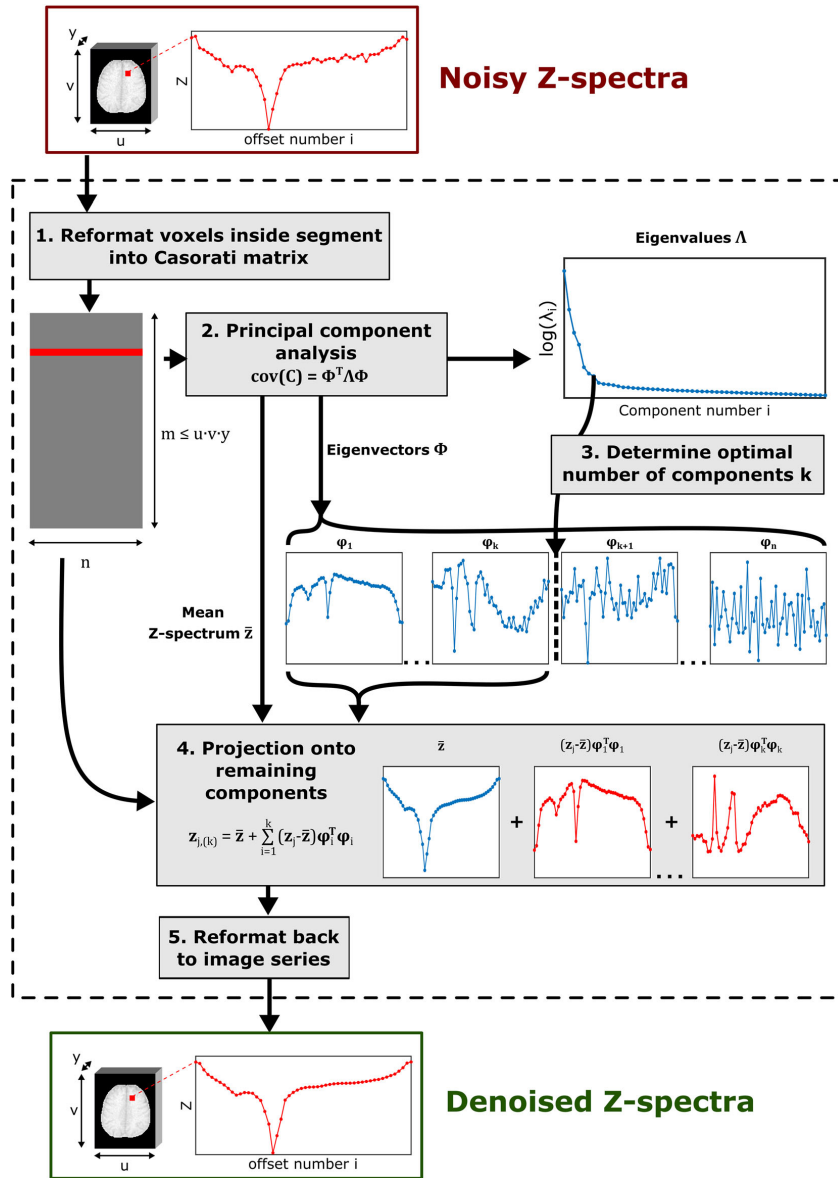


FIGURE 1 Illustration of the proposed denoising algorithm (the Z-spectrum of an exemplary voxel is shown in red). Step 1: The normalized and for B_0 -inhomogeneities corrected CEST data is reformatted into a Casorati matrix with voxels outside the segmentation being omitted. Step 2: PCA using the covariance matrix yields the mean Z-spectrum, the eigenvectors as well as the associated eigenvalues (blue). Step 3: Data-driven approaches based on the magnitude and slope changes of the eigenvalues approximate the optimal number of components to preserve. Step 4: Projection onto these first eigenvectors results in the denoised Z-spectra (step 5), which are reformatted back to an image series in the end

voxel. PCA is performed by eigendecomposition of the covariance matrix (Figure 1, step 2).

$$\text{cov}(\mathbf{C}) = \frac{1}{n-1} \tilde{\mathbf{C}}^T \tilde{\mathbf{C}} = \Phi^T \Lambda \Phi \quad (2)$$

with $\Phi = (\varphi_1, \varphi_2, \dots, \varphi_n)$ being the $n \times n$ orthonormal eigenvector matrix and $\Lambda = \text{diag}(\lambda_1, \lambda_2, \dots, \lambda_n)$ being the associated diagonal eigenvalue matrix with $\lambda_1 \geq \lambda_2 \geq \dots \geq \lambda_n$. For calculation of the covariance matrix, the column-wise mean-centered Casorati matrix $\tilde{C} = (\tilde{z}(\Delta\omega_1) \tilde{z}(\Delta\omega_2) \dots \tilde{z}(\Delta\omega_n))$ is used, where the corresponding rows are obtained by subtraction of the mean Z-spectrum $\bar{z}(\Delta\omega_i) = \frac{1}{m} \sum_{j=1}^m z_j(\Delta\omega_i)$.

To remove the contributions which are associated only with noise, \tilde{C} is projected onto a reduced set of the k highest ranked PCs $\Phi_{(k)} = (\varphi_1, \varphi_2, \dots, \varphi_k)$ with $1 \leq k \leq n$ (Figure 1, step 4):

$$\tilde{C}_{(k)} = \tilde{C} \Phi_{(k)} \Phi_{(k)}^T \quad (3)$$

The denoised Casorati matrix is obtained by addition of the mean Z-spectrum: $z_{f,(k)}(\Delta\omega_i) = \tilde{z}_{f,(k)}(\Delta\omega_i) + \bar{z}(\Delta\omega_i)$. Finally, the denoised Casorati matrix is reformatted into a denoised image series of dimensions $u \times v \times y \times n$ (Figure 1, step 5).

The outcome of the algorithm mainly depends on one parameter: the number of preserved components k (Figure 1, step 3). If too few components are preserved, actual information will be lost, leading to missing or deformed resonances, whereas too many components would diminish the denoising effect. A close to optimal value of k is therefore essential for the performance of the denoising. The number of components can be based upon prior knowledge about the composition of the examined object if available, as was demonstrated in the case of a hyper-CEST agent.⁴¹ For in vivo applications focusing on endogenous contrast and multiple spectral features, the choice of k must be carefully tuned.

Therefore, in this study, we apply PCA in conjunction with data-driven approaches to objectively determine the optimal k for any noise level and without prior knowledge about the spectral composition. The associated eigenvalues of the PCA can be interpreted for each component as the variability of the signal as well as of the noise, with the first components being mainly related to the signal and the later components only to noise. Data-driven approaches based on the associated eigenvalues can be used to approximate the optimal k of respective datasets. In the following, three suitable methods are presented and thereafter investigated for their applicability to denoising of in vivo CEST MRI data. The three examined criteria were chosen based on their simplicity, straightforward applicability and robustness. However, they only represent a selective choice and there are numerous other approaches.⁴⁴⁻⁴⁶

2.1.1 | Malinowskis empirical indicator function

The first approach is based on a theory of error concerning abstract factor analysis.⁴⁷ Assuming knowledge of the correct number of components, the real error RE (ie the difference between the ground truth and the noisy unprocessed data) can be expressed as:

$$RE = \left[\frac{\sum_{j=k+1}^n \lambda_j}{m(n-k)} \right]^{1/2} \quad (4)$$

From RE an empirical indicator function can be derived, which was shown to reach a minimum when the – actually unknown – correct number of components is employed.⁴⁸

$$k_{ind} = \arg \min_k \frac{RE(k)}{(n-k)^2} \quad (5)$$

2.1.2 | Nelson criterion

The second approach is based on the shape of the course of the eigenvalues plotted as a diminishing series (Figure 1, step 3). A sharp change in the slope marks the transition from signal-related components to noise-related components.⁴⁹ The latter noise-related eigenvalues exhibit a characteristic linear fall-off, which enables identifying them with an iterative linear regression. To this end, the coefficient of determination r^2 can be expressed as:

$$r^2(k) = \left(\frac{(n-k) \sum_{i=k+1}^n \lambda_i - \sum I \sum \lambda_i}{\left((n-k) \sum^2 - (\sum I)^2 \right)^{1/2} \left((n-k) \sum \lambda^2 - (\sum \lambda_i)^2 \right)^{1/2}} \right)^2 \quad (6)$$

The largest subset of eigenvalues (ie smallest number of excluded leading eigenvalues) achieving $r^2 \geq 0.8$ was shown to indicate separation of signal- and noise-related components, and thereby the optimal number of components.⁵⁰

$$k_{reg} = \min \{k | r^2(k) \geq 0.8\} \quad (7)$$

2.1.3 | Median criterion

The third approach uses the median of the eigenvalues to estimate the noise level of the data and thereby determines a threshold for the signal-related eigenvalues.⁵¹ To increase robustness and minimize the impact of the signal itself, only a subset λ_t is used in the median estimation, with some of the first eigenvalues adaptively removed:

$$\lambda_t = \left\{ \lambda_j | \sqrt{\lambda_j} < 2 \cdot \text{median} \left(\sqrt{\lambda_1}, \sqrt{\lambda_2}, \dots, \sqrt{\lambda_n} \right) \right\} \quad (8)$$

The noise estimate is obtained after taking into account the previously stated empirical correction factor ($\beta = 1.29$)⁵¹ and is used as a threshold to determine the number of components:

$$k_{med} = \max \left\{ k | \lambda_k \geq \beta^2 \cdot \text{median}(\lambda_t) \right\} \quad (9)$$

2.2 | CEST MR imaging

2.2.1 | CEST MR imaging at 3 T

CEST MRI was performed on three different 3 T whole-body MR-scanners (MAGNETOM Prisma, Siemens Healthineers, Erlangen, Germany) with the vendor's head/neck coil (64 channels) on six healthy subjects (V1/V2, V3/V4 and V5/V6 on scanners 1, 2 and 3, respectively), with informed consent provided prior to the experiment and with the approval of the local ethics committee in accordance with the relevant guidelines and regulations.

The employed 3D snapshot CEST acquisition³⁸ consisted of a presaturation module followed by a single-shot radiofrequency (RF) and gradient spoiled gradient echo readout with centric spiral reordering. The image-readout parameters optimized for 3 T³⁴ were: GRAPPA acceleration factor 2, TE = 2 ms, TR = 4 ms, bandwidth = 700 Hz/pixel, elongation factor = 0.5 with a flip angle (FA) = 5°, field of view = 220 × 180 × 54 mm³, and matrix size of 128 × 104 × 18 yielding a 1.7 × 1.7 × 3 mm³ resolution for the measurement of V1; and a FA = 6°, field of view = 220 × 180 × 60 mm³, and matrix size of 128 × 104 × 12 yielding a 1.7 × 1.7 × 5 mm³ resolution for the measurements of V2 through to V6. The resulting readout times for one 3D-image were 2.9 and 2.0 seconds, respectively.

Presaturation was achieved by a train of 80 Gaussian-shaped RF pulses of mean amplitude $B_1 = FA/(\gamma \cdot t_p) = 0.6 \mu\text{T}$, pulse duration $t_p = 20$ ms and duty cycle (DC) = 50%, resulting in a total saturation time of $t_{sat} = 3.2$ seconds. Z-spectrum data were acquired after saturation at 55 offsets in the range between ±100 ppm and normalized by M_0 scans with 12 seconds of relaxation and saturation at -300 ppm. CEST measurements were acquired six times to enable generation of high SNR data by averaging. B_0 - and B_1 -mapping were obtained using the WASABI approach⁵² with the same image-readout parameters as for the CEST measurements. All image data were motion-corrected using the AFNI's 3Dvolreg function.⁵³

2.2.2 | CEST MR imaging at 7 T

CEST MRI was performed on a 7 T whole-body MR-scanner (MAGNETOM, Siemens Healthineers) with a 24 channel head coil on one healthy subject (ie V7), with informed consent provided prior to the experiment and with the approval of the local ethics committee of the Medical Faculty of the University of Heidelberg, and in accordance with the relevant guidelines and regulations.

The snapshot CEST acquisition used at 7 T differed from the 3 T settings of V1 in the following parameters: GRAPPA acceleration factor 3, bandwidth = 560 Hz/pixel, FA = 6° and elongation factor = 0.6. The resulting readout time for one 3D image was 2.0 seconds.

Optimized presaturation for 7 T consisted of a train of 140 Gaussian-shaped RF pulses with mean amplitude $B_1 = 0.6 \mu\text{T}$ or $0.9 \mu\text{T}$, pulse duration $t_p = 15$ ms and DC = 60%, resulting in a $t_{sat} = 3.5$ seconds. Z-spectrum data were acquired after saturation at 54 offsets in the range between ±100 ppm and normalized by M_0 scans with 12 seconds of relaxation and saturation at -300 ppm. Similar to the 3 T measurements, at 7 T, B_0 - and B_1 -mapping were obtained using the WASABI approach⁵² and CEST measurements were repeated six times to enable generation of high SNR data by averaging. All image data was coregistered using an intensity-based rigid registration algorithm in MITK.⁵⁴

2.3 | Data evaluation

For both 3 and 7 T data, M_0 images were manually masked to isolate brain tissues and CSF with the outermost slices excluded due to slice profile artifacts in the slab-selective readout. CEST images were generated from the Z-value $Z(\Delta\omega)$, given by the ratio of the saturated image $M_{sat}(\Delta\omega)$ and the unsaturated image M_0 : $Z(\Delta\omega) = M_{sat}(\Delta\omega)/M_0$. The resulting Z-spectra were shifted along the frequency offset dimension according to the acquired B_0 -map to correct for field shifts. After B_0 -correction, Z-spectra were either averaged or denoised using PCA with one of the three criteria listed above to determine the number of relevant PCs to retain. For the denoising the entire masked volume was used, comprising brain tissue and CSF with a total of between 40 000 and 70 000 voxels.

Z-spectra at 7 T were fitted voxel-wise by a five-pool Lorentzian fit model comprising contributions of direct water saturation (0 ppm), semisolid magnetization transfer (-2.0 ppm), as well as rNOE (-3.5 ppm), amide (3.5 ppm) and amine (2.0 ppm) resonances. A more detailed description of the fit model (ie start values and boundaries) can be found in the supporting information. By omitting the pool of interest a reference Z-spectrum Z_{ref} is obtained.⁵ For Z-spectra at 3 T, Z_{ref} is generated by a two-pool background fit model consisting of direct water saturation and semisolid magnetization transfer.³⁴ Peak specific CEST contrasts were calculated by the Lorentzian difference method⁴ according to $MTR_{LD} = Z_{ref} - Z$, where Z are the actual data points. Amide and rNOE contrast images were generated by evaluating the corresponding MTR_{LD} maps at 3.5 and -3.5 ppm, respectively. The 7 T CEST contrasts were corrected for B_1 -inhomogeneities by a two-point contrast correction⁵⁵ (reconstructed to $B_1 = 0.7 \mu\text{T}$).

2.4 | Simulations

2.4.1 | Generation of synthesized data

To demonstrate the performance of the denoising approach, artificial noise was introduced to fitted *in vivo* Z-spectra. This allowed investigation of the dependence on the number of components with a defined reference (ie ground truth).

The fitted Z-spectra of the averaged high SNR 7 T CEST data acquired with $B_1 = 0.6 \mu\text{T}$ without application of the denoising algorithm were used as a starting point for generating realistic simulation data. Image data were obtained by multiplication of the input Z-spectra with the M_0 used for normalization. To obtain a realistic noise distribution, a GRAPPA reconstruction was simulated with a similar set-up as for the *in vivo* imaging at 7 T (24 coils, acceleration factor 3, 32 ACS lines), with the image for each coil being corrupted in k-space with additive circular complex Gaussian noise with amplitude σ , normalized variance of 1 at each coil, and a correlation coefficient between coils of $\rho = 0.1$.⁵⁶ The final noisy Z-spectra were obtained after normalization with the noise-afflicted M_0 image. The ground truth for comparison was generated by performing the procedure without addition of noise. This process is illustrated in Figure S1.

2.4.2 | Quantification of the truncation

Different data-driven approaches were investigated to determine the required number of PCs to best describe the data. To determine the optimal number of components, the peak signal-to-noise ratio (PSNR) over all voxels j and offsets i was determined as an evaluation measure:

$$PSNR(k) = -10 \cdot \log_{10} \left(\frac{1}{m \cdot n} \sum_{i=1}^n \sum_{j=1}^m (z_i(\Delta\omega_j) - z_{i,ground\,truth}(\Delta\omega_j))^2 \right) \quad (10)$$

The PSNR is equivalent to the mean square error and was chosen due to its simplicity and its straightforward applicability to spectral data. To reliably assess the denoising performance for different SNR levels, 100 different realizations were generated at each noise level and evaluated.

3 | RESULTS

3.1 | Synthesized data

The effect of noise on the ability to detect Z-spectrum features, and the corresponding improvement with low-rank approximations, is illustrated using synthesized spectra in Figure 2. Upon introduction of artificial noise, the quality of exemplary single voxel grey matter (GM) and white matter (WM) Z-spectra of the synthesized data degrade significantly, preventing a clear identification of CEST peaks in the spectrum, especially for the low SNR case (Figure 2, bottom row). PCA of the noisy data and subsequent low-rank approximation by retaining a small number of components leads to smoother Z-spectra in all cases, allowing reliable identification of CEST resonances. Observing the residuals (dotted lines, enlarged by a factor of 10) and the mean absolute error (MAE) of WM and GM combined, shows that fluctuations decrease when using fewer and fewer components, but if too few components are used (Figure 2, sigma = 0.001, k = 7) then the Z-spectra cannot be fully described by the reduced basis and errors increase again. This shows that it is important to use enough components to not introduce new errors. Interestingly, the MAE

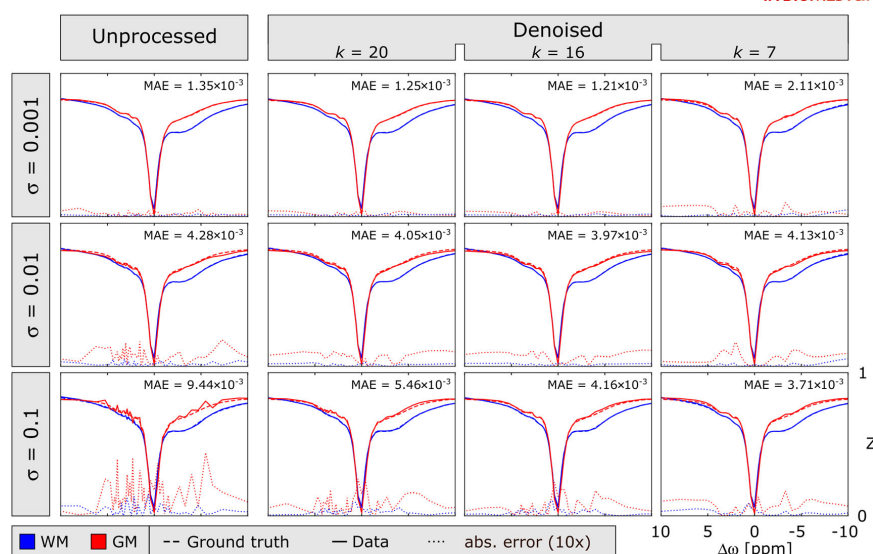


FIGURE 2 Effect of denoising in synthesized gray matter (GM, red) and white matter (WM, blue) Z-spectra of exemplary single voxels. As the noise level increases (from top to bottom rows), more PCs are corrupted by noise and fewer components give the best spectral approximation. However, using too few PCs can introduce small residual errors, which can be seen in the high SNR data (top right) as an increase of the combined mean absolute error (MAE) of WM and GM. Please note that the absolute error (dotted) between ground truth (dashed) and data (solid) is scaled by a factor of 10 for visualization purposes

does not increase much with more truncation in the case of higher noise levels (Figure 2, $\sigma = 0.01$, $k = 7$). This observation illustrates that the best truncation depends on the noise level. This effect can be studied by the PSNR value (Equation 10), which uses the simulated ground truth for comparison.

The PSNR value as a function of retained components k is shown in Figure 3, along with the mean truncation point suggested by the proposed application of the Malinowski criterion, Nelson criterion and median criterion. For all SNR levels there is one defined (global) optimum PSNR value and corresponding PC truncation point. The three data-driven approaches based on the associated eigenvalues yield a good approximation of the optimal number of components, as determined by the PSNR (Table 1). The Malinowski criterion tends to underestimate the necessary number of components (Table 2), especially for the medium SNR data (Figure 3, middle), but yields good results for lower SNR data. The median criterion consistently provided the number of components that resulted in the highest PSNR for all SNR levels. As SNR decreases, the optimum PC truncation point shifts as expected to fewer components; additional components are corrupted by noise and thereby would deteriorate the spectral approximation (Figure 3, top). Furthermore, for noisier data a larger gain in the PSNR between the optimal denoising and the initial data (data with all components) was observed (3.38 compared with 2.07 dB for the high SNR data; Table 1, first and last rows). This observation is in line with the associated smaller number of necessary components to describe the noisier spectra, which implies more PCs can be omitted with a consequential larger achievable denoising effect. Or, in other words, a higher initial noise level will enable the removal of more noise from the dataset.

Observing the square root of the eigenvalues λ_i (Figure 3, bottom), which are a measure of the influence of the individual PCs, enables obtaining additional interesting insights from the denoising. The value $\sqrt{\lambda_i}$ can be shown to be equal to the maximum possible change at a single frequency offset in the Z-spectrum upon the addition or omission of this i^{th} PC. For higher noise levels, the influence of the trailing, noise-corrupted PCs increases. Because we can determine the optimal truncation point with the criteria, this leads to an important finding: we can now evaluate if the noise level of our data is sufficiently small to describe an effect we are interested in. Because the optimal truncation point denotes the transition of signal related to noise-dominated PCs, $\sqrt{\lambda_{k+1}}$ (square root of the first eigenvalue after the truncation point) can be used as an estimate of the maximum possible noise-induced error at a single frequency offset, and thereby of the smallest detectable effect size. If the effect size of interest in the Z-spectrum S_E is larger than this value, we can in principle resolve it; if it is smaller, then the data is too noisy and potentially we cannot retrieve the information we are interested in. This value is, however, to be understood as an upper limit. For example, sampling the Z-spectrum very densely and taking nearby offsets into account in the analysis potentially enables detecting even smaller effects.

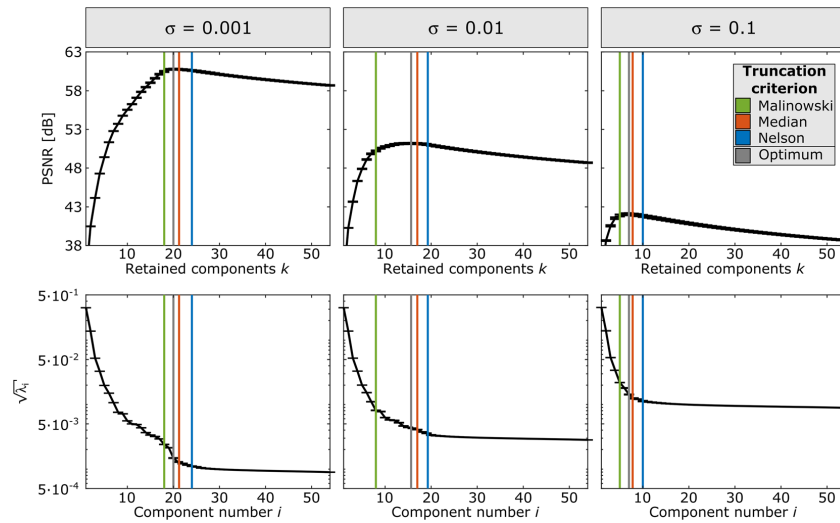


FIGURE 3 Determining the optimum PC truncation in synthesized Z-spectra (exemplary gray and white matter voxels shown in Figure 2). Top: Peak signal-to-noise ratio (PSNR) over all voxels and offsets compared with the ground truth. Results are shown as the mean for 100 different noise realizations with the error bars showing the corresponding standard deviation. An increase in noise (from left to right) results for the PSNR maximum in a shift to a smaller optimal number of components as well as a larger gain compared with the noisy input data (Table 2, first and bottom rows). Bottom: The transition point of the eigenvalues corresponds to the PSNR optimum (gray), and can be automatically determined by the three different data-driven criteria. The median stopping criterion (orange) suggests a close to optimal number of PCs resulting in the lowest residual error. The necessary number of components is underestimated by the Malinowski criterion (green) and overestimated by the Nelson criterion (blue)

TABLE 1 Peak signal-to-noise ratio corresponding to each proposed criterion for different noise levels. Results are obtained as the mean of 100 repetitions of the denoising algorithm each run with a different noise realization. The values in the brackets are the corresponding standard deviations of the obtained mean

Truncation criterion	PSNR [dB]		
	$\sigma = 0.001$	$\sigma = 0.01$	$\sigma = 0.1$
All components	58.70 (5)	48.69 (5)	38.68 (7)
Malinowski	60.49 (7)	50.21 (7)	41.89 (13)
Nelson	60.60 (7)	51.03 (11)	41.83 (16)
Median	60.74 (7)	51.17 (9)	42.01 (15)
Optimum	60.77 (7)	51.18 (9)	42.06 (14)

TABLE 2 Mean difference between the suggested number of retained components of each proposed criterion and the actual optimum. A negative value implies too few retained components, a positive one too many. Results are obtained as the mean of 100 repetitions of the denoising algorithm each run with a different noise realization. The values in the brackets are the corresponding standard deviations of the obtained mean

Truncation criterion	Mean difference between component number and optimal truncation		
	$\sigma = 0.001$	$\sigma = 0.01$	$\sigma = 0.1$
Malinowski	-2.0 (0)	-7.7 (5)	-2.0 (1)
Nelson	4.0 (4)	3.6 (7)	3.0 (4)
Median	1.2 (4)	1.4 (5)	0.8 (5)

3.2 | In vivo data

To enable the assessment of the performance of the denoising in vivo, high SNR data were obtained at 3 and 7 T by averaging six measurements. As these still do not constitute a real ground truth, only a qualitative assessment based on visual inspection is performed, as opposed to

quantitative measures. Figure 4 illustrates the effect of PCA denoising on MTR_{LD} images acquired at 7 T with an estimated⁵⁷ SNR ≈ 185 for the M_0 image. In this dataset, the median criterion suggested 16 components should be retained (Table 3). As observed in the synthesized data, retaining fewer components (in this case, six) yielded even smoother images than the averaged ones, but with reduced GM/WM contrast. This effect also becomes evident in the corresponding Bland-Altman plot (Figure S2). Both results illustrate one possible pitfall of uncontrolled and thereby potentially excessive PCA denoising, namely the distortion of contrast.

Similar results are obtained in MTR_{LD} images acquired from 3 T spectra, as illustrated in Figure 5. At clinical field strengths, CEST effects are spectrally broad and coalesced, making isolated spectrally selective effects particularly sensitive to noise. Denoising of the Z-spectra by retaining 14 components as determined by the median criterion results in an image quality comparable or even superior to those achieved by averaging the six measurements. As observed in the 7 T data, retaining only the small amount of PCs as suggested by the Malinowski criterion resulted in exceptionally smooth images, with a slightly reduced GM/WM contrast (Figure 5, right). It should be noted that in this case, distortions in the contrasts due to retaining too few components cannot be excluded with complete certainty. Application of the denoising algorithm using the median criterion to the data of five additional subjects measured at three different MR scanners at 3 T yielded a considerable image quality gain for the MTR_{LD} contrasts compared with the unprocessed data (Figure 6). The corresponding suggested number of components to retain is consistent across all subjects for all three criteria with an expectable small variability (Table 3).

4 | DISCUSSION

In this study, we propose a denoising algorithm for Z-spectral image data acquired from CEST experiments. PCA was applied to 3D datasets to identify spectral redundancies, and thereby separate noise-like characteristics from meaningful spectral features. In conjunction with an appropriate data-driven approach to determine the required number of components, we demonstrated that a PCA-based denoising algorithm can reduce noise and provide a better approximation of the actual Z-spectrum signal. Importantly, PCA and subsequent low-rank approximations of the Z-spectrum are fast computational operations that are simple to implement. The resulting SNR gain allows us to avoid the scan time trade-off of reducing the volume coverage for more signal averages.

PCA has already been shown to be a powerful denoising technique in HyperCEST by Döpfert et al.⁴¹ Note that in that work, as opposed to the approach presented here, each voxel was interpreted as a variable, with the saturation frequency offsets being the different observations. This entails a row-wise mean-centering of the Casorati matrix and transposed dimensions for calculating the covariance matrix and the resulting eigenvectors. It should be noted that this is not just a difference in formulation but in conception and yields slightly different results in the denoising. In the HyperCEST study, the optimal number of components was deduced from the two-phase composition of the investigated phantom. For conventional CEST experiments with multiple spectral resonances, the number of relevant components is not straightforward to determine, as the number of contributions, their dependencies on physiological parameters and pathological alterations thereof, are unknown. We showed that for in vivo ¹H CEST imaging, retaining too many components will diminish the denoising effect, while retaining too few components

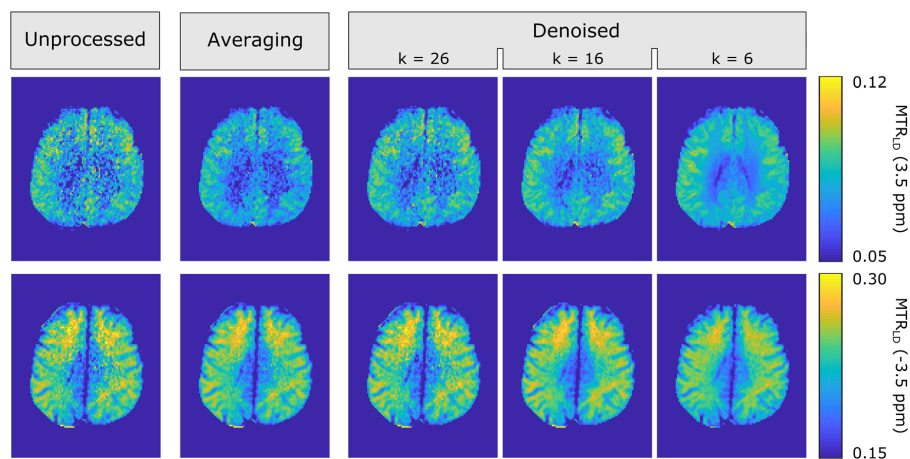
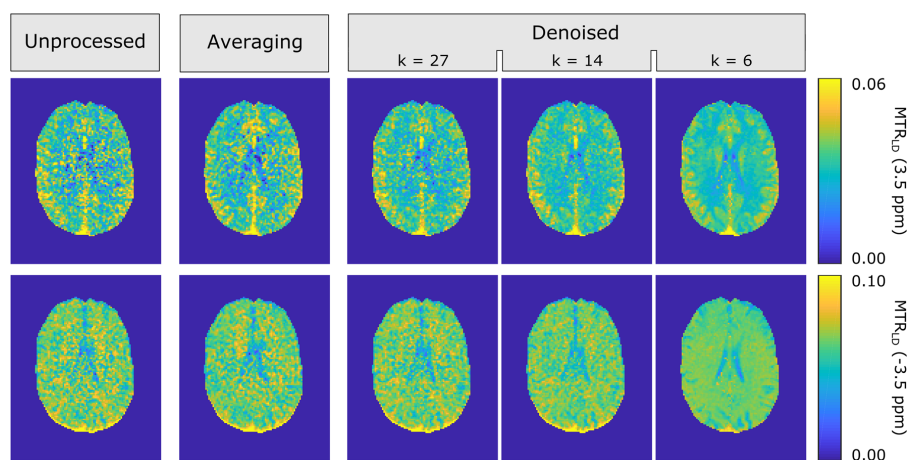


FIGURE 4 MTR_{LD} contrasts for amide (top) and rNOE (bottom) of a healthy volunteer (V7) acquired at 7 T. Application of the denoising algorithm to the single measurement (left) results in smoother images for a decreasing number of retained components (middle to right). Preservation of 16 PCs as determined by the median criterion yields an image quality (second from the right) comparable to averaging six measurements (second from the left). A stronger truncation results in even smoother contrast (right), which, however, indicates the introduction of artifacts.

TABLE 3 Suggested number of retained components of each proposed criterion for the in vivo measurements

Subject	B0 [T]	B1 [μ T]	Number of retained components k		
			Malinowski	Nelson	Median
V1	3	0.6	6	12	14
V2	3	0.6	9	15	19
V3	3	0.6	9	15	15
V4	3	0.6	10	14	17
V5	3	0.6	5	12	13
V6	3	0.6	9	16	17
V7	7	0.6	9	12	16
V7	7	0.9	9	13	16

**FIGURE 5** MTR_{LD} contrasts for amide (top) and rNOE (bottom) of a healthy volunteer (V1) acquired at 3 T, as for the 7 T data (Figure 4), application of the denoising algorithm to the single measurement (left) results in smoother images with the decreasing number of retained components (middle to right). Retaining 14 PCs as suggested by the median criterion yields an image quality (second from the right) superior to averaging six measurements (second from the left). A stronger truncation as suggested by the Malinowski criterion results in even smoother contrast (right); however, as a result the introduction of potential contrast distortions by retaining too few PCs cannot be completely excluded

will result in missing or deformed resonances. We want to emphasize caution, as these artifacts can be difficult to recognize: although excessive denoising leads to startlingly smooth images, these may no longer represent true spectral features.

Here, we investigated the optimal choice of retained components by means of synthesized data to allow for comparison with a ground truth. The synthesized data were modeled from high SNR in vivo CEST spectra acquired by low-power saturation. By using the fitted data of an actual in vivo CEST measurement, which was only corrected for motion and B_0 -inhomogeneities, the simulated signal still contained residual B_1 inhomogeneities as well as the spatially variant coil sensitivity profile. The noise distribution was realistically simulated by adding the noise in k -space and thereby takes into account the effects of the GRAPPA reconstruction, as is performed for the in vivo data. Consequences of this can also be seen in the resulting differing noise levels in the exemplary voxels of GM and WM (Figure 2, sigma = 0.1, unprocessed), which can be attributed to the spatially varying noise distribution as well as a scaling effect due to the normalization with the M_0 image, which exhibits different signal amplitudes for GM and WM. The synthesized signal assumes a five-pool Lorentzian model with no B_0 shifts. The resulting numerous combinations of width, amplitude and position of the Lorentzians should reflect the observable variety of Z-spectra in vivo. It has yet to be determined if the prior application of a correction for B_0 inhomogeneities affects the functioning of the PCA.

The data-driven truncation criteria examined in this study estimate the number of principle components which remain uncontaminated by noise. Simulations indicated that all three criteria give reliable denoising results for each investigated SNR level. Here, the Median criterion yields the best results for the synthesized data with a close to optimal truncation point, as reflected by PSNR, determined for all three noise levels. The Nelson criterion tends to overestimate the necessary number of components in the synthesized data, diminishing the desired denoising effect. By contrast, the

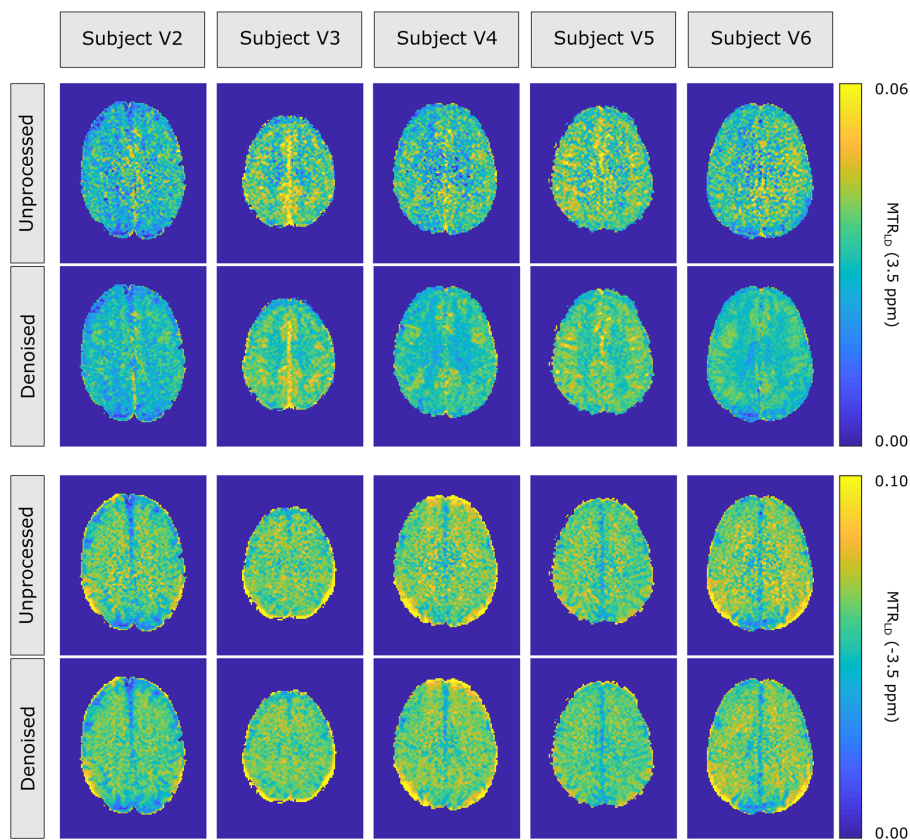


FIGURE 6 MTR_{LD} contrasts for amide (top half) and rNOE (bottom half) of five subjects (V2 to V6) acquired at 3 T. Application of the denoising algorithm using the median criterion (respective bottom rows) results in a considerable image quality gain compared with the unprocessed data (respective top rows) for all five subjects. The corresponding number of components to retain as suggested by the median criterion (also for the other two criteria) is very consistent across the subjects with an expectable small variability (Table 3)

Malinowski criterion is prone to underestimating the number of components to be retained; however, for low SNR data the criterion works well as a lower limit. In vivo, MTR_{LD} contrast images obtained from 7 T experiments exhibit only small differences after denoising with the number of components according to each of the three criteria (Figure S3). It should, however, be noted that the suggested number of components by the median criterion appears to be high and residual noise was observed. As a result, the suggested number of components in vivo is even higher than the one for the Nelson criterion, which is in strong contrast to the observed tendencies in the simulations. This might possibly be attributed to influences such as motion and B_0 -inhomogeneities and their respective correction, which so far were not considered in the simulations. These effects should be investigated further. As additional information, for each in vivo measurement and criterion, the lower limit for reliably detectable effect sizes in the Z-spectrum can be estimated with the associated eigenvalues (Figure S4; compare with Figure 3, bottom row). For the 7 T data, the SNR gain provided by PCA-based Z-spectral denoising according to the median criterion was quantified as comparable or even superior to averaging across six measurements (Figure S5). All in all, we want to emphasize that we suggest using the median criterion, which performed best in the simulations and suggests the highest number of components in vivo, to rule out any potential risk of distorted Z-spectra and contrasts at the expense of a potential suboptimal denoising performance. In any case, the Malinowski criterion represents a lower limit, which should not be fallen short of.

In general, application of the proposed denoising algorithm is not restricted to low-power Z-spectra but can be applied to any CEST-related approach providing a spectral dimension to exploit redundancies. A different choice of saturation parameters will thereby potentially affect the required number of PCs to describe the spectra because the number of resolvable spectral components will change. However, the validity of the criteria holds, which was confirmed in preliminary dualCEST³³ measurements. The achievable denoising effect will generally depend on the proportion of preserved components to acquired offsets. Thereby, the minimal number of necessary components is predetermined by the spectral

composition of the investigated object, as well as the distribution of the acquired offsets. The maximal number of components is equal to the number of acquired offsets. Therefore, the denoising effect will be diminished for approaches with only a few frequency offsets and benefits from densely sampled Z-spectra. PCA also requires a sound statistical basis to be applicable. In particular, a sufficient number of observations (ie voxels) are required. While 3D imaging easily meets this requirement, 2D imaging may not provide a sufficient number of observations for effective denoising.

To ensure correct functioning of the PCA, appropriate preprocessing of the image data is crucial. A correction for B_0 -inhomogeneities as well as for possible movements and deformations during the measurement is necessary to restore the required spectral redundancy across all voxels. Otherwise, unaddressed frequency shifts and displacements will result in distorted PCs and a higher number of necessary components to describe the data. Furthermore, prior segmentation of meaningful tissue regions in the images enables excluding the distorting influence of voxels that are dominated by fat or depict only noise.

In this study, the entire masked volume was denoised together, yielding a joint set of PCs as well as a general truncation point for WM, GM and CSF. In principal, one could also denoise the different parts of the brain separately, which should yield a reduced number of suggested PCs for each compartment and thus a better denoising performance. However, this would require additional anatomical imaging to allow segmentation, and would raise the question of how to deal with voxels which cannot be classified with absolute certainty. Furthermore, unique signatures of local CEST signals (eg in tumor) should be better described by the joint set of PCs, which covers a broader range of different CEST effects.

Application of the denoising technique to synthetic and real data demonstrated the effective and robust denoising capabilities of CEST images with a straightforward and computationally fast implementation. However, the proposed algorithm represents only a first introduction to denoising techniques to in vivo CEST data, with potential remaining for advancements. For instance, the necessary rearrangement of the image series into a 2D Casorati matrix reduces the available information to correlations between the frequency offsets and voxels. Any additional correlations concerning spatial as well as tissue interdependencies are thereby lost. More advanced denoising techniques taking this additional information into account by exploiting further redundancies in the image dimensions could potentially achieve an enhanced denoising performance for CEST imaging.

5 | CONCLUSION

The proposed denoising algorithm combines the identification of spectral redundancies by means of a PCA with an appropriate data-driven truncation criterion to separate the meaningful spectral features from noise-like characteristics. The latter is essential for the application to feature rich in vivo data, where the number of necessary components cannot be determined a priori. The given criteria additionally facilitate a straightforward assessment of data quality, providing guidance for CEST MR protocols in terms of SNR. In a benchmark test consisting of fitted in vivo Z-spectra with artificially introduced noise, the median criterion demonstrated the best performance in estimating the optimal number of necessary components. Application of the denoising algorithm to 3 and 7 T in vivo data revealed a considerable increase in image quality of the amide and rNOE contrasts, with an SNR gain comparable or even superior to that achieved by an averaging of six measurements. Applicability of the algorithm is not restricted to the investigated low-power Z-spectra but includes any CEST-related approach, providing an additional dimension to exploit redundancies. The resulting robust and effective denoising allows for a reliable detection of small CEST effects for many different applications.

ACKNOWLEDGEMENTS

The financial support of the Max Planck Society (support to J.B., M.Z. and A.D.), the German Research Foundation (DFG, grant ZA 814/2-1, support to K.H.), and the European Union's Horizon 2020 research and innovation programme (Grant Agreement No. 667510, support to M.Z. and A.D.) is gratefully acknowledged.

Johannes Breitling and Anagha Deshmane contributed equally to this work.

The authors declare no conflict of interest.

FUNDING INFORMATION

The financial support of the Max Planck Society (support to J.B., M.Z. and A.D.), the German Research Foundation (DFG, grant ZA 814/2-1, support to K.H.), and the European Union's Horizon 2020 research and innovation programme (Grant Agreement No. 667510, support to M.Z. and A.D.) is gratefully acknowledged.

ORCID

Johannes Breitling  <https://orcid.org/0000-0001-8003-5382>

Anagha Deshmane  <https://orcid.org/0000-0003-0697-0895>

Steffen Goerke  <https://orcid.org/0000-0002-0684-2423>

Moritz Zaiss  <https://orcid.org/0000-0001-9780-3616>

REFERENCES

1. Forsen S, Hoffman RA. Study of moderately rapid chemical exchange reactions by means of nuclear magnetic double resonance. *J Chem Phys.* 1963;39:2892–2901.
2. Ward K, Aletras A, Balaban R. A new class of contrast agents for MRI based on proton chemical exchange dependent saturation transfer (CEST). *J Magn Reson.* 2000;143:79–87.
3. Zhou J, Payen J-F, Wilson DA, Traaystman RJ, van Zijl PCM. Using the amide proton signals of intracellular proteins and peptides to detect pH effects in MRI. *Nat Med.* 2003;9:1085–1090.
4. Jones CK, Huang A, Xu J, et al. Nuclear Overhauser enhancement (NOE) imaging in the human brain at 7T. *Neuroimage.* 2013;77:114–124.
5. Zaiss M, Windschuh J, Paech D, et al. Relaxation-compensated CEST-MRI of the human brain at 7T: unbiased insight into NOE and amide signal changes in human glioblastoma. *Neuroimage.* 2015;112:180–188.
6. Zaiss M, Windschuh J, Goerke S, et al. Downfield-NOE-suppressed amide-CEST-MRI at 7 tesla provides a unique contrast in human glioblastoma. *Magn Reson Med.* 2017;77:196–208.
7. Zaiss M, Kunz P, Goerke S, Radbruch A, Bachert P. MR imaging of protein folding in vitro employing nuclear-Overhauser-mediated saturation transfer. *NMR Biomed.* 2013;26:1815–1822.
8. Goerke S, Zaiss M, Kunz P, et al. Signature of protein unfolding in chemical exchange saturation transfer imaging. *NMR Biomed.* 2015;28:906–913.
9. Goerke S, Milde KS, Bukowiecki R, et al. Aggregation-induced changes in the chemical exchange saturation transfer (CEST) signals of proteins. *NMR Biomed.* 2017;30:e3665.
10. Kogan F, Haris M, Singh A, et al. Method for high-resolution imaging of creatine in vivo using chemical exchange saturation transfer. *Magn Reson Med.* 2014;71:164–172.
11. Rerich E, Zaiss M, Korzowski A, Ladd ME, Bachert P. Relaxation-compensated CEST-MRI at 7 T for mapping of creatine content and pH – preliminary application in human muscle tissue in vivo. *NMR Biomed.* 2015;28:1402–1412.
12. Cai K, Haris M, Singh A, et al. Magnetic resonance imaging of glutamate. *Nat Med.* 2012;18:302–306.
13. Haris M, Nath K, Cai K, et al. Imaging of glutamate neurotransmitter alterations in Alzheimer's disease. *NMR Biomed.* 2013;26:386–391.
14. Aime S, Calabi L, Biondi L, et al. Iopamidol: exploring the potential use of a well-established x-ray contrast agent for MRI. *Magn Reson Med.* 2005;53:830–834.
15. Longo DL, Busato A, Lanzardo S, Antico F, Aime S. Imaging the pH evolution of an acute kidney injury model by means of iopamidol, a MRI-CEST pH-responsive contrast agent. *Magn Reson Med.* 2013;70:859–864.
16. Jones KM, Randtke EA, Howison CM, et al. Measuring extracellular pH in a lung fibrosis model with acidoCEST MRI. *Mol Imaging Biol.* 2015;17:177–184.
17. Chan KWY, McMahon MT, Kato Y, et al. Natural D-glucose as a biodegradable MRI contrast agent for detecting cancer. *Magn Reson Med.* 2012;68:1764–1773.
18. Walker-Samuel S, Ramasawmy R, Torrealdea F, et al. In vivo imaging of glucose uptake and metabolism in tumors. *Nat Med.* 2013;19:1067–1072.
19. Xu X, Yadav NN, Knutsson L, et al. Dynamic glucose-enhanced (DGE) MRI: translation to human scanning and first results in glioma patients. *Tomography.* 2015;1:105–114.
20. Schuenke P, Koehler C, Korzowski A, et al. Adiabatically prepared spin-lock approach for T1ρ-based dynamic glucose enhanced MRI at ultrahigh fields. *Magn Reson Med.* 2017;78:215–225.
21. Nasrallah FA, Pagès G, Kuchel PW, Golay X, Chuang K-H. Imaging brain deoxyglucose uptake and metabolism by glucoCEST MRI. *J Cereb Blood Flow Metab.* 2013;33:1270–1278.
22. Rivlin M, Tsarfaty I, Navon G. Functional molecular imaging of tumors by chemical exchange saturation transfer MRI of 3-O-methyl-D-glucose. *Magn Reson Med.* 2014;72:1375–1380.
23. Zaiss M, Schuppert M, Deshmane A, et al. Chemical exchange saturation transfer MRI contrast in the human brain at 9.4 T. *Neuroimage.* 2018;179:144–155.
24. Cai K, Singh A, Poptani H, et al. CEST signal at 2 ppm (CEST@2ppm) from Z-spectral fitting correlates with creatine distribution in brain tumor. *NMR Biomed.* 2014;28:1–8.
25. Paech D, Burth S, Windschuh J, et al. Nuclear Overhauser enhancement imaging of glioblastoma at 7 tesla: region specific correlation with apparent diffusion coefficient and histology. *PLoS ONE.* 2015;10:1–16.
26. Paech D, Windschuh J, Oberhollenzer J, et al. Assessing the predictability of IDH mutation and MGMT methylation status in glioma patients using relaxation-compensated multipool CEST MRI at 7.0 T. *Neuro Oncol.* 2018;20:1661–1671.
27. Jiang S, Zou T, Eberhart CG, et al. Predicting IDH mutation status in grade-II gliomas using amide proton transfer-weighted (APT_w) MRI. *Magn Reson Med.* 2017;78:1100–1109.
28. Jiang S, Rui Q, Wang Y, et al. Discriminating MGMT promoter methylation status in patients with glioblastoma employing amide proton transfer-weighted MRI metrics. *Eur Radiol.* 2018;28:2115–2123.
29. Meissner J-E, Korzowski A, Regnery S, et al. Early response assessment of glioma patients to definitive chemoradiotherapy using chemical exchange saturation transfer imaging at 7 T. *J Magn Reson Imaging.* 2019. <https://doi.org/10.1002/jmri.26702>
30. Regnery S, Adebeg S, Dreher C, et al. Chemical exchange saturation transfer MRI serves as predictor of early progression in glioblastoma patients. *Oncotarget.* 2018;9:28772–28783.

31. Desmond KL, Mehrabian H, Chavez S, et al. Chemical exchange saturation transfer for predicting response to stereotactic radiosurgery in human brain metastasis. *Magn Reson Med*. 2017;78:1110–1120.
32. Mehrabian H, Myrehaug S, Soliman H, Sahgal A, Stanisz GJ. Evaluation of glioblastoma response to therapy with chemical exchange saturation transfer. *Int J Radiat Oncol*. 2018;101:713–723.
33. Goerke S, Breitling J, Zaiss M, et al. Dual-frequency irradiation CEST-MRI of endogenous bulk mobile proteins. *NMR Biomed*. 2018;31:e3920.
34. Deshmane A, Zaiss M, Lindig T, et al. 3D gradient echo snapshot CEST MRI with low power saturation for human studies at 3T. *Magn Reson Med*. 2019;81:2412–2423.
35. Windschuh J, Zaiss M, Meissner J-E, et al. Correction of B₁-inhomogeneities for relaxation-compensated CEST imaging at 7 T. *NMR Biomed*. 2015;28:529–537.
36. Jin T, Wang P, Zong X, Kim S-G. MR imaging of the amide-proton transfer effect and the pH-insensitive nuclear overhauser effect at 9.4 T. *Magn Reson Med*. 2013;69:760–770.
37. Zhou IY, Wang E, Cheung JS, Zhang X, Fulci G, Sun PZ. Quantitative chemical exchange saturation transfer (CEST) MRI of glioma using image downsampling expedited adaptive least-squares (IDEAL) fitting. *Sci Rep*. 2017;7:84.
38. Zaiss M, Ehses P, Scheffler K. Snapshot-CEST: optimizing spiral-centric-reordered gradient echo acquisition for fast and robust 3D CEST MRI at 9.4 T. *NMR Biomed*. 2018;31:e3879.
39. Eckart C, Young G. The approximation of one matrix by another of lower rank. *Psychometrika*. 1936;1:211–218.
40. Hotelling H. Analysis of a complex of statistical variables into principal components. *J Educ Psychol*. 1933;24:417–441.
41. Döpfert J, Witte C, Kunth M, Schröder L. Sensitivity enhancement of (hyper-)CEST image series by exploiting redundancies in the spectral domain. *Contrast Media Mol Imaging*. 2014;9:100–107.
42. Wech T, Köstler H. Robust motion correction in CEST imaging exploiting low-rank approximation of the z-spectrum. *Magn Reson Med*. 2018;80:1979–1988.
43. Balvay D, Kachenoura N, Espinoza S, et al. Signal-to-noise ratio improvement in dynamic contrast-enhanced CT and MR imaging with automated principal component analysis filtering. *Radiology*. 2011;258:435–445.
44. Veraart J, Novikov DS, Christiaens D, Ades-aron B, Sijbers J, Fieremans E. Denoising of diffusion MRI using random matrix theory. *Neuroimage*. 2016;142:394.
45. Kaiser HF. The varimax criterion for analytic rotation in factor analysis. *Psychometrika*. 1958;23:187–200.
46. Valle S, Li W, Qin SJ. Selection of the number of principal components: the variance of the reconstruction error criterion with a comparison to other methods. *Ind Eng Chem Res*. 1999;38:4389–4401.
47. Malinowski ER. Theory of error in factor analysis. *Anal Chem*. 1977;49:606–612.
48. Malinowski ER. Determination of the number of factors and the experimental error in a data matrix. *Anal Chem*. 1977;49:612–617.
49. Cattell RB. The scree test for the number of factors. *Multivar Behav Res*. 1966;1:245–276.
50. Nelson LR. Some observations on the scree test, and on coefficient alpha. *J Educ Res Meas*. 2005;3:1–17.
51. Manjón JV, Coupé P, Buades A. MRI noise estimation and denoising using non-local PCA. *Med Image Anal*. 2015;22:35–47.
52. Schuenke P, Windschuh J, Roeloffs V, Ladd ME, Bachert P, Zaiss M. Simultaneous mapping of water shift and B₁ (WASABI)-application to field-inhomogeneity correction of CESTMRI data. *Magn Reson Med*. 2017;77:571–580.
53. Cox RW, Hyde JS. Software tools for analysis and visualization of fMRI data. *NMR Biomed*. 1997;10:171–178.
54. Nolden M, Zelzer S, Seitel A, et al. The medical imaging interaction toolkit: challenges and advances: 10 years of open-source development. *Int J Comput Assist Radiol Surg*. 2013;8:607–620.
55. Windschuh J, Zaiss M, Meissner J-E, et al. Correction of B₁-inhomogeneities for relaxation-compensated CEST imaging at 7 T. *NMR Biomed*. 2015;28:529–537.
56. Aja-Fernández S, Tristán-Vega A, Hoge WS. Statistical noise analysis in GRAPPA using a parametrized noncentral chi approximation model. *Magn Reson Med*. 2011;65:1195–1206.
57. Foi A. Noise estimation and removal in MR imaging: the variance-stabilization approach. In: 2011 IEEE International Symposium on Biomedical Imaging: from Nano to Macro;2011:1809–1814.

SUPPORTING INFORMATION

Additional supporting information may be found online in the Supporting Information section at the end of the article.

How to cite this article: Breitling J, Deshmane A, Goerke S, et al. Adaptive denoising for chemical exchange saturation transfer MR imaging. *NMR in Biomedicine*. 2019:e4133. <https://doi.org/10.1002/nbm.4133>

DOI: 10.1002/nbm.4278

ERRATUM

NMR
IN BIOMEDICINE WILEY

A joint authorship statement was mistakenly omitted from the article by Breitling et al.¹ The statement is given here:
Johannes Breitling and Anagha Deshmane contributed equally to this work.

REFERENCES

1. Breitling J, Deshmane A, Goerke S, et al. Adaptive denoising for chemical exchange saturation transfer MR imaging. *NMR Biomed.* 2019;32:e4133. <https://doi.org/10.1002/nbm.4133>

Publication IV

Optimized dualCEST-MRI for imaging of endogenous bulk mobile proteins in the human brain

Authors: Johannes Breitling, Jan-Eric Meissner, Moritz Zaiss, Daniel Paech, Mark E. Ladd, Peter Bachert, and Steffen Goerke

Journal reference: NMR in Biomedicine. 2020;33:e4262.

DOI: 10.1002/nbm.4262

Author contributions: **JB** designed the study with support of **SG**, implemented the new pulses for the imaging sequence, conceived and developed the novel weighted acquisition scheme and performed all data acquisition, analysis and interpretation. **JEM** assisted during the in vivo measurements for the reproducibility study. **DP** was responsible for the patient enrollment and medical supervision during the study. **JB** drafted and revised the manuscript with support from **SG** and critical review from all co-authors.



RESEARCH ARTICLE

NMR
IN BIOMEDICINE WILEY

Optimized dualCEST-MRI for imaging of endogenous bulk mobile proteins in the human brain

Johannes Breitling^{1,2,3} | Jan-Eric Meissner¹ | Moritz Zaiss⁴ | Daniel Paech⁵ |
Mark E. Ladd^{1,3,6} | Peter Bachert^{1,3} | Steffen Goerke¹ ¹Division of Medical Physics in Radiology, German Cancer Research Center (DKFZ), Heidelberg, Germany²Max-Planck-Institute for Nuclear Physics, Heidelberg, Germany³Faculty of Physics and Astronomy, University of Heidelberg, Heidelberg, Germany⁴Department of High-Field Magnetic Resonance, Max-Planck-Institute for Biological Cybernetics, Tuebingen, Germany⁵Department of Radiology, German Cancer Research Center (DKFZ), Heidelberg, Germany⁶Faculty of Medicine, University of Heidelberg, Heidelberg, Germany

Correspondence

Dr. rer. nat. Steffen Görke, Im Neuenheimer Feld 280, 69120 Heidelberg, Baden-Württemberg, Germany.
Email: s.goerke@dkfz.de

Funding information

German Research Foundation, Grant/Award Number: GO 2172/1-1

Dual-frequency irradiation chemical exchange saturation transfer (dualCEST) allows imaging of endogenous bulk mobile proteins by selectively measuring the intramolecular spin diffusion. The resulting specificity to changes in the concentration, molecular size, and folding state of mobile proteins is of particular interest as a marker for neurodegenerative diseases and cancer. Until now, application of dualCEST in clinical trials was prevented by the inherently small signal-to-noise ratio and the resulting comparatively long examination time. In this study, we present an optimized acquisition protocol allowing 3D dualCEST-MRI examinations in a clinically relevant time frame. The optimization comprised the extension of the image readout to 3D, allowing a retrospective co-registration and application of denoising strategies. In addition, cosine-modulated dual-frequency presaturation pulses were implemented with a weighted acquisition scheme of the necessary frequency offsets. The optimization resulted in a signal-to-noise ratio gain by a factor of approximately 8. In particular, the application of denoising and the motion correction were the most crucial improvement steps. In vitro experiments verified the preservation of specificity of the dualCEST signal to proteins. Good-to-excellent intra-session and good inter-session repeatability was achieved, allowing reliable detection of relative signal differences of about 16% or higher. Applicability in a clinical setting was demonstrated by examining a patient with glioblastoma. The optimized acquisition protocol for dualCEST-MRI at 3 T enables selective imaging of endogenous bulk mobile proteins under clinically relevant conditions.

KEYWORDS

APT, dualCEST, MRI, optimization, repeatability, rNOE

Abbreviations: APT, amide proton transfer; APT_w, APT-weighted; BSA, bovine serum albumin; CEST, chemical exchange saturation transfer; CSF, cerebrospinal fluid; DC, duty cycle; dualCEST, dual-frequency irradiation CEST; GM, grey matter; HC, hair conditioner; ICC, intraclass correlation coefficient; LOA, limits of agreement; M₀, equilibrium water magnetization; M_{sat}, water magnetization after presaturation; MTR_{inv}, inverse magnetization transfer ratio; rNOE, relayed nuclear Overhauser effect; SNR, signal-to-noise ratio; ssMT, semi-solid magnetization transfer; t_p, interpulse delay; t_{pr}, pulse length; T_{protein}, isolated saturation cross-talk of mobile proteins; t_{sat}, saturation length; T (Δω₁, Δω₂), saturation cross-talk; WM, white matter; Z, Z-spectrum; Δω₁, frequency offset; Δω₂, constant frequency offset; Δω_{center}, carrier frequency offset; Δω_{modulation}, modulation frequency; Δω_{off}, far off-resonant frequency offset; Δω_{ssMT}, ssMT selective frequency offset.

This is an open access article under the terms of the Creative Commons Attribution-NonCommercial-NoDerivs License, which permits use and distribution in any medium, provided the original work is properly cited, the use is non-commercial and no modifications or adaptations are made.

© 2020 The Authors. NMR in Biomedicine published by John Wiley & Sons Ltd

1 | INTRODUCTION

Chemical exchange saturation transfer (CEST) MRI¹⁻³ has emerged as an important imaging modality for the detection of low concentration organic compounds in living tissue such as peptides and proteins⁴⁻⁷ and various other metabolites.⁸⁻¹⁰ In particular, CEST signals attributed to protons have been shown to provide information of clinical interest, such as the amide proton transfer (APT)⁴ signal and the relayed nuclear Overhauser effect (rNOE)⁶ of aliphatic protons. Applications range from tumor detection,^{11,12} grading,^{13,14} and therapy response assessment¹⁵⁻¹⁷ to the diagnosis of neurological diseases such as Alzheimer's,^{18,19} Parkinson's,²⁰ and multiple sclerosis.²¹ However, the superposition of signals from various cellular compounds in living tissues as well as their dependence on physiological conditions (i.e. pH and/or temperature)^{4,22,23} prevents exclusive assignment of the observed effects to proteins. Although the value of conventional protein-weighted CEST-MRI has been demonstrated in diverse studies, increased specificity to proteins would allow better assessment of the actual protein contribution to CEST signal changes in disease states, which may reveal so far undetected effects and correlations.

Recently, dual-frequency irradiation CEST (dualCEST)²⁴ has been introduced as a novel technique overcoming these limitations. This method allows the selective detection of endogenous bulk mobile proteins in vivo without contributions from saturation transfer effects of metabolites, lipids, or semi-solids. The specificity of this approach is achieved by using the coupling of different CEST signals as a distinguishing feature.^{24,25} Detection of this coupling is accomplished by extending the RF presaturation scheme to a simultaneous irradiation at two frequency offsets. The dualCEST signal depends on changes in bulk mobile protein concentration, average molecular size, and global folding state.^{24,26-28} Due to its specificity and sensitivity, dualCEST could serve as a reference for assessing the assignment of conventional CEST approaches to proteins and may lead to novel insights into the origin of protein-related CEST contrasts in vivo. Furthermore, dualCEST is of interest as a non-invasive imaging technique for diseases associated with structural and conformational changes of proteins such as cancer and neurodegenerative diseases. However, until now, application in a clinical setting was prevented by the inherently small signal-to-noise ratio (SNR) in comparison with conventional CEST approaches.

The aim of this work was to realize a clinically applicable dualCEST-MRI protocol at 3 T, with comparable image quality, examination duration, and reproducibility to conventional protein CEST modalities. To achieve this goal we applied several methodological developments: (i) implementation of cosine-modulated pulses^{29,30} allowed for a simultaneous presaturation at two frequency offsets; and was additionally combined with (ii) a weighted acquisition scheme for optimal averaging. Furthermore, (iii) utilization of a 3D snapshot-CEST³¹ image readout allowed for retrospective motion correction and (iv) facilitated the application of advanced denoising strategies.³² Preservation of specificity of the optimized dualCEST protocol was demonstrated in vitro. Reproducibility was quantified by repeated in vivo measurements. Finally, clinical relevance was demonstrated by examining a patient with glioblastoma.

2 | METHODS

2.1 | DualCEST approach

2.1.1 | Theory

DualCEST allows the coupling between CEST signals resonating at two different frequency offsets to be measured. In proteins, the observed magnetization transfer—saturation crosstalk,²⁴ T —is attributed to the intramolecular spin diffusion between dipolar-coupled protons. DualCEST is based on acquiring the water MR signal after a dual frequency irradiation at a frequency offset pair, $\Delta\omega$ and $\Delta\omega_c$. The corresponding Z -value is calculated by normalizing the presaturated signal, $M_{\text{sat}}(\Delta\omega, \Delta\omega_c)$, by the equilibrium magnetization, M_0 : $Z(\Delta\omega, \Delta\omega_c) = M_{\text{sat}}(\Delta\omega, \Delta\omega_c)/M_0$. The saturation crosstalk, T , which quantifies the coupling between the two frequency offsets, can be calculated according to²⁴:

$$T(\Delta\omega, \Delta\omega_c) = \frac{R_1}{DC} \left[\frac{1}{Z(\Delta\omega, \Delta\omega_{\text{off}})} + \frac{1}{Z(\Delta\omega_{\text{off}}, \Delta\omega_c)} - \frac{1}{Z(\Delta\omega, \Delta\omega_c)} - \frac{1}{Z(\Delta\omega_{\text{off}}, \Delta\omega_{\text{off}})} \right] \quad (1)$$

where the far off-resonant frequency offset, $\Delta\omega_{\text{off}} = 295$ ppm, is synonymous with disabling the saturation.

A comparatively broad saturation crosstalk of semi-solid macromolecular structures (ssMT, semi-solid magnetization transfer) is detected in vivo, in addition to signals of mobile proteins. To isolate the superimposed signal of mobile proteins, the contribution of the ssMT has to be subtracted. The actual amplitude thereof is determined by measuring combinations of the crosstalk between frequency offset pairs specific to the ssMT²⁴:

$$T_{\text{protein}}(\Delta\omega, \Delta\omega_c) = T(\Delta\omega, \Delta\omega_c) - \frac{T(\Delta\omega, -\Delta\omega_{\text{ssMT}}) \cdot T(\Delta\omega_{\text{ssMT}}, \Delta\omega_c)}{T(\Delta\omega_{\text{ssMT}}, -\Delta\omega_{\text{ssMT}})} \quad (2)$$

where $\Delta\omega_{\text{ssMT}} = 30$ ppm is a frequency offset off-resonant for proteins but on-resonant for ssMT. Note that this correction approach is independent of the ssMT line shape and enables removal of both symmetric and asymmetric contributions.

2.1.2 | Cosine-modulated pulses

Dual-frequency irradiation at a frequency offset pair, $\Delta\omega$ and $\Delta\omega_c$, can be achieved by either (i) using an alternating RF irradiation scheme (Figure 1A) or (ii) modulating the employed Gaussian-shaped RF pulses with a cosine (Figure 1B). With this irradiation, a more efficient simultaneous presaturation at both frequency offsets is achieved, with pulses centered at $\Delta\omega_{\text{center}} = (\Delta\omega + \Delta\omega_c)/2$ and modulation frequency $\Delta\omega_{\text{modulation}} = (\Delta\omega - \Delta\omega_c)/2$.^{29,30} Both presaturation types are characterized by their respective mean amplitude, $B_1 = \text{flip angle}/(\gamma \cdot t_p)$, pulse length, t_p , and duty cycle, $\text{DC} = t_p/(t_p + t_d)$. Note that for dualCEST the DC is defined per frequency offset, implying a maximum of 50% for alternating pulses. For the cosine-modulated pulses the mean amplitude of the enveloping Gaussian is set to $2 \cdot B_1$, such that each frequency component effectively receives the desired mean amplitude B_1 .

Imperfections of the cosine modulation, e.g. due to the limited number of 8000 digitized steps per pulse of our Siemens scanner (IDEA VE11C), result in small deviations from the anticipated saturation as well as residual carrier leakage at $\Delta\omega_{\text{center}} = 0$ ppm (Figure 1C inset). To compensate for these deviations, slightly asymmetric frequency offsets were chosen to prevent unintentional direct water saturation. Furthermore, frequency offset pairs, including a far-off resonant irradiation, are acquired using Gaussian RF pulses without cosine modulation to avoid the corresponding very high modulation frequency and the consequent poor modulation with only a few digitized steps per cycle. With this approach, the maximum spacing needed for acquisition of $M_{\text{sat}}(\Delta\omega_{\text{ssMT}}, -\Delta\omega_{\text{ssMT}})$ is limited to 60 ppm, resulting in a sufficiently high number of at least 108 digitized steps per period of the cosine modulation (using $t_p = 20$ ms at $B_0 = 3$ T).

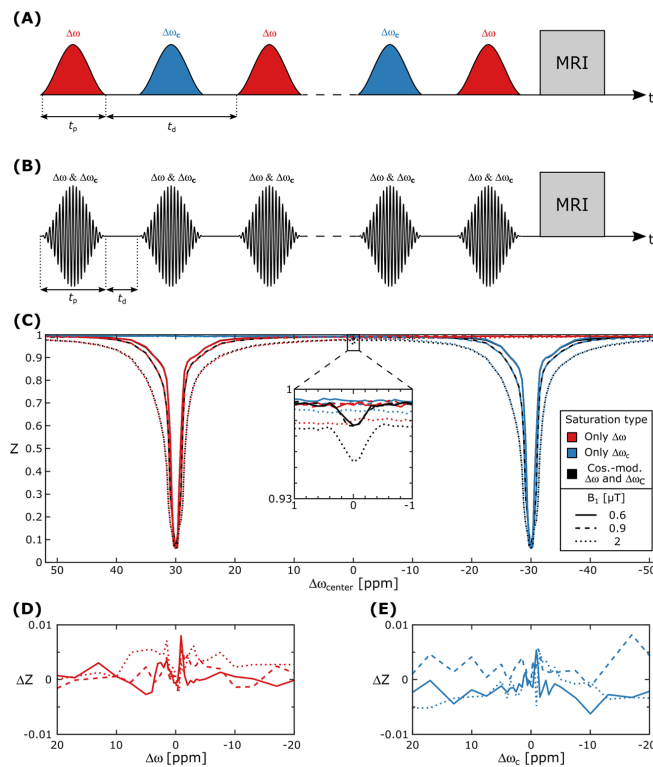


FIGURE 1 Implementation of cosine-modulated saturation. Dual-frequency saturation schemes can be achieved by using either alternating RF irradiation (A) or the more efficient cosine-modulated pulses (B). Z-spectra (C) acquired using single-frequency irradiation (red and blue, respectively) and cosine-modulated pulses (black, fixed spacing of $\Delta\omega_{\text{modulation}} = 30$ ppm) exhibit only small differences (D, E), verifying the functionality of the modulation. A small residual carrier leakage can be seen as attenuation around $\Delta\omega_{\text{center}} = 0$ ppm (inset in C)

2.1.3 | Weighted acquisition scheme

In principle, acquisition of nine Z-values is sufficient for the calculation of the final dualCEST contrast, T_{protein} (Equation (2)). Certain frequency offset pairs have a larger impact on the final contrast quality than others, due to different amplitudes and resulting relative errors of the Z-values, as well as their multiple usage in the calculation. As dualCEST-MRI requires multiple repetitions to be averaged in order to accumulate enough SNR, averaging the higher impact Z-values more often will ultimately reduce the error of the final contrast while maintaining the same number of total repetitions. The impact of each Z-value can be calculated by Gaussian error propagation using the covariance matrix, Σ , of the nine Z-values and the respective Jacobian matrices, J_1 and J_2 , of Equations (1) and (2) (Supplementary Information). By assuming an uncorrelated error with the same variance, σ^2 , for each measurement, the entries of Σ will only depend on the number of repetitions, $N = (n_1, \dots, n_9)$, acquired and thus can be written without loss of generality as

$$\Sigma_{ij} = \begin{cases} \sigma^2/n_i & \text{if } i = j \\ 0 & \text{otherwise.} \end{cases} \quad (3)$$

The optimal distribution of averages, N_{opt} , for a fixed number of repetitions, $n = \sum n_i$, can be determined by minimizing the error, i.e. variance, of the final contrast:

$$N_{\text{opt}} = \arg \min_N J_2 \cdot J_1 \cdot \Sigma \cdot J_1^T \cdot J_2^T. \quad (4)$$

This result is independent of σ^2 and is therefore valid for all noise levels. However, determination of the Jacobian matrices requires the actual Z-values and will result in a different N_{opt} depending on the tissue and saturation parameters. The optimal distribution for the intended in vivo protocol was therefore determined as the median of the optimal samplings calculated for all voxels of a measurement.

2.2 | Materials

2.2.1 | Subjects

In vivo examinations were approved by the local ethics committee of the Medical Faculty of the University of Heidelberg and are in accordance with relevant guidelines and regulations. Written informed consent was obtained prior to the experiment. Two healthy male volunteers (aged 26 and 28 years) were recruited. One was scanned as part of the optimization of the sequence and post-processing; the other was scanned for the repeatability analysis twice on two different days (four times total) without repositioning in between the scans of each session. One patient with newly diagnosed glioblastoma (WHO grade IV) was examined before therapy using an imaging protocol consisting of (i) conventional T_{1w} , (ii) relaxation-compensated APT and rNOE CEST, (iii) dualCEST, and (iv) APT-weighted (APT_w) CEST. The image data obtained with the first two (i.e. contrast-enhanced T_{1w} and MTR_{rex} amide and rNOE) have been published previously³³ and were re-used as reference in this study (see Figure 5 later).

2.2.2 | Model solutions

Three model solutions were prepared consisting of the main contributions in the Z-spectrum: proteins, metabolites, and ssMT. Bovine serum albumin (BSA, 5% (w/v)) and hair conditioner (HC, 50% (w/v)) (Schwarzkopf Gliss Kur Spelung, Henkel, Dusseldorf, Germany) were selected to model mobile proteins and ssMT respectively. HC has already been utilized in previous studies concerning CEST and ssMT due to its lamellar structure resulting in molecular and structural properties of neural tissue in white matter (WM).^{19,34} Metabolite contributions were represented by a solution containing creatine (15 mM), carnosine (50 mM), and glutamate (25 mM). All model solutions were buffered at pH 7.3 using phosphate-buffered saline and titrated using NaOH or HCl. The phantom was measured at room temperature.

2.3 | MRI protocol

2.3.1 | Imaging readout

The following imaging readout was utilized for all CEST-related measurements in this study. All measurements were made on a 3 T whole-body MR-scanner (MAGNETOM Prisma; Siemens Healthineers, Erlangen, Germany) using the vendor's 64-channel head/neck coil. The image-readout parameters of the employed 3D spiral-centric-reordered gradient-echo acquisition (snapshot CEST³¹) were taken from a previously established

protocol³³: GRAPPA acceleration factor = 2, $T_E = 2.75$ ms, $T_R = 5.5$ ms, bandwidth = 340 Hz/pixel, flip angle = 7° , elongation factor = 0.5, with FOV = $140 \times 140 \times 48$ mm³ and matrix size $128 \times 128 \times 16$ yielding a $1.1 \times 1.1 \times 3$ mm³ resolution for the in vitro measurement, and FOV = $220 \times 180 \times 48$ mm³ and matrix size $128 \times 104 \times 16$ yielding a $1.7 \times 1.7 \times 3$ mm³ resolution for the in vivo measurement. The resulting readout time for one 3D image was 3.6 s. The outer two slices on both sides were discarded due to aliasing artifacts in the slice direction, resulting in effectively 12 slices. All in vivo image data were motion corrected using an automatic multimodal rigid registration algorithm in MITK,^{35,36} with the exception of the two dualCEST acquisitions used for the respective comparison (see Figure 2A and 2B later).

In addition, B_0 and B_1 mapping were acquired by the WASABI³⁷ (simultaneous mapping of water shift and B_1) approach and a T_1 map using a saturation recovery sequence. The acquisition time for WASABI and T_1 mapping was 3 min 41 s and 1 min 58 s, respectively.

2.3.2 | DualCEST

Presaturation for the in vivo dualCEST measurement was achieved by either 255 cosine-modulated Gaussian-shaped RF pulses with DC = 85% or, for the comparison study, with 129 pairs of Gaussian-shaped RF pulses with DC = 43% (Figure 2A), both with an effective mean amplitude $B_1 = 2$ μ T, pulse duration $t_p = 20$ ms, effective interpulse delay $t_d = 3.5$ ms, and a resulting total saturation time of $t_{\text{sat}} = 6$ s. For the phantom measurement, the saturation was extended to 500 cosine-modulated Gaussian-shaped RF pulses to ensure steady-state saturation considering the anticipated longer T_1 .

The nine frequency offset pairs required for calculation of T_{protein} are given for the cosine-modulated pulses by the combination of $\Delta\omega = \{295, 29, 3.5\}$ ppm with $\Delta\omega_c = \{295, -31, -5.5\}$ ppm. To avoid unintentional direct water saturation at the carrier frequency, these pairs are slightly shifted compared with the pairs used for the alternating dualCEST irradiation, $\Delta\omega = \{295, 30, 5\}$ ppm and $\Delta\omega_c = \{295, -30, -5\}$ ppm. For averaging, 90 saturated images were acquired in total, with the repetitions distributed either in an optimized weighted scheme (Supplementary Information) or uniformly (10 repetitions each). For normalization, M_0 was acquired with 12 s of relaxation and saturation at -300 ppm at the beginning and end of the dualCEST experiment and interpolated to obtain an individual M_0 for each saturated image. The acquisition duration for the dualCEST data was 15 min 5 s in total.

The resulting Z-data were first denoised using an algorithm based on principal component analysis³² with the number of components determined according to the Malinowski criterion, and subsequently averaged to obtain the required nine Z-images. The final T_{protein} contrast—as calculated from Equations (1) and (2)—was corrected for B_1 inhomogeneities by the “one-point-contrast correction” method.^{24,38} However, a correction for B_0 inhomogeneities is not necessary due to the comparatively broad dualCEST resonances at 3 T.

2.3.3 | Z-spectroscopy

For the characterization of the cosine modulation, presaturation was achieved by 500 either cosine-modulated or conventional Gaussian-shaped RF pulses with a mean amplitude $B_1 = 0.6, 0.9,$ or 2 μ T, $t_p = 20$ ms, $t_d = 3.5$ ms, and DC = 85%, resulting in $t_{\text{sat}} = 12$ s. The longer saturation duration is necessary to ensure steady-state saturation despite the anticipated longer T_1 . Z-spectra were sampled at 97 frequency offsets in unequal steps between ± 52 ppm. The obtained Z-spectra were corrected for B_0 inhomogeneities.

For the in vitro specificity investigation, presaturation was achieved by 480 Gaussian-shaped RF pulses with a mean amplitude $B_1 = 0.7$ or 2 μ T, $t_p = 20$ ms, $t_d = 5$ ms, DC = 80%, resulting in $t_{\text{sat}} = 12$ s. Z-spectra were sampled at 57 frequency offsets in unequal steps between ± 250 ppm. The obtained Z-spectra were corrected for B_0 inhomogeneities.

2.3.4 | APT_w CEST

In vitro APT_w CEST contrast images were generated from the Z-spectra acquired with $B_1 = 2$ μ T by calculating the asymmetric magnetization transfer ratio ($\text{MTR}_{\text{asym}} = Z(-\Delta\omega) - Z(\Delta\omega)$) at $\Delta\omega = 3.5$ ppm.

Presaturation for the in vivo APT_w measurement was achieved using four block RF pulses ($B_1 = 2$ μ T, $t_p = 20$ ms, $t_d = 1$ ms, DC = 95%)³⁹ with Z-spectra sampled at -300 (1), ± 4 (1), ± 3.75 (2), ± 3.5 (2), ± 3.25 (2), and ± 3 (1) ppm, where the number in the parenthesis is the number of repetitions acquired for averaging. APT_w CEST contrast images were generated from B_0 -corrected Z-spectra by calculating MTR_{asym} at $\Delta\omega = 3.5$ ppm.

2.4 | Test-retest reliability in a healthy volunteer

Comparability of the different acquisitions was ensured by aligning the dualCEST images. To do so, the first image of every scan (the M_0 image of WASABI) was co-registered to the first scan of the first session. The corresponding transformation matrices were subsequently applied to the

dualCEST contrasts to obtain comparable images. Bland-Altman plots⁴⁰ and intraclass correlation coefficients (ICCs)⁴¹ were used to evaluate the intra-session, i.e. two consecutive scans without repositioning in between, and inter-session repeatability of the technique. To obtain a more meaningful assertion with regard to a possible diagnostic application, the mean of $3 \times 3 \times 1$ regions was used as input for the evaluations instead of single-voxel values. For intra-session repeatability, the first scan of each session was compared with the corresponding second scan, with the scans separated by 20 min 44 s. For inter-session repeatability, the respective first and second scans of both sessions were compared with each other, with the two sessions separated by 4 d. For each Bland-Altman analysis the bias was calculated as the median of the relative differences between the two measurements and the limits of agreement (LOA) as the corresponding 2.5th and 97.5th percentiles such that 95% of the deviations lay within them. ICC estimates and their 95% confidence intervals were calculated using IBM SPSS Statistics Subscription (Build 1.0.0.1246; IBM, Armonk, NY) based on a single-measurement, absolute-agreement, two-way mixed-effects model. The ICC is a statistical quantity (i.e. an estimate of the true value); therefore, the corresponding 95% confidence interval was taken into account for the assessment and interpretation of the reliability.⁴¹ The respective combined data set of either both sessions or both scans was used as input for the intra- and inter-session repeatability. To obtain an estimate for the overall repeatability, all four measurements were compared with one another. In the ideal case of perfect repeatability and no noise, the bias and LOA would be zero and the ICC would be one.

3 | RESULTS

3.1 | Optimization and validation

Correct implementation and functionality of the cosine-modulated pulses was verified in a BSA phantom using a constant modulation frequency of $\Delta\omega_{\text{modulation}} = 30$ ppm. The resulting Z-spectrum (Figure 1C, black line) exhibits the expected features of the dual-frequency irradiation: a superposition of two conventional Z-spectra centered at $\Delta\omega_{\text{center}} \pm 30$ ppm. Measurements using only the corresponding single-frequency irradiation ($\Delta\omega = \Delta\omega_{\text{center}} + 30$ ppm and $\Delta\omega_c = \Delta\omega_{\text{center}} - 30$ ppm) show nearly identical Z-spectra (Figure 1C, red and blue, respectively) with only small deviations ($|\Delta Z| \leq 0.005$) compared with the cosine-modulated irradiation (Figure 1D and 1E). The very close agreement of the Z-spectra generated by single- and dual-frequency irradiation confirms the correct implementation and functionality. However, a small residual carrier frequency leakage around $\Delta\omega_{\text{center}} = 0$ ppm is observable (Figure 1C inset). As the resulting interfering direct water saturation would ultimately distort the dualCEST signal, a slightly asymmetric center frequency ($|\Delta\omega_{\text{center}}| \geq 1$ ppm) was used. This asymmetry was large enough to consider possible B_0 field inhomogeneities.

Application of the cosine-modulated pulses in vivo (Figure 2B) resulted, compared with the reference image acquired using the alternating dual-frequency irradiation (Figure 2A), in a small but insignificant SNR gain ($34 \pm 47\%$) across various tissue regions (Supporting Information

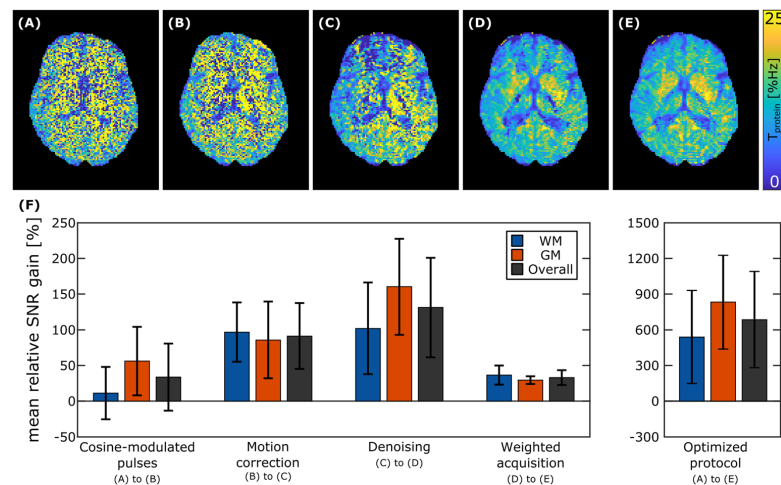


FIGURE 2 Improvements achieved by optimization of the dualCEST acquisition and post-processing (Slice 1 of 12): reference (A), cosine-modulated pulses (B), and additional motion correction (C), which is essential for the application of the denoising (D), and an optimized weighted acquisition scheme (E). The improvement achieved by each step was quantified by determining the mean relative SNR gain for regions of interest in WM (blue), GM (orange), and combining the two (grey) (F). The error bars represent the corresponding standard deviations of the obtained means. The SNR estimate was calculated by dividing the mean by the standard deviation for each region of interest (as defined in Supporting Information Figure S1)

FIGURE 3 Protein specificity of dualCEST at B_0 3 T. Model solutions (inset in A) containing BSA (orange), HC (blue), and a metabolite mixture (green) show characteristic signal contributions in the respective mean Z-spectra (B_1 0.7 T) (A, B). The conventional APT_w image exhibits a positive signal for both proteins and metabolites (C), whereas the dualCEST contrast is specific to proteins (D)

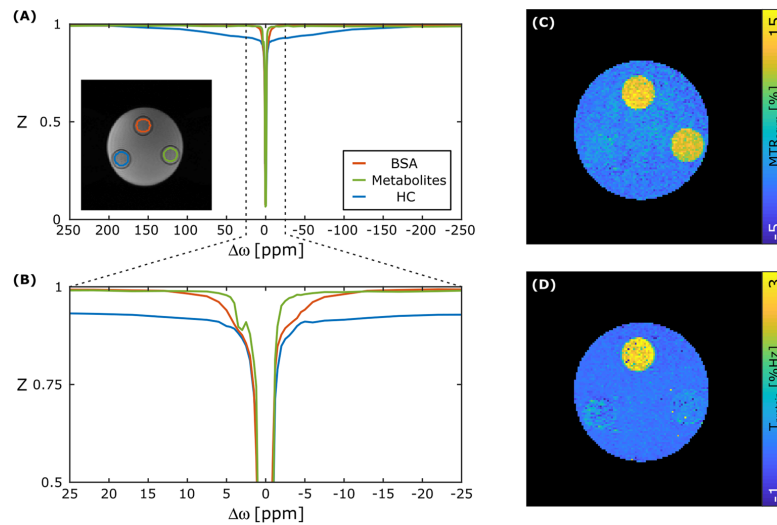


Figure S1, including the absolute SNR values). However, both images are noisy, allowing only the cerebrospinal fluid (CSF) to be distinguished, but no grey matter (GM) or WM structures. Additional co-registration of the image data to correct for potential motion artefacts yielded a smoother dualCEST contrast (SNR gain of $91 \pm 46\%$), but with a patchy and asymmetric appearance (Figure 2C). Initially, motion correction seems therefore to be unnecessary or even adverse. However, motion correction is a prerequisite for effective utilization of denoising strategies and should not be omitted. Application of a denoising approach based on a principal component analysis resulted in a tremendous improvement in image quality (SNR gain of $131 \pm 70\%$) (Figure 2D). The CSF is clearly delineable and exhibits signal values close to zero, which is in agreement with the expected negligible amounts of proteins therein. Furthermore, a slight contrast between GM and WM structures is apparent, with higher signal values in WM. Interestingly, the GM of the putamen was detected consistently as a hyperintense region across all relevant slices. Additional implementation of the weighted acquisition resulted in further improvement of the image quality (SNR gain of $33 \pm 10\%$) with an overall smoother dualCEST contrast and a clearly defined putamen (Figure 2E). The optimization resulted in an overall SNR gain of approximately a factor of 8 (Figure 2F).

Specificity to proteins of the optimized protocol was investigated in model solutions containing three different compounds associated with the main contributors to the in vivo Z-spectrum: proteins (represented by BSA), metabolites (represented by carnosine, creatine, and glutamate), and ssMT (represented by HC). The low power Z-spectra with $B_1 = 0.7 \mu\text{T}$ (Figure 3A and 3B) exhibit CEST signals in the spectral range of ± 15 ppm for BSA and -1 ppm to $+8$ ppm for the metabolites. In addition, the metabolite sample has a distinct resonance around $\Delta\omega = 3.5$ ppm, which can be assigned to the APT signal of carnosine. The Z-spectrum of HC (Figure 3B, blue line) exhibits a very broad ssMT extending up to ± 200 ppm. The asymmetry reported at higher field strengths¹⁹ was not observable, potentially due to the significantly lower spectral resolution at 3 T, as well as different saturation parameters. In the conventional APT_w images (Figure 3C), this negligible asymmetry of the ssMT resulted in values close to zero, whereas the protein compartment is clearly visible. As expected, the metabolite solution exhibits a signal of comparable amplitude, preventing an unambiguous assignment of the APT_w contrast to proteins. In contrast, dualCEST-MRI (Figure 3D) shows only a signal in the BSA compartment with values close to zero everywhere else, confirming the specificity of the optimized acquisition protocol to proteins.

3.2 | Test-retest reliability in healthy volunteers

The intra- and inter-session repeatability of dualCEST was investigated by examining one subject twice on two different days. The acquired contrasts (Figure 4A–4D) were in very good agreement, with consistent contrast of GM and WM structures, as well as a clearly delineable CSF. However, in comparison with the first in vivo measurement (Figure 2), a slightly different contrast behavior can be observed, mainly visible as a hyperintensity in the frontal WM. In contrast, the amplitude of the dualCEST signal in deep GM (i.e. putamen) is consistent and the occipital GM-WM contrast is quite similar. Possible explanations could be an actual physiological variation between the two different subjects or an overcompensation of B_1 inhomogeneities in the frontal WM. Furthermore, small differences in image quality (particularly Figure 4A) and contrast amplitude are visible between the four scans for the repeatability assessment. The corresponding Bland-Altman analyses of mean values obtained in a

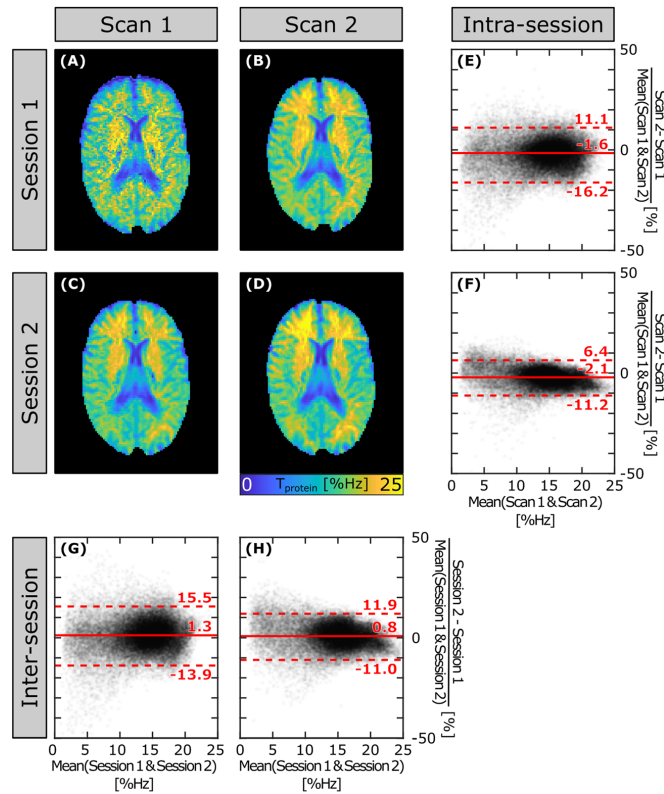


FIGURE 4 The repeatability of the technique is visualized by co-registered dualCEST images (Slice 6 of 12) of a healthy volunteer acquired in two different sessions with two different scans each (A-D). The corresponding Bland-Altman plots show the intra- (E, F) and inter-session (G, H) repeatabilities. For the plots, the mean values of $3 \times 3 \times 1$ regions are used to compute the relative differences between the two measurements as well as the associated bias (solid line) and LOA (broken lines)

$3 \times 3 \times 1$ region (Figure 4E-4H) give similar results for intra- and inter-session comparisons. The corresponding bias and LOA are plotted as relative values as there was a clearly visible correlation between their absolute differences and their mean. In addition, plots involving the noisier first scan of the first session (Figure 1A) exhibit a notably stronger scattering. Overall, the relative differences are small, with a bias close to zero ($\pm 2\%$) and a maximal LOA of approximately $\pm 16\%$. The LOA is an estimate of the threshold for the reliable detectability of signal differences across multiple scans and sessions. In other words, signal changes larger than 16% in a region of $3 \times 3 \times 1$ voxels can be detected reliably. This result is further supported by the corresponding ICCs (Table 1), which indicate a good inter-session and good-to-excellent intra-session and overall reliability of the optimized dualCEST-MRI protocol.

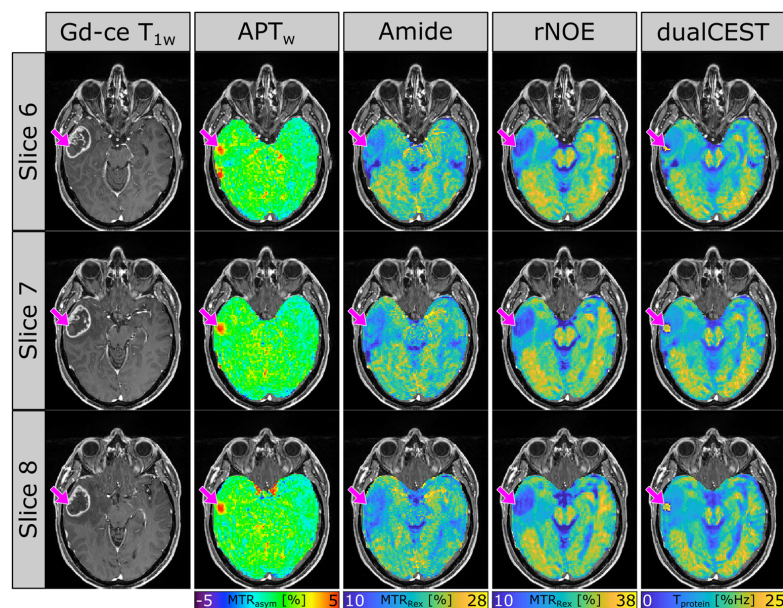
3.3 | Patient measurement

Applicability of the proposed dualCEST acquisition protocol in a clinical setting was demonstrated by examining a patient with newly diagnosed and histopathologically proven glioblastoma (WHO grade IV) (Figure 5). The optimized dualCEST-MRI allows clear delineation of the tumor region

TABLE 1 ICCs and corresponding reliability for dualCEST examinations using the mean of $3 \times 3 \times 1$ regions as input

	Intraclass correlation	95% confidence interval		Indicated reliability ⁴¹
		Lower bound	Upper bound	
Intra-session	0.918	0.875	0.943	Good to excellent
Inter-session	0.895	0.890	0.899	Good
Overall	0.902	0.888	0.913	Good to excellent

FIGURE 5 DualCEST-MRI examination (Slices 6–8 of 12) of a patient with newly diagnosed and histopathologically proven glioblastoma (WHO grade IV) examined at $B_0 = 3$ T. For comparison, conventional APT_w and relaxation-compensated CEST (amide and rNOE) contrasts are illustrated. The tumor volume can be identified in the gadolinium contrast-enhanced T_1 -weighted MR image (Gd-ce T_{1w}). The dualCEST contrast exhibits an artefact (pink arrow), which most likely coincides with a blood clot within the tumor and is also visible as a hyperintense region in the other CEST modalities



by the significantly reduced T_{protein} signal compared with the contralateral side. The healthy tissue exhibits a similar contrast between WM and GM structures as observed in the two volunteers (cf. Figures 3, 4 and 5). A strong hyperintense region was observed in the dualCEST images (Figure 5, pink arrows), which most likely coincides with a blood clot within the tumor. However, these strongly elevated signals are an artefact, which can be traced back to a malfunctioning of the ssMT correction (Equation (2)). This error is caused by the lack of ssMT and resulting T ($\Delta\omega_{\text{ssMT}}$, $-\Delta\omega_{\text{ssMT}}$) values close to or even below zero. However, identification and subsequent exclusion of the affected voxels is straightforward. Interestingly, this region is also discernible in the other CEST modalities, particularly in APT_w images. In general, the dualCEST contrast bears a close resemblance to the rNOE contrast based on the MTR_{Relax} evaluation. The slight differences in the tumor region or the generally less pronounced WM and GM contrast might be of particular interest, as they potentially indicate additional information. A conclusive interpretation of the contrast changes with respect to the clinical relevance and diagnostic value of dualCEST will have to be made in further studies involving a sufficiently large patient cohort.

4 | DISCUSSION

In this study, we optimized the acquisition protocol for dualCEST-MRI at 3 T to enable clinically relevant examinations of the human brain, including changes in the presaturation, image readout, and post-processing of the technique. A first dualCEST proof-of-concept in vivo examination has already been conducted at 3 T.²⁴ However, the inherently low SNR of the dualCEST approach has led to a comparatively long measurement time for the acquisition of sufficiently good images, preventing its application in clinical trials. The optimization presented in this study allowed the reduction of number of averages from 18 to 10, which resulted in an approximately two times shorter imaging protocol, with an increased resolution by a factor of two (now $1.7 \times 1.7 \times 3$ mm³ compared with $1.9 \times 1.9 \times 5$ mm³). Additionally, this increased image quality no longer necessitates Gaussian smoothing. The overall acquisition duration of the proposed protocol—consisting of the dualCEST scan, as well as B_1 and T_1 mapping to correct for field inhomogeneities and water relaxation properties—is 20 min, which is comparable to the acquisition of relaxation-compensated CEST contrasts.^{7,33}

The optimization comprised implementation of (i) a simultaneous dual-frequency presaturation, (ii) a weighted acquisition scheme, (iii) a 3D image acquisition enabling retrospective motion correction, and (iv) application of advanced denoising strategies. An SNR analysis across multiple tissue regions revealed that the latter two steps contributed most to the achieved improvement. In contrast to most of the conventional CEST modalities, for the registration of dualCEST image data no specialized motion correction is required as no fully saturated images are acquired at the direct water saturation ($\Delta\omega = 0$ ppm), which otherwise potentially yield artifacts.⁴² In addition to the resulting SNR gain, motion correction is an essential prerequisite for the subsequent denoising.³² Application of the denoising algorithm resulted in a tremendous improvement in image quality.

The utilized algorithm combines principal component analysis with an appropriate data-driven criterion to differentiate meaningful spectral features from noise-like characteristics to avoid the potential risk of excessive denoising.³² For the in vivo data the criterion consistently determined six components to be optimal, which seems adequate compared with the maximally possible nine degrees of freedom (i.e. frequency offset pairs).

In comparison to the post-processing steps, the implementation of the cosine-modulated pulses and the weighted acquisition scheme resulted in only a minor improvement. Based on the previous investigations, the effectively doubled DC of a simultaneous presaturation was expected to result in a substantially more efficient saturation and thereby improved image quality. However, usage of the cosine-modulated pulses resulted in only an insignificant SNR gain. This can be explained by the Z-values for an increased DC being smaller and closer to the noise level, counteracting the potential gain by the increased DC. Furthermore, this approach required shifting the frequency offsets to exclude the possibility of unintentional direct water saturation by the residual carrier leakage (Figure 1C). Due to the comparatively broad dualCEST resonances at 3 T, this frequency shift does not impair the specificity of the approach. However, in the presence of large B_0 inhomogeneities (i.e. $|\Delta B_0| \geq 0.5$ ppm) the shifted frequency offsets might result in an off-resonant saturation. To avoid the susceptibility to large B_0 inhomogeneities resulting from the frequency shift, parallel transmission systems⁴³ could be used to achieve a simultaneous dual-frequency irradiation without residual carrier frequency leakage (Figure 1C). Alternatively, a more robust acquisition protocol could be realized by using the conventional alternating presaturation without a significant loss in SNR. In contrast to the cosine-modulated pulses, application of the weighted acquisition scheme for averaging the frequency offset pairs resulted in a small but significant SNR increase. This was achieved by adjusting the averaging according to the anticipated effect of the Z-values on the final contrast (see Section 2.1.3). In the future, the model could be extended by using the actual Rician⁴⁴ error distribution instead of a Gaussian distribution, which would avoid the assumption of the error being independent of the signal value. Nonetheless, the distribution obtained in this study is a good first approximation, yielding improved image quality compared with previous uniform averaging.

Reproducibility was investigated by repeating in vivo measurements with the optimized dualCEST-MRI protocol. Respective mean values in regions of $3 \times 3 \times 1$ voxels were compared during data assessment (Bland-Altman analyses and ICC). More meaningful results are obtained using $3 \times 3 \times 1$ voxels than single voxels, as the spatial information of the image is taken into account (i.e. surrounding voxels). In contrast to using only a single region of interest (e.g. a whole organ or tissue),^{45,46} this "fixed window" approach allowed for a larger sample size for the statistical analyses. It should be kept in mind that in doing so the following assessment results are only valid for evaluating regions of $3 \times 3 \times 1$ voxels. Even better repeatability and sensitivity can be expected for a potential diagnostic application assessing larger regions of interest. As expected, repeatability (ICC and LOA) is lower for inter- compared with intra-session measurements. However, these marginal differences indicate that deviations due to repositioning and resulting partial volume effects are quite small. The repeatability of CEST-MRI has so far only been evaluated in a few studies with widely varying evaluation standards and in different entities.⁴⁵⁻⁴⁸ In the brain, repeatability was only evaluated using the less informative coefficient of variation, which could not be assessed in this study as there were only two repetitions for the intra- and inter-session evaluation. Therefore, we resorted to comparing our results in the brain with breast and prostate imaging, which are however intrinsically more difficult to reproduce due to e.g. increased B_0 inhomogeneities and additional non-rigid motion. ICC values were reported as 0.963 (95% confidence interval 0.852, 0.991)⁴⁵ for conventional APT-CEST in the breast and as 33-38% LOA for conventional APT- and rNOE-CEST in the prostate.⁴⁶ In comparison with the values in this study (ICC = 0.902 with a 95% confidence interval of 0.888, 0.913; LOA = 16%), the reliability of dualCEST is equal or even better. Furthermore, the obtained LOA of 16% is a threshold estimate for identifying signal differences caused by genuine biophysical effects. However, the diagnostic value will ultimately depend on the actual magnitude of change in pathologies which must be assessed in future clinical studies. For example, a recent study on mice with Alzheimer's disease revealed conventional CEST signal changes attributed to proteins to be of the order of 20%.¹⁹ The exceptional specificity of dualCEST to proteins might allow the isolation of signal changes from other confounding influences and thus result in an even larger observable effect.

This acquisition protocol enables the application of dualCEST-MRI in a clinical setting. The significant signal decrease in the tumor region (approximately 35% compared with contralateral normal appearing WM) of a patient with glioblastoma (Figure 5) is in line with results of the previous proof-of-concept examination.²⁴ In comparison to this previous examination,²⁴ a superior image quality and resolution was achieved. In addition, the specificity of the dualCEST approach was preserved in the optimized protocol (Figure 3), meaning that the signal decrease in the tumor region can be attributed to a pathological modification of mobile proteins (i.e. changes in the concentration, folding state, or molecular size).²⁴ With regard to protein content assessment, the dualCEST signal is a measure of the relative protein content and therefore depends on the apparent water content.⁴⁹ This is an unsolved issue in the research field of CEST-MRI in general and holds true for all exchange mediated methods measuring solutes indirectly via the water signal. Therefore, part of the observable contrast between GM, WM, and tumor could be attributed to differences in the water content. Assessment of absolute protein content is in principle possible by a correction of the water content, which can be quantified by established techniques based on for example T_2^* and T_1 measurements.⁵⁰ The achieved specificity of the dualCEST approach could be utilized as a reference to assess the assignment of conventional amide and rNOE CEST signals to proteins. Discrepancies revealed by comparing different approaches would indicate confounding contributions (i.e. metabolites or lipids) or physiological dependencies (i.e. pH). In doing so, dualCEST may lead to novel insights into the origin of protein CEST contrasts in vivo. In the future, clinical studies with larger patient cohorts need to be examined to assess the diagnostic value of dualCEST-MRI, particularly the potential of the dualCEST contrast as a biomarker for neurodegenerative diseases or cancer.

5 | CONCLUSIONS

In this study, we developed an acquisition protocol for dualCEST-MRI at 3 T to enable selective imaging of endogenous bulk mobile proteins under clinically relevant conditions. This goal was achieved by extending the image readout to 3D, allowing for retrospective motion correction and application of denoising strategies. Furthermore, a simultaneous dual-frequency presaturation was implemented and combined with a weighted acquisition scheme. Preservation of specificity was demonstrated *in vitro*. Repeated *in vivo* examinations indicated good-to-excellent reliability and allowed estimation of a threshold to distinguish genuine biophysical effects from measurement noise. Applicability in a clinical setting was demonstrated by examining a patient with glioblastoma, revealing significant alterations of the dualCEST contrast in the tumor region. This optimized protocol enables examination of larger patient cohorts, and thus assessment of the diagnostic value of dualCEST-MRI.

ACKNOWLEDGEMENTS

The financial support of the German Research Foundation (DFG; GO 2172/1-1) is gratefully acknowledged. In addition, we cordially thank Dr Rachel A. High from the University of California, San Diego, for her diligent language editing of the manuscript and Dominik Ludwig from the German Cancer Research Center for his assistance in the phantom preparation.

CONFLICTS OF INTEREST

The authors declare no conflict of interest.

ORCID

Johannes Breitling  <https://orcid.org/0000-0001-8003-5382>

Moritz Zaiss  <https://orcid.org/0000-0001-9780-3616>

Daniel Paech  <https://orcid.org/0000-0001-5755-6833>

Steffen Goerke  <https://orcid.org/0000-0002-0684-2423>

REFERENCES

1. Forsén S, Hoffman RA. Study of moderately rapid chemical exchange reactions by means of nuclear magnetic double resonance. *J Chem Phys*. 1963; 39(11):2892-2901.
2. Ward K, Aletras A, Balaban R. A new class of contrast agents for MRI based on proton chemical exchange dependent saturation transfer (CEST). *J Magn Reson*. 2000;143(1):79-87.
3. McMahon MT, Gilad AA, Bulte JWM, van Zijl PCM. *Chemical Exchange Saturation Transfer Imaging: Advances And Applications*. 1st ed. Singapore: Pan Stanford; 2017.
4. Zhou J, Payen J-F, Wilson DA, Traystman RJ, van Zijl PCM. Using the amide proton signals of intracellular proteins and peptides to detect pH effects in MRI. *Nat Med*. 2003;9(8):1085-1090.
5. Yan K, Fu Z, Yang C, et al. Assessing amide proton transfer (APT) MRI contrast origins in 9 L gliosarcoma in the rat brain using proteomic analysis. *Mol Imaging Biol*. 2015;17(4):479-487.
6. Jones CK, Huang A, Xu J, et al. Nuclear Overhauser enhancement (NOE) imaging in the human brain at 7 T. *Neuroimage*. 2013;77:114-124.
7. Zaiss M, Windschuh J, Paech D, et al. Relaxation-compensated CEST-MRI of the human brain at 7 T: unbiased insight into NOE and amide signal changes in human glioblastoma. *Neuroimage*. 2015;112:180-188.
8. Chan KWY, McMahon MT, Kato Y, et al. Natural D-glucose as a biodegradable MRI contrast agent for detecting cancer. *Magn Reson Med*. 2012;68(6): 1764-1773.
9. Haris M, Nanga RPR, Singh A, et al. Exchange rates of creatine kinase metabolites: feasibility of imaging creatine by chemical exchange saturation transfer MRI. *NMR Biomed*. 2012;25(11):1305-1309.
10. Cai K, Haris M, Singh A, et al. Magnetic resonance imaging of glutamate. *Nat Med*. 2012;18(2):302-306.
11. Jones CK, Schlosser MJ, van Zijl PCM, Pomper MG, Golay X, Zhou J. Amide proton transfer imaging of human brain tumors at 3T. *Magn Reson Med*. 2006;56(3):585-592.
12. Wen Z, Hu S, Huang F, et al. MR imaging of high-grade brain tumors using endogenous protein and peptide-based contrast. *Neuroimage*. 2010;51(2): 616-622.
13. Togao O, Yoshiura T, Keupp J, et al. Amide proton transfer imaging of adult diffuse gliomas: correlation with histopathological grades. *Neuro Oncol*. 2014;16(3):441-448.
14. Takayama Y, Nishie A, Togao O, et al. Amide proton transfer MR imaging of endometrioid endometrial adenocarcinoma: association with histologic grade. *Radiology*. 2018;286(3):909-917.
15. Zhou J, Tryggstad E, Wen Z, et al. Differentiation between glioma and radiation necrosis using molecular magnetic resonance imaging of endogenous proteins and peptides. *Nat Med*. 2011;17(1):130-134.
16. Mehrabian H, Desmond KL, Soliman H, Sahgal A, Stanisz GJ. Differentiation between radiation necrosis and tumor progression using chemical exchange saturation transfer. *Clin Cancer Res*. 2017;23(14):3667-3675.
17. Meissner J-E, Korzowski A, Regnery S, et al. Early response assessment of glioma patients to definitive chemoradiotherapy using chemical exchange saturation transfer imaging at 7 T. *J Magn Reson Imaging*. 2019;50(4):1268-1277. <https://doi.org/10.1002/jmri.26702>
18. Wang R, Li S-Y, Chen M, et al. Amide proton transfer magnetic resonance imaging of Alzheimers Disease at 3.0 Tesla. *Chin Med J (Engl)*. 2015;128(5): 615-619.

19. Chen L, Wei Z, Chan KWY, et al. Protein aggregation linked to Alzheimer's disease revealed by saturation transfer MRI. *Neuroimage*. 2019;188:380-390.
20. Li C, Peng S, Wang R, et al. Chemical exchange saturation transfer MR imaging of Parkinson's disease at 3 Tesla. *Eur Radiol*. 2014;24(10):2631-2639.
21. Dula AN, Asche EM, Landman BA, et al. Development of chemical exchange saturation transfer at 7T. *Magn Reson Med*. 2011;66(3):831-838.
22. Goerke S, Zaiss M, Bachert P. Characterization of creatine guanidinium proton exchange by water-exchange (WEX) spectroscopy for absolute-pH CEST imaging *in vitro*. *NMR Biomed*. 2014;27(5):507-518.
23. Liepinsh E, Otting G. Proton exchange rates from amino acid side chains—implications for image contrast. *Magn Reson Med*. 1996;35(1):30-42.
24. Goerke S, Breitling J, Zaiss M, et al. Dual-frequency irradiation CEST-MRI of endogenous bulk mobile proteins. *NMR Biomed*. 2018;31(6):e3920.
25. Vallurupalli P, Tiwari VP, Ghosh S. A double-resonance CEST experiment to study multistate protein conformational exchange: an application to protein folding. *J Phys Chem Lett*. 2019;10(11):3051-3056.
26. Zaiss M, Bachert P. Exchange-dependent relaxation in the rotating frame for slow and intermediate exchange—modeling off-resonant spin-lock and chemical exchange saturation transfer. *NMR Biomed*. 2013;26(5):507-518.
27. Goerke S, Zaiss M, Kunz P, et al. Signature of protein unfolding in chemical exchange saturation transfer imaging. *NMR Biomed*. 2015;28(7):906-913.
28. Goerke S, Milde KS, Bukowiecki R, et al. Aggregation-induced changes in the chemical exchange saturation transfer (CEST) signals of proteins. *NMR Biomed*. 2017;30(1):e3665.
29. Lee J-S, Khitrin AK, Regatte RR, Jerschow A. Uniform saturation of a strongly coupled spin system by two-frequency irradiation. *J Chem Phys*. 2011;134(23):234504.
30. Prevost VH, Girard OM, Mchinda S, Varma G, Alsop DC, Duhamel G. Optimization of inhomogeneous magnetization transfer (IhMT) MRI contrast for preclinical studies using dipolar relaxation time ($T_{1\rho}$) filtering. *NMR Biomed*. 2017;30(6):e3706.
31. Zaiss M, Ehse P, Scheffler K. Snapshot-CEST: optimizing spiral-centric-reordered gradient echo acquisition for fast and robust 3D CEST MRI at 9.4 T. *NMR Biomed*. 2018;31(4):e3879.
32. Breitling J, Deshmane A, Goerke S, et al. Adaptive denoising for chemical exchange saturation transfer MR imaging. *NMR Biomed*. 2019;32(11):e4133.
33. Goerke S, Soehngen Y, Deshmane A, et al. Relaxation-compensated APT and rNOE CEST-MRI of human brain tumors at 3 T. *Magn Reson Med*. 2019;82(2):622-632.
34. Varma G, Duhamel G, de Bazelaire C, Alsop DC. Magnetization transfer from inhomogeneously broadened lines: a potential marker for myelin. *Magn Reson Med*. 2015;73(2):614-622.
35. Nolden M, Zelzer S, Seitel A, et al. The Medical Imaging Interaction Toolkit: challenges and advances. *Int J Comput Assist Radiol Surg*. 2013;8(4):607-620.
36. Flocq R. Matchpoint: on bridging the innovation gap between algorithmic research and clinical use in image registration. *IFMBE Proc*. 2009;25:1105-1108.
37. Schuenke P, Windschuh J, Roeloffs V, Ladd ME, Bachert P, Zaiss M. Simultaneous mapping of water shift and B_1 (WASABI)—application to field-inhomogeneity correction of CESTMRI data. *Magn Reson Med*. 2017;77(2):571-580.
38. Windschuh J, Zaiss M, Meissner J-E, et al. Correction of B_1 -inhomogeneities for relaxation-compensated CEST imaging at 7 T. *NMR Biomed*. 2015;28(5):529-537.
39. Zhou J, Heo H-Y, Knutsson L, van Zijl PCM, Jiang S. APT-weighted MRI: techniques, current neuro applications, and challenging issues. *J Magn Reson Imaging*. 2019;50(2):347-364.
40. Bland JM, Altman DG. Statistical methods for assessing agreement between two methods of clinical measurement. *Lancet*. 1986;327(8476):307-310.
41. Koo TK, Li MY. A guideline of selecting and reporting intraclass correlation coefficients for reliability research. *J Chiropr Med*. 2016;15(2):155-163.
42. Wech T, Köstler H. Robust motion correction in CEST imaging exploiting low-rank approximation of the z-spectrum. *Magn Reson Med*. 2018;80(5):1979-1988.
43. Katscher U, Börner P. Parallel RF transmission in MRI. *NMR Biomed*. 2006;19(3):393-400.
44. Gudbjartsson H, Patz S. The Rician distribution of noisy MRI data. *Magn Reson Med*. 1995;34(6):910-914.
45. Dula AN, Dewey BE, Arlinghaus LR, et al. Optimization Of 7-T chemical exchange saturation transfer parameters for validation of glycosaminoglycan and amide proton transfer of fibroglandular breast tissue. *Radiology*. 2015;275(1):255-261.
46. Evans VS, Torrealdea F, Rega M, et al. Optimization and repeatability of multipool chemical exchange saturation transfer MRI of the prostate at 3.0 T. *J Magn Reson Imaging*. 2019;50(4):1238-1250.
47. Nanga RPR, DeBrosse C, Kumar D, et al. Reproducibility of 2DGluCEST in healthy human volunteers at 7 T. *Magn Reson Med*. 2018;80(5):2033-2039.
48. Yuan J, Chen S, King AD, et al. Amide proton transfer-weighted imaging of the head and neck at 3 T: a feasibility study on healthy human subjects and patients with head and neck cancer. *NMR Biomed*. 2014;27(10):1239-1247.
49. Lee D-H, Heo H-Y, Zhang K, et al. Quantitative assessment of the effects of water proton concentration and water T_1 changes on amide proton transfer (APT) and nuclear Overhauser enhancement (NOE) MRI: the origin of the APT imaging signal in brain tumor. *Magn Reson Med*. 2017;77(2):855-863.
50. Neeb H, Zilles K, Shah NJ. A new method for fast quantitative mapping of absolute water content *in vivo*. *Neuroimage*. 2006;31(3):1156-1168.

SUPPORTING INFORMATION

Additional supporting information may be found online in the Supporting Information section at the end of this article.

How to cite this article: Breitling J, Meissner J-E, Zaiss M, et al. Optimized dualCEST-MRI for imaging of endogenous bulk mobile proteins in the human brain. *NMR in Biomedicine*. 2020;33:e4262. <https://doi.org/10.1002/nbm.4262>

3 Discussion

The non-invasive imaging of protein-attributed CEST signals has been shown to provide biochemical insights *in vivo*, which have been shown to be correlated to clinically relevant information for a variety of diseases. While conventional CEST imaging modalities suffer from confounding signals of metabolites and macromolecules, the novel approach of dualCEST enables increased protein specificity by selectively detecting the intramolecular spin diffusion. However, its application has so far been restricted to spectrometer measurements of model solutions at ultra-high magnetic field strengths. The aim of this thesis was therefore the translation of the dualCEST technique from a spectrometer application to a clinical whole-body MR scanner to enable, for the first time, examinations of the human brain.

3.1 Translation from NMR spectrometer to clinical scanner

This translation required, among other things, extending the technique from a spectroscopic approach to an imaging modality and addressing the considerably smaller SNR of the lower magnetic field strength, while at the same time meeting clinical needs in terms of practicability, reproducibility, and imaging speed. In order to achieve these objectives, several methodological developments were utilized, covering all parts of the technique: signal preparation, imaging readout, and post-processing.

Impact of clinical magnetic field strength

In general, the transfer of CEST approaches to lower magnetic field strengths is complicated by the entailing decrease in the spectral resolution and resulting incapability to resolve individual and distinct peaks. In contrast, for dualCEST this limitation can be bypassed by its novel dimension of selectivity. Using the coupling of different CEST signals as a distinguishing feature, rather than the resolution and isolation of the individual resonances, enables a straightforward application at clinical magnetic field strengths. Moreover, the dualCEST technique actually benefits from the decrease in spectral resolution. In proteins, the chemical shift of identical protons is dispersed depending on their location in the molecule and the surrounding chemical environment.⁸⁰ A decrease in the magnetic field strength results in a spectral broadening of the presaturation pulses. As a result, more protons from neighboring chemical shifts are incorporated into the measurement procedure, yielding a larger signal. With regard to the occurrence of B_0 -inhomogeneities, the comparatively broad plateau

of the dualCEST resonance at 3 T allows the omission of a correction procedure. Otherwise, a time-consuming acquisition of additional frequency offset combinations would be required. In view of those factors, the dualCEST technique seems suited for application at clinical magnetic field strengths. However, the concomitant and considerable SNR decrease ($SNR \propto B_0^{1.65}$)⁸¹ becomes problematic in combination with the already inherently low SNR of dualCEST. The latter can be attributed to the complex calculation of the final contrast (Chapter 1, equations 7 and 8) and consequent error propagation for nine error-containing signal values. The improvement of SNR was therefore paramount for all subsequent decisions and further developments.

Presaturation

For optimizing the presaturation parameters, the aforementioned novel dimension of selectivity and the beneficial spectral broadening of the presaturation pulses can be further exploited. Firstly, the signal strength can be increased by applying presaturation pulses with a shorter duration t_p (Publication I, figure 3E and F). In a similar manner to the decrease in the magnetic field strength, the resulting increase of the spectral bandwidth results in a larger number of saturated protons. Secondly, as dualCEST is only relying on the coupling of CEST signals, this allows the application of high B_1 amplitudes to increase the signal strength without any loss in the specificity. This is in strong contrast to conventional CEST approaches, where the extensive peak broadening for high B_1 amplitudes results in an undesirable deterioration of the spectral selectivity.⁸² However, it should be noted that even for dualCEST, an excessive broadening of signals is possible, resulting in an erroneous signal quantification. This erroneous signal quantification is the case if the resulting linewidths are larger than the distance between the two frequency offsets $\Delta\omega$ and $\Delta\omega_c$. In other words, a direct saturation of CEST signals at one frequency offset induces pulses applied to the other. Nevertheless, the utilized spacing of $|\Delta\omega - \Delta\omega_c| \geq 10$ ppm should be sufficient to avoid such influences, while at the same time allowing for a broad range of possible B_1 amplitudes and pulse lengths. With these specifications, the presaturation parameters in this study were optimized to maximize the dualCEST signal while avoiding an excessive broadening of the resonances. For the determined optimal parameters ($t_p = 20$ ms, $B_1 = 2$ μ T) the dualCEST signal is in addition approximately linear as a function of B_1 , which enables a straightforward correction of the B_1 -inhomogeneities encountered in vivo.⁸³

In a next step, as part of Publication IV, the presaturation was further developed by introducing dual-frequency pulses. The previous implementations of the dualCEST technique utilized a train of Gaussian-shaped pulses to alternately saturate the two different frequency offsets (Figure 2A). However, as only every second pulse is effectively saturating the same frequency offset, such an alternating pulse scheme is inefficient. Modulating the employed Gaussian-shaped RF pulses with a cosine function allows for the simultaneous saturation of both frequency offsets,^{77,78} thereby effectively increasing the duty cycle by a factor of two. Based on the previous investigations of the duty cycle dependence,^{32,33} a considerably more efficient saturation, and thus increase in SNR, was expected. However, usage of the

cosine-modulated pulses resulted in only an insignificant gain. This lack of improvement could potentially be explained by the acquired Z -values of this more efficient saturation being smaller while the signal noise of the image itself remains constant. Hence, the Z -values' relative error actually increases. As a result, a higher dualCEST contrast value might be observed in the end, however, the corresponding error would increase even more and nullify any SNR gain. For future applications, it should therefore be investigated whether a less efficient saturation is actually beneficial for the SNR. In this context, a simultaneous saturation using a decreased B_1 amplitude – as opposed to the previous alternating scheme with high B_1 – is preferable as it allows the same saturation efficiency to be achieved but without any unnecessary signal broadening.

It should be noted that the implementation of the simultaneous saturation using the cosine-modulated pulses comes at the disadvantage of requiring the intended frequency offsets to be shifted to exclude a potential direct water saturation. Imperfections of the cosine modulation, e.g. due to the finite number of digitized steps per pulse, result in addition to small deviations in a residual carrier leakage. For a pair of frequency offsets positioned symmetrically around the water resonance $\Delta\omega = 0$ ppm, this residual carrier leakage will result in an unintentional direct water saturation. To avoid this effect, slightly asymmetric frequency offsets had to be utilized. Due to the comparatively broad plateau of the dualCEST resonance, this adaption does not impair the specificity of the dualCEST signal. However, in combination with the occurrence of severe B_0 -inhomogeneities (i.e. $|\Delta B_0| \geq 0.5$ ppm) the shifted frequency offsets could potentially result in the saturation being off-resonant. To avoid the necessity of shifting frequency offsets and the entailing susceptibility to large B_0 -inhomogeneities altogether, parallel transmission systems^{84–86} could be used to achieve simultaneous saturation without residual carrier frequency leakage. For this purpose, the alternating dual-frequency irradiation would be applied to the different coil elements with adjacent channels having the opposite order of frequency offset.

Imaging readout and acquisition scheme

In general, the right choice of signal acquisition is – besides the details of the presaturation – of the uttermost importance for CEST imaging. The immediately commencing decay of the prepared signal towards the equilibrium magnetization necessitates a fast signal acquisition to minimize any contrast loss. For dualCEST, the extension from a spectroscopic approach to an imaging modality was first achieved by combining the presaturation module with an established 2D gradient echo pulse sequence with a centric reordered k -space acquisition.^{13,87} In this context, gradient echo-based approaches offer a particularly high robustness in addition to a sufficiently fast imaging speed. Moreover, the centric reordering of k -space, which samples the crucial central data points first, allows for an efficient acquisition of the contrast generated by the presaturation phase.

As a next step, the subsequent extension of the image readout to 3D facilitated both coverage of a larger volume and the possibility to apply retrospective motion correction algorithms.

However, the straightforward solution of a sequential multi-slice approach was not feasible. This would otherwise have resulted in a significantly deteriorated contrast due to the longer acquisition time and simultaneous decay of the prepared signal. Consequently, the dualCEST preparation was combined with the sophisticated imaging readout of the recently published snapshot-CEST approach.⁷¹ The centric-spiral sampling of the k-space of this approach allows a 3D volume to be acquired in a single-shot with tolerable contrast loss. The snapshot-CEST sequence has many parameters that affect the image quality and acquisition duration. The influence of the main parameters (GRAPPA acceleration factor and bandwidth) were investigated and optimized in Publication II. As a result, it was possible to maximize the acquired 3D volume and the SNR, while at the same time minimizing the acquisition time and thus preserving the contrast.

An additional small but significant SNR increase was achieved by developing and implementing a weighted acquisition scheme. As dualCEST-MRI still requires multiple averages to accumulate enough SNR, the distribution of the number of averages spent per frequency offset pair is as well an optimizable parameter. The idea behind this method is that certain frequency offset pairs will have a larger impact on the final contrast quality than others. Essentially, the acquired Z-values have different amplitudes, thus different relative errors, and are used in different places in the equations. The aim is therefore to average the high-impact Z-values more often to ultimately reduce the error of the final contrast for a fixed number of repetitions. In this way, adjustment of the averaging scheme to the anticipated effect of the Z-values allowed an SNR gain of 33%. Application of this approach is straightforward and does not necessitate any complicated changes to the sequence. Nevertheless, this implementation is only a first step and there is still room for improvement. The proposed determination of the optimal distribution assumes uncorrelated and normally distributed errors with a uniform variance, which in most cases does not hold true. As a next step, the model should be extended to incorporate a Rician,⁸⁸ instead of Gaussian, noise distribution, which avoids the assumption of the noise being independent of the actual signal value. To be even more realistic, the noise correlations induced by the utilized parallel imaging should be incorporated as well.⁸⁹ However the latter is not straightforward, as it would rule out an analytical solution and would necessitate a numerical optimization using simulations. Nonetheless, the approach presented here and the obtained distribution are a good first approximation and have already resulted in a significant improvement compared to the previous uniform averaging scheme.

Post-processing

As previously mentioned, the main challenge of this work was the considerable SNR decrease due to the lower field strength in combination with the intrinsically low SNR of the dualCEST technique. In addressing this issue, the development and application of a novel denoising algorithm resulted in the largest improvement compared with all other advancements. The basis for this approach is the application of a PCA, which allows the dimensionality of the data to be reduced while preserving the essence of information. In combination

with an appropriate data-driven approach to determine the crucial number of remaining components, this technique enables an efficient and robust separation of noise-like characteristics from meaningful spectral features.

PCA has previously been reported to be a powerful denoising technique for HyperCEST by Döpfert et al.⁹⁰ However, for these previous attempts the optimal number of necessary components was determined based on prior knowledge about the composition of the imaged phantom. For in vivo data, comprising multiple spectral resonances, the number of necessary components is not a straightforward deduction as the number of contributions as well as their dependence on physiological influences and pathological alterations are unknown. The fact that the number of components is unknown is problematic, as the right number is crucial for the performance of the approach: preservation of too many components will diminish the denoising effect, while too few components will result in unacceptable contrast distortions.

Therefore, in Publication III, the combination of the PCA with several data-driven criteria were examined, which estimate the number of principle components remaining uncontaminated by noise. The performance and validity of the different criteria was investigated for synthetic and in vivo data sets of conventional CEST experiments. Utilization of synthesized data allowed for the comparison with a ground truth, which is necessary for determining the actual optima. The synthesized data was generated from high SNR in vivo CEST spectra, taking into account B_1 inhomogeneities, the spatially variant coil sensitivity profile, and the accurate noise distribution of the utilized GRAPPA reconstruction.⁸⁹ The simulations and in vivo data determined that all three investigated criteria yield robust and reliable results with the denoising capability being comparable or even superior to an averaging of six measurements (i.e. a factor of 2.5). The latest investigations of Appendix A even indicated a remarkable SNR gain by a factor of 3.5 (Figure A.3) by additionally incorporating a correction for the Rician noise induced bias.⁹¹

This approach is in general not limited to the investigated conventional CEST experiment but is applicable to all related approaches providing an additional dimension to exploit redundancies. For dualCEST this is realized by stringing together the individual acquisitions, i.e. the combined dimension of frequency offset pairs and repetitions. In Publication IV, application of the denoising approach to in vivo dualCEST data yielded an SNR increase by a factor of 2.3, which is consistent with the results for the conventional CEST. Moreover, the consistently determined number of six components seems appropriate with regard to the overall possible nine degrees of freedom (i.e. frequency offset pairs), again indicating the general validity of the utilized criterion.

To ensure correct functioning of the denoising approach, adequate preprocessing of the data is essential. Prior segmentation of meaningful tissue (i.e. brain matter and cerebral spinal fluid (CSF)) is required to exclude the distorting influence of voxels dominated by fat, noise, or large vessels. With regard to large vessels, special emphasis should be placed on the sagittal sinus superior, since failing to properly exclude this region has resulted in serious defects on numerous occasions. In addition to the segmentation, a correction for possible movements and deformations during the measurement is crucial to restore the underlying correlations across all voxels. Unaddressed or remaining displacements will result in corrupted spectral

3 Discussion

components and in a higher number of necessary components to describe the data. In this context, the previous extension of the image readout to 3D is vital as it allows correcting for a displacement or tilting of the investigated body region out of the imaging plane. In addition to being an essential prerequisite for the denoising approach, application of the motion correction resulted directly in a significant SNR gain by a factor of 1.9. In comparison to other conventional CEST approaches, registration of dualCEST image data does not require a specialized motion correction as there is no fully saturated image acquired (i.e. with only little image intensity values at the direct water saturation $\Delta\omega = 0$ ppm), which typically results in severe malfunctioning.⁹² Nevertheless, application of such specialized approaches might still be beneficial as the complex calculation of the dualCEST contrast is susceptible to even small remaining displacements, which are then potentially corrected. In the future, the necessity for retrospective motion corrections could be avoided altogether by real-time tracking of the head motion and corresponding adjustment of the position and orientation of the field of view. The necessary sophisticated tracking could be realized by optical markers rigidly attached to the head or additional navigator scans determining the current position shortly before the actual acquisition.^{93,94}

As impressive as the results are, the algorithm presented in Publication III represents only a first introduction of denoising techniques to the field of in vivo CEST, with potential remaining for advancements. For instance, the utilized PCA reduces the data set to solely the correlations between the frequency offsets across all voxels. Any additional information about the spatial as well as tissue interdependencies is thereby lost. To exploit at least the latter to some extent, in Appendix A the PCA was combined with a prior formation of subsets of similar spectra, which most likely originate from tissue with comparable properties. By exploiting only the remaining subtle differences of these subsets – instead of the entire data set – a better identification and isolation of the underlying spectral features is achieved.^{95,96} Application of this extended approach to conventional in vivo CEST data resulted in an additional SNR increase by .114%. Moreover, the selection and subsequent denoising of subsets of similar spectra reduces the risk of spectral features being undesirably distorted or removed altogether. This is particularly important for unique signatures, which are only present in a small area of the acquisition volume, as is usually the case for tumors. In comparison to a simple prior segmentation of the image into different tissue classes (i.e. white matter (WM), gray matter (GM), CSF, etc.) with a subsequent denoising of these compartments, the data-driven grouping of similar spectra avoids a presumptuous classification of aberrant voxels and results in a more diverse and better representation of the spectral features. In the future, a further incorporation of the latent spatial information would be desirable; however, this is not possible on the basis of a simple PCA. For that purpose, more sophisticated approaches would have to be utilized, combining both spatial and spectral information to improve the denoising performance even further.^{96,97}

Further acceleration – an outlook

Altogether, the developments discussed above facilitated the establishment of a dualCEST imaging protocol, which overcame the combined challenges and limitations of the technique itself and the considerably lower magnetic field strength – in particular the inherently low SNR. The resulting overall acquisition time for dualCEST-MRI, including B_1 and T_1 mapping for correcting field inhomogeneities and tissue water relaxation properties, is 20 minutes. This time is on par with conventional relaxation-compensated CEST approaches^{13,98} and allowed this technique to be used in pilot studies investigating its diagnostic value. The results of these pilot studies are discussed in the last section. The future long-term objective for dualCEST should not only be its applicability in studies, but also in clinical routine, which means even stricter requirements for the acquisition time and a resulting necessity to accelerate the approach even further.

An acceleration of dualCEST-MRI can in principle be realized in two ways: by increasing the SNR of each repetition to reduce the necessary number of averages, or by shortening the time for one repetition. Possible methods for the former have already been mentioned in the respective parts of this chapter, i.e. advanced denoising strategies and utilization of parallel transmission systems for the presaturation, and will therefore not be discussed in more detail here. With regard to a reduction of the repetition time, shortening the presaturation phase would be of particularly impactful, as it represents a long waiting period, which accounts currently for 60% of the total examination duration. The necessity for this long saturation time arises from the fact that dualCEST requires, as do most other quantitative techniques, a saturation time in the order of 3-5 times T_1 to reach the steady-state condition.⁴⁵

In Appendix B, a method for (conventional) CEST approaches is presented, which allows this time-consuming problem to be avoided by calculating the steady-state signal from an experiment with a significantly reduced saturation period. In order to achieve this reduced saturation period, the analytical description of the signal evolution (Equation 3) is solved for the steady-state signal, which as a result can then be determined from data acquired with an arbitrary saturation time. In other words, the method is a fairly accurate extrapolation of the accelerated data based on the analytical model of the signal evolution. Two important things can already be deduced from this fact: the extrapolation will only be as accurate as the underlying model, and the further the extrapolation is (i.e. for very short saturation times), the worse the results will be. The final calculation (Equation B.3) requires multiple quantities to be determined: the dualCEST measurement with a shortened presaturation period, B_0 -, B_1 - and T_1 -maps (usually already acquired, as they are required for dualCEST) and a calibration measurement with the dualCEST sequence parameters. The only additional measurement is the calibration, which does not require too much extra time. An acceleration of the imaging protocol is thus achieved as soon as the time, saved by the reduction of the presaturation, outweighs the additional expenditure of the calibration measurement, which is given for almost all experimental setups.

For conventional CEST experiments this method was shown to be able to provide a very close approximation of the steady-state Z-spectra using a presaturation period in the order

of one-time T_1 (Figures B.2 and B.3). The discrepancies in the solid components of the brain were limited to only small deviations for GM in the Z-spectrum region of the rNOE; however, rather considerable differences were observable in the CSF. The first observation is potentially explainable by the rather slow exchange rate of the rNOE (approximately 5 Hz)⁹⁹ in combination with the longer T_1 of GM. Within this limit, the underlying assumption of a mono-exponential decay does not hold anymore and additional rotational effects and exchange processes in the pauses would have to be considered.¹⁰⁰ To avoid this problem as much as possible, long pulses, if not even a continuous saturation, should be used with a saturation time that is at least one-time T_1 of the 'slowest' tissue of interest. The deviations in CSF can be understood in terms of partial volume effects, which prevent assignment of a single decay rate for each voxel and thereby prevent a correct determination of the steady-state. However, for most applications the main emphasis is on the solid components of the brain, for which the method yields reliable results. Overall, the method has shown very promising results for accelerating CEST experiments relying on steady-state conditions.

For dualCEST, this technique bears the promise of enabling examination times which comply with the requirements for the daily clinical routine. In principle, there should be direct applicability, as the underlying analytical model also retains its validity for dualCEST. Previous experiments and simulations indicated the required exponential decay and build-up of the dualCEST signal.^{32,69} In a next step, further investigations will be needed to confirm these results, in particular the strictly mono-exponential behavior of the signal evolution. To this end, the utilization of the previously discussed simultaneous saturation might be beneficial as this would avoid the potential complication of two interleaved saturation phases with an individual exponential decay each. Another potential issue might be the previously observed small deviations for the rNOE in conventional CEST experiments. As the dualCEST signal is related closely to the same underlying physical phenomenon, i.e. the intramolecular spin diffusion processes, these deviations are very likely to also come into play here. Due to the complex calculation of the final dualCEST contrast, these small deviations could result in large errors for the final contrast. A potentially excessive acceleration should therefore be avoided at all cost. Having said that, even a moderate and cautious reduction of the presaturation should be sufficient to enable tremendous time savings while avoiding many of the aforementioned issues. For example, halving the current presaturation time from six to three seconds would guarantee a reasonable saturation of at least two times T_1 and lead to a 30% faster acquisition. In summary, this method presents a promising technique to facilitate a prospective application of dualCEST-MRI in the clinic.

3.2 In vivo application

Using the combined further developments discussed in the previous section, in Publication IV an imaging protocol was created which fulfills the requirements for clinical studies in terms of image quality and acquisition speed. The achieved protein specificity, reproducibility, and sensitivity to pathological alterations are of particular interest to further verify the

clinical applicability of this technique. Consequently, extensive investigations of biochemical model solutions and volunteers were performed, and first pilot studies with brain tumor and Alzheimer's patients were conducted.

Specificity and reproducibility

The preserved specificity of the dualCEST technique was investigated on the basis of biochemical model solutions. In a similar manner, previous *in vitro* experiments on a 14.1 T narrow-bore NMR spectrometer demonstrated the exceptional specificity of the approach to proteins. In conjunction with further investigations, observed signal changes were assignable to changes in the concentration, folding state, or molecular size of the bulk mobile proteins.³² To verify the preserved specificity and thus enable the assignment of observed changes *in vivo* to proteome alteration, a phantom with three model solutions was examined in this study. Each solution represented one of the major contributions to an *in vivo* Z-spectrum: proteins, metabolites, and macromolecules. As anticipated, only the protein compartment exhibited a non-zero signal in the acquired dualCEST images with negligible values everywhere else. This result confirms the preserved specificity of the approach, and thus allows the assignment of signal changes *in vivo* to genuine alterations of the proteome.

In addition to the specificity, a precise understanding of two other factors is required in order to properly assign observed features in patients to possible pathological alterations: the already preexisting contrast in healthy tissue and the comparability between different subjects. With regard to the latter, dualCEST has the advantage, that the measured quantity, i.e. $T_{protein}$, is a quantitative value, which renders a direct comparison between different subjects possible. It should be noted that a necessary prerequisite to ensure the comparability is the use of an identical experimental setup, i.e. the same imaging sequence, presaturation parameters, and magnetic field strength. With regard to the already preexisting contrast, in all subjects examined for this thesis, a small but consistent contrast between healthy tissue structures was observed with generally higher signal values in WM compared to GM. The only exception to this observation was the deep GM of the putamen, which was detected as a hyperintense region in multiple subjects and across several imaging slices. From previous MR spectroscopy studies analyzing macromolecular resonances attributed to mobile proteins, no significant differences in protein concentration or composition are expected for WM and GM.¹⁰¹ The observed differences are therefore most likely attributable to differences in the apparent water content of the two tissues. The dualCEST signal has previously been shown to be a measure of the relative protein concentration, and thus a dependence on the apparent water proton concentration is consequential.³² Of note, this additional dependence on the apparent water proton concentration is an unsolved issue for CEST-based approaches in general and affects all exchange-mediated techniques quantifying solutes indirectly via the water proton signal. As a consequence of this dependence, for an otherwise equal protein concentration and composition, the differences in water content of GM and WM (literature values of 81.9% and 70.9% respectively)¹⁰² result in a 15% higher signal for WM. This estimate is close to the actual observed contrast in this study, thus supporting the previous

3 Discussion

conclusions. To exclude this influence as well, in principle, an absolute protein content assessment could be achieved by a simple multiplication with a correction factor. To this end, the apparent water content would have to be quantified using established approaches based on T_1 and T_2^* measurements.¹⁰² Overall, the comparability of the dualCEST signal values between multiple subjects and the nearly imperceptible contrast in healthy tissue facilitate the identification of pathological alterations in forthcoming patient studies.

In a next step, as part of publication IV, the reproducibility of dualCEST-MRI was investigated by repeating measurements in vivo. To this purpose, mean values in regions of $3 \times 3 \times 1$ voxels were determined in a 'moving window' fashion and each time compared between the different measurements using Bland-Altman analysis¹⁰³ and the intraclass correlation coefficient (ICC).⁷⁹ By assessing the reproducibility based on regions of $3 \times 3 \times 1$ voxels, more meaningful results are obtained compared to using single voxels, as the spatial information is additionally incorporated (i.e. surrounding voxels). In contrast to taking only the mean of a single region of interest (e.g. a whole organ, tissue compartment or tumor), this approach avoids the reduction of a whole data set to a single value and thus preserves the 'image' nature of the data. Moreover, this approach results in a larger sample size for the statistical analyses and therefore in a more reliable quantification. It should be kept in mind that in doing so the obtained assessment results are only valid for investigations of $3 \times 3 \times 1$ voxel regions and thus have limited informative value for the individual image voxels. With regard to a potential diagnostic application assessing larger regions of interest, i.e. the entire tumor or the hippocampus for Alzheimer's, an even better reproducibility and sensitivity can be expected.

Scanning one healthy volunteer twice on two different days each (four times in total) allowed the determination of the intra-session, i.e. two consecutive measurements without repositioning in between, and the inter-session reproducibility. As might be expected, the determined intra-session reproducibility is better compared with inter-session repetitions. However, the only marginal differences indicate that the additional deviations, due to the repositioning and resulting partial volume effects, are rather small. Altogether, dualCEST-MRI demonstrated a good inter-session and good-to-excellent intra-session and overall reliability.⁷⁹

The reproducibility of conventional CEST-MRI has so far only been evaluated in a few studies, with various entities being investigated and widely varying evaluation standards.^{104–109} Most studies concerning an application in the brain utilized the coefficient of variation as their method of choice. However, for this study, the approach was not feasible as the coefficient of variation depends on determining the respective mean and variance of the investigated quantity (i.e. signal value of a single voxel or region of interest) across the repeated measurements, which is problematic with only two available data points (i.e. repetitions) for the intra- and inter-session evaluation. Moreover, in particular for APT-weighted CEST, it is questionable whether the coefficient of variation is a valid measure, as the investigated quantity (MTR_{asym}) does not have a 'natural' zero point and therefore does not qualify as a ratio variable, but only as an interval scale.¹¹⁰ A comparison of results would

thus be rendered meaningless. Studies based on more appropriate and sophisticated evaluation methods reported for APT-weighted CEST an ICC of 0.84 (95% confidence interval $CI_{95\%} = [0.72, 0.91]$) in the healthy brain and up to 0.96 ($CI_{95\%} = [0.91, 0.99]$) for patients with a glioma,¹⁰⁸ and an ICC of 0.95 (no confidence interval given) for patients with general brain tumors.¹⁰⁹ In comparison with the results obtained in Publication IV (ICC of 0.902 with $CI_{95\%} = [0.888, 0.913]$), dualCEST-MRI demonstrates reproducibility comparable to established conventional CEST-MRI protocols.

In addition to quantifying the reproducibility, repeated measurements allowed the smallest contrast change resolvable with dualCEST-MRI to be estimated. The utilized Bland-Altman analysis yields in addition to the bias, determined as the mean or median of the relative differences between two measurements, the limits of agreement, which confine 95% of these deviations. The determined relative limits of agreement of maximal 16% can therefore be interpreted as a threshold to distinguish genuine biophysical effects from measurement noise: contrast changes above 16% are with almost complete certainty genuine effects, whereas everything below could be a fluctuation. Whether this resolution capability is good enough to be of any diagnostic value will depend on the actual magnitude of change in pathologies, which must be assessed in future clinical studies. An estimate can be obtained from the preliminary results of pilot studies concerning cancer and Alzheimer's.

Pilot studies

In order to evaluate the diagnostic significance of dualCEST-MRI for examinations of humans, two pilot studies, examining brain tumor (Publications I and IV) and Alzheimer patients (Appendix C), are being conducted. The underlying hypothesis is that the increased specificity of the approach is particularly beneficial in two areas: (i) Due to its specificity, dualCEST could be used as a reference to evaluate the actual contribution of proteins to conventional CEST signal changes in disease states, which would provide new insights into the true clinical significance of protein CEST-MRI. And (ii), the better isolation of the protein signal changes from other interfering influences could lead to a larger observable effect and thus to a better sensitivity to the pathology under investigation. In the following section, the results of the pilot studies are discussed and analyzed in relation to both questions. It should be noted that the small number of patients examined so far does not yet allow for a final evaluation of either of the two questions. Nevertheless, the observations made so far already provide initial indications of possible findings.

In the first study with brain tumor patients, the dualCEST technique was confirmed to be able to identify the tumorous tissue. In both examined patients, a considerably lower signal was observed in the area of necrotic tissue, facilitating a clear delineation of the tumor region. In comparison, the surrounding healthy tissue exhibited contrast values in the order of the values obtained in volunteers, attesting once more to the comparability between different subjects. Due to the preserved specificity of dualCEST, the observed signal changes can be attributed to genuine pathological modification of mobile proteins (i.e. changes in the

3 Discussion

relative concentration, folding state, or molecular size). This attribution is further supported by the fact that necrotic tissue is known to consist of decomposing or dead cells.

The achieved specificity of the dualCEST approach is of particular interest for comparisons with conventional protein-attributed CEST signals, as it could provide new insights into the origin of protein CEST signals in vivo. In the first investigations, a great similarity between the dualCEST contrast and the conventional rNOE contrast was observed, which is also illustrated by a similar appearance in tumor tissue. This result is in line with previous expectations, since both quantities are primarily attributed to the intramolecular spin diffusion processes of mobile proteins.^{23,32} The remaining slight differences in the tumor region, as well as a generally less pronounced WM and GM contrast, could therefore be of particular interest, as they might indicate the contribution of additional effects, such as confounding contributions of metabolites or lipids, or additional physiological dependences. This is as well very interesting with regard to the first part of the study hypothesis, as these additional effects might have been misinterpreted as pathological protein changes. All in all, the observed contrast similarities and even more so the discrepancies, once again prove the necessity to investigate the origin and assignment of protein CEST signals.

A more precise assignment of the signals would not only be of interest for cancer, but also for neurodegenerative diseases such as Alzheimer's. For instance, a previously published patient study showed that there is a significant change in the CEST signal in the hippocampus of patients with Alzheimer's, but the tentative hypothesis that this is attributable to an increase of cytosolic proteins and peptides cannot be answered unequivocally from the data available.¹⁴ In this respect, the chosen asymmetry analysis (MRT_{asym}) is especially problematic as it mixes different signal influences. In addition to the targeted amide signal, the observed signal changes could also be caused by superimposing signals from rNOE, metabolites, lipids, and macromolecules, as well as by changes in the relaxation times T_1 and T_2 , or of the pH.⁶⁴ In this context, the results of a recent study in a mouse model indicate that the larger part of the contrast is actually caused by signals in the upfield frequency range, i.e. mainly attributed to the rNOE but potentially also to lipids and macromolecules.¹⁵ In contrast to the first Alzheimer study, the authors attribute the observed signal changes to protein aggregation processes. However, due to the ambiguity of the utilized method, no final conclusion is possible. The improved specificity of dualCEST might allow to evaluate the assignment of the signal changes to proteins, and more specifically to the aggregation thereof.

The first results of the Alzheimer's study, which was recently started as part of this work, indicate that a pathological change in the proteome can be detected. For one of the two patients examined, a significantly reduced dualCEST signal was observed across the whole image compared to the healthy control group. For this comparison, the age-induced biases were minimized by including only subjects from the same age group. Again, due to the specificity of dualCEST the signal differences can be attributed to a reduced relative concentration, a reduced average molecular size, or a denatured global folding state of bulk mobile proteins. In particular, the last possibility also includes the pathological formation of amyloid fibrils,

i.e. the aggregation of amyloid- β proteins, as demonstrated previously using *in vitro* experiments.⁶⁹ With regard to the conclusions of the previous Alzheimer's studies, the specificity of dualCEST allows at least some of the signal changes to be attributed to proteins, and additional indications are provided to support the assignment of the changes to aggregation processes.

In addition to the more precise assignment of effects, the preliminary results also seem to support the second part of the hypothesis, namely that the improved specificity of the dualCEST contrast also entails a better sensitivity. This can be understood in terms of the improved specificity of the approach allowing a better isolation of the protein signal of interest from other confounding signals, which would either dilute or even completely suppress the observable effect. The now observed larger effect size (25% relative signal change for dualCEST as compared to 20% for the conventional rNOE CEST) seems to corroborate this interpretation as it demonstrates the aforementioned effect dilution. However, as with all results of pilot studies, it is necessary to determine in a larger cohort whether this observation is valid only for the few cases studied or whether it corresponds to a consistent trend.

In the preliminary results it is striking that only in one of the two patients a change in the signal was observed, while the second showed no significant difference to the control group. At first glance, this result naturally casts doubt on the sensitivity of the method and the significance of the results obtained so far. However, the different response in both patients is consistent with the conventional rNOE CEST signals, and moreover with observations for an established anatomical marker, i.e. the enlargement of the ventricles. The latter has previously shown that it allows conclusions to be drawn about the current stage of the disease.¹¹¹ The seeming failure could therefore be the ability of dualCEST to assess disease progression. If this is true, dualCEST-MRI could be used to avoid other invasive modalities to monitor disease progression. As a result, examinations could be performed on a more regular and frequent basis, resulting in an improved level of patient care. However, due to the very small group of patients to date, these conclusions are rather speculative and should be treated with care. Nevertheless, the initial results seem promising and a subsequent inclusion of further study participants will allow final conclusions to be drawn.

In summary, the preliminary results of the two pilot studies show that dualCEST enables the identification of tumor tissue and first indications for a possible identification of Alzheimer's disease were obtained. For the Alzheimer's study, the effect size seems to be higher than what was observed for previous CEST approaches and, in addition, there might be evidence for a correlation with the disease progression. Smaller differences between the dualCEST and conventional protein contrast in tumor patients indicate that additional signaling influences are present, proving the value of dualCEST as a reference for *in vivo* experiments. However, for both studies the number of subjects is too small to draw any final conclusions. In the future, the inclusion of more study participants into the ongoing studies, as well as the start of new clinical studies with larger patient cohorts will be needed to conclusively assess the diagnostic value of dualCEST-MRI, particularly the potential of the dualCEST contrast as a biomarker for neurodegenerative diseases or cancer.

4 Conclusion

The aim of this study was the translation of the recently introduced dualCEST technique to a clinical whole-body MR scanner to enable the non-invasive imaging of endogenous proteins *in vivo*. To achieve this, several methodological developments were utilized, covering all parts of the technique: signal preparation, imaging readout, and post-processing. The developed imaging protocol was validated in extensive investigations of biochemical model solutions and volunteers, and was applied in pilot studies with brain tumor and Alzheimer's patients.

First, the impact of lower magnetic field strengths on the dualCEST signal was investigated, which revealed the signal broadening – which typically impairs conventional CEST approaches – to be beneficial for the dualCEST technique. A subsequent optimization of the RF saturation pulses in terms of amplitude, length, and timing allowed the maximization of signal strength while avoiding excessive broadening of spectral resonances. To further increase the saturation efficiency, novel cosine-modulated pulses were implemented which enabled a simultaneous irradiation of both involved frequency offsets. Finally, the dualCEST signal preparation module was combined with a fast and robust image readout and optimized for maximum SNR and volume coverage while avoiding contrast deviations. Moreover, a newly developed weighted acquisition scheme allowed for an optimal use of the limited examination time by adjusting the number of averages per frequency offset pair to the anticipated effect of the Z -value on the final contrast.

An important milestone for the application of dualCEST-MRI was the development and implementation of an effective and robust denoising technique. This technique is based on a dimensionality reduction using spectral redundancies, which are identified and exploited by the linear correlations between the tens of thousands of spectra acquired for each measurement. Combining the well-established dimensionality reduction technique PCA with an appropriate data-driven identification of the relevant information allowed noise-like characteristics to be separated from meaningful spectral features. Of note, the resulting improvements are not limited to the topic of this study but are relevant for CEST research in general. With regard to dualCEST-MRI, the denoising allowed the technique's inherently low SNR to be overcome, which facilitated examinations in a clinical setting.

The capability of the final dualCEST imaging protocol to meet the clinical needs in terms of practicability, reproducibility and imaging speed was verified in extensive *in vivo* and *in vitro* experiments. The preserved specificity of the dualCEST technique – following the extensive adaption to the clinical whole-body MR scanner – was confirmed in measurements of biochemical model solutions comprising all major compounds present in living tissue.

4 Conclusion

Furthermore, repeated volunteer measurements demonstrated the reproducibility and imaging speed to be on par with established conventional CEST imaging protocols. The reproducibility assessment moreover allowed quantification of the technique's capability to resolve genuine contrast changes from random fluctuations.

Finally, dualCEST-MRI was successfully applied in two pilot studies with brain tumor and Alzheimer's patients, demonstrating its applicability in a clinical setting. Due to the confirmed specificity of the dualCEST approach, the observed significant signal decrease in the glioblastoma region can be attributed to a pathological modification of mobile proteins. Furthermore, recent preliminary results of dualCEST-MRI examinations of the two Alzheimer's patients and two healthy age-matched volunteers revealed a considerable signal alteration in the hippocampus of one subject, potentially indicating the capability of dualCEST to assess disease progression. In the future, clinical studies with larger patient cohorts will allow the diagnostic value of dualCEST-MRI to be investigated, particularly its potential as a biomarker for neurodegenerative diseases or cancer. The exceptional protein specificity of this approach will allow for novel insights into the origin of protein CEST contrasts *in vivo* and, for the first time, for the determination of the actual contribution of mobile proteins to conventional CEST signal changes in pathologic tissue.

Within this study, a clinical dualCEST imaging modality was established, which enables the non-invasive investigation of endogenous proteins in living tissue. Due to its specificity, the approach may become a valuable diagnostic tool, providing complementary information on a molecular level for many diseases associated with pathological alterations of protein expression, particularly for cancer and Alzheimer's.

Appendices

The following research was originally submitted as abstract #453 to the *28th Annual Meeting of the International Society for Magnetic Resonance in Medicine, Paris, France 2020*. Reproduced with kind permission of the INTERNATIONAL SOCIETY FOR MAGNETIC RESONANCE IN MEDICINE.

A. Two-stage denoising of CEST-MRI data by principal component analysis of spectral groups

Johannes Breitling¹, Steffen Goerke¹, Mark E. Ladd¹, Peter Bachert¹, Andreas Korzowski¹

¹ *Division of Medical Physics in Radiology, German Cancer Research Center (DKFZ), Heidelberg, Germany*

Synopsis

In this study a novel method for the denoising of CEST MRI data is presented, combining the formation of subsets of similar spectra and the subsequent application of a principal component analysis. Exploiting only the subtle spectral differences of these reduced datasets – as opposed to using all spectra for the analysis – allows for a better identification and isolation of the obscured underlying spectral features. The proposed denoising resulted in an SNR gain by approximately a factor of four compared to the noisy initial data and an additional 14% compared to the conventional principal component analysis denoising.

Introduction

Recently, we developed an adaptive denoising algorithm for CEST spectra, combining the identification of spectral redundancies by means of a principal component analysis (PCA) with an appropriate data-driven truncation criterion to separate the relevant spectral features from noise-like characteristics.^{A1} However, an even better denoising performance for CEST data is desirable, for example, to generate high-SNR ground truths for the reliable training of neural networks. In this study a novel method is presented, extending the previous approach by a second stage of denoising^{A2,A3} (Step 3 in methods section). To this end, the result of the previously established denoising approach is used to define for each spectrum the subset of its most similar spectra. Subsequent application of a PCA to these reduced datasets – exhibiting only subtle

spectral differences – allows for a better identification and isolation of the obscured underlying spectral features.

Methods

The proposed denoising algorithm comprises the following steps (Fig. A.1):

Step 1: The acquired CEST data of size $u \times v \times y \times n$ (one 3D image for each of the n saturation frequency offsets) is reformatted into a Casorati matrix of size $m \times n$ (with $m \leq u \cdot v \cdot y$ being the number of remaining voxels after skull stripping). Subsequently, a variance-stabilizing transformation (VST) is applied to the matrix to correct for the Rician noise induced bias.^{A4}

Step 2: In the first denoising stage, all noisy spectra are denoised using the previously established adaptive

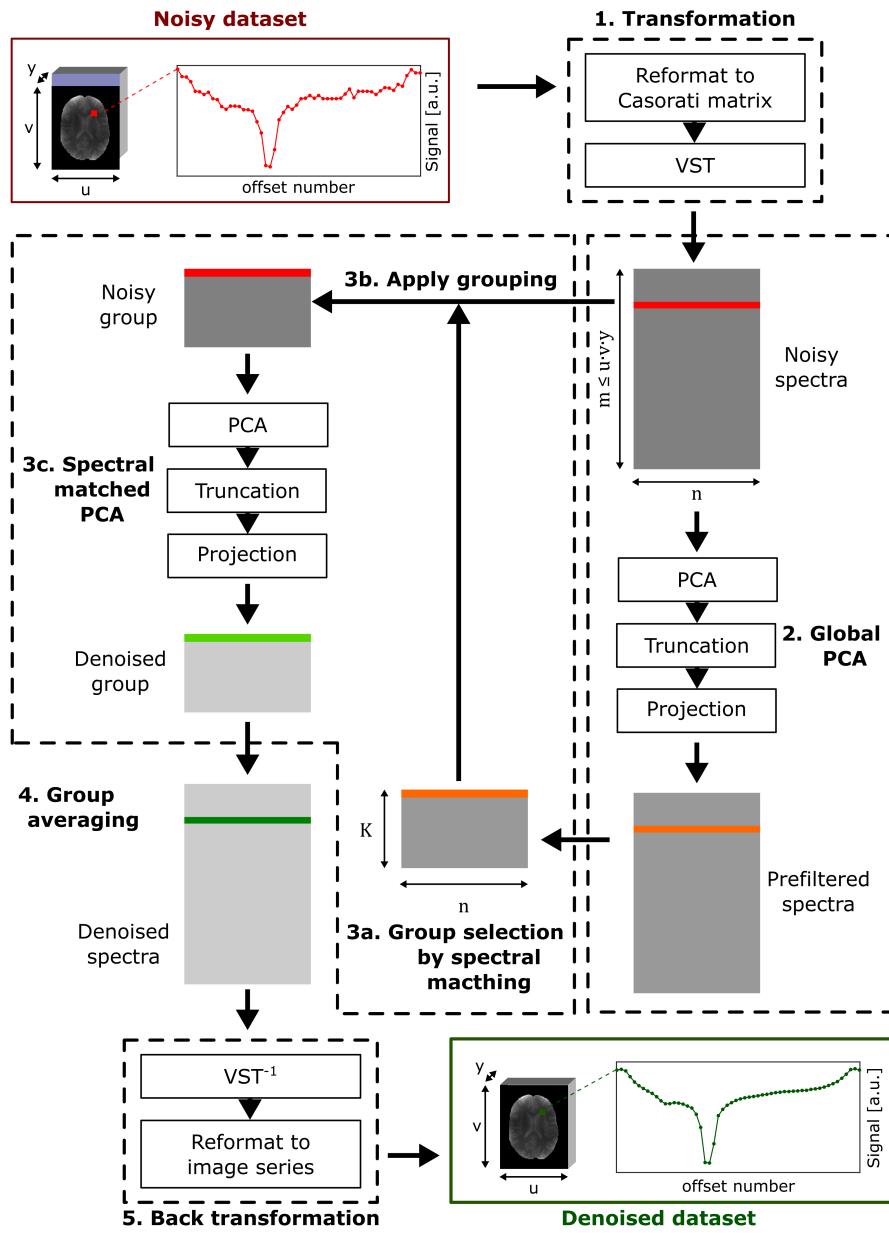


Figure A.1: Illustration of the proposed denoising algorithm (representative spectrum in color). In the first stage, transformed spectra (red) are denoised using an adaptive principal component analysis (PCA). In the second stage, each resulting prefiltered spectrum (orange) is grouped with its closest K spectra. The corresponding noisy groups are individually denoised using an adaptive PCA. The final denoised spectra (dark green) are obtained by averaging the corresponding spectra (light green) from all denoised groups. Finally, back transformation yields the denoised dataset.

PCA, whereby the optimal truncation is determined by the Nelson criterion.^{A1,A5}

Step 3: In the newly introduced second denoising stage, each resulting prefiltered spectrum is used to define the group of its K (in this study set to $10 \cdot n$) most similar spectra (Step 3a),^{A3} whereby the similarity between two spectra and is determined by the cosine similarity:

$$\text{sim}(\mathbf{s}_i, \mathbf{s}_j) = \frac{\mathbf{s}_i \cdot \mathbf{s}_j}{\|\mathbf{s}_i\| \cdot \|\mathbf{s}_j\|}$$

The corresponding groups of noisy spectra are each denoised individually using again the adaptive PCA (Step 3b and c). As a result, each group yields an estimate for all included spectra.

Step 4: The final denoised spectra are calculated by averaging the corresponding estimates from all groups.

Step 5: Application of the inverse VST and reformatting to an image series yields the denoised dataset.

In vivo 3D CEST MRI was performed on a 7T whole-body scanner (Siemens Healthineers, Germany) using the snapshot-CEST approach^{A6} with a matrix size of $128 \times 104 \times 12$ and a resolution of $1.7 \times 1.7 \times 3 \text{ mm}^3$. Presaturation was obtained by 140 Gaussian-shaped pulses ($t_p = 15 \text{ ms}$, duty cycle = 60%, $t_{\text{sat}} = 3.5 \text{ s}$, mean $B_1 = 0.7 \mu\text{T}$) applied at 56 unevenly distributed offsets. Low-SNR data as input for the denoising were acquired with bandwidth (BW) = 1560 Hz/pixel and flip angle (FA) = 1° and high-SNR data with BW = 560 Hz/pixel and $FA = 4^\circ$. All acquired image data were motion corrected using an automatic multimodal rigid registration algorithm in MITK,^{A7} corrected for B_0 inhomogeneities and manually skull stripped. A ground truth was obtained by averaging five high-SNR datasets and application of the first stage (i.e. single-stage) denoising. To obtain a reference for the denoising performance, the conventional single-stage denoising was also applied to the low-SNR data. Image contrasts were calculated by the asymmetric magnetization transfer ratio ($MTR_{\text{asym}} = (M(-\Delta\omega) - M(\Delta\omega))/M_0$) at $\Delta\omega = 3.5 \text{ ppm}$.

Results

Application of the proposed two-stage denoising algorithm to the low-SNR data results in an image quality comparable with the ground truth (see last paragraph in Methods for definition of the ground truth) and slightly improved compared to using only the conventional denoising approach (Fig. A.2). In the corresponding Bland-Altman plots (Fig. A.3), this translates into a reduced spread of the limits of agreement –

and thereby gain in SNR – by a factor of approximately four compared to the noisy initial data and 14% compared to the single-stage denoising. A small bias of the proposed denoising is observable (i.e. difference of the mean from zero in the Bland-Altman plot), which can however in large parts be assigned to the different BW and FA of the low-SNR data acquisition with respect to the ground truth as it is already present in the noisy data.

Discussion

The proposed method extends the previously presented denoising algorithm^{A1} by a second denoising stage allowing, improved image quality. Moreover, the selection and subsequent denoising of similar subsets of spectra reduces the risk of spectral features being undesirably removed or significantly blurred. This is especially important for rare spectral features only present in a small region of the acquisition volume (e.g. in the tumor) containing the important clinical information. However, introduction of the second stage comes at the cost of increased computation time, as the spectral matching and subsequent denoising are repeated for each voxel. In a next step, a thorough investigation on realistic simulations will be necessary to be able to compare the denoising results with an unbiased ground truth, thereby allowing quantification of the SNR gain across multiple noise levels, as well as investigation of the effect of the denoising on rare spectral features.

Conclusion

In this study, a novel denoising algorithm for CEST MRI is presented that exploits in a second stage the denoising of spectrally matched groups. The resulting improved image and spectral quality might in the future allow for the development of faster CEST imaging sequences, application of metrics and methods especially prone to noise, and generation of high-SNR ground truths for the reliable training of neural networks.

Acknowledgements

JB acknowledges the financial support of the International Max Planck Research School for Quantum Dynamics in Physics, Chemistry and Biology.

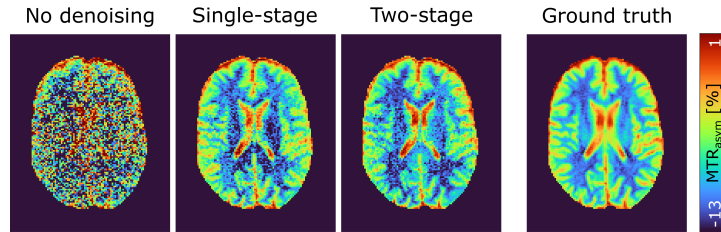


Figure A.2: MTR_{asym} contrasts (Slice 8 of 12) of a healthy volunteer demonstrating the slight improvement in image quality with the proposed two-stage denoising compared to only using the previously established single-stage approach.

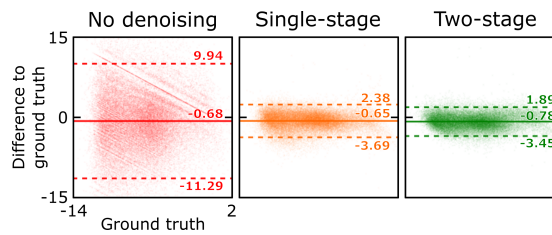


Figure A.3: Bland-Altman plots of the corresponding MTR_{asym} contrasts, including the bias (solid line) and the 95% limits of agreement (dashed lines). Application of the proposed two-stage denoising results in a reduced spread of the limits of agreement – and thereby SNR gain – by a factor of four compared to the noisy initial data and 14% compared to the single-stage denoising.

References

- A1 Breitling J, Deshmane A, Goerke S, et al. Adaptive Denoising For Chemical Exchange Saturation Transfer MR Imaging. *NMR Biomed.* 2019;32(11).
- A2 Zhang X, Peng J, Xu M, et al. Denoise Diffusion-Weighted Images Using Higher-Order Singular Value Decomposition. *Neuroimage.* 2017;156:128-145.
- A3 Zhang L, Dong W, Zhang D, Shi G. Two-Stage Image Denoising By Principal Component Analysis With Local Pixel Grouping. *Pattern Recognit.* 2010;43(4):1531-1549.
- A4 Foi A. Noise Estimation And Removal In MR Imaging: The Variance-Stabilization Approach. In: 2011 IEEE International Symposium on Biomedical Imaging: From Nano to Macro. IEEE; 2011:1809-1814.
- A5 Nelson LR. Some Observations On The Scree Test, And On Coefficient Alpha. *J Educ Res Meas.* 2005;3(1):1-17.
- A6 Zaiss M, Ehses P, Scheffler K. Snapshot-CEST: Optimizing Spiral-Centric-Reordered Gradient Echo Acquisition For Fast And Robust 3D CEST MRI At 9.4 T. *NMR Biomed.* 2018;31(4):e3879.
- A7 Floca R. Matchpoint: On Bridging The Innovation Gap Between Algorithmic Research And Clinical Use In Image Registration. In: *IFMBE Proceedings. Vol 25.* Springer, Berlin, Heidelberg; 2009:1105-1108.

The following research was originally presented as poster #2240 at the *Joint Annual Scientific Meeting ISMRM-ESMRMB, Paris, France 2018*. Reproduced with kind permission of the INTERNATIONAL SOCIETY FOR MAGNETIC RESONANCE IN MEDICINE.

B. Steady-state CEST-MRI using a reduced saturation period

Johannes Breitling¹, Steffen Goerke¹, Jan-Eric Meissner¹, Andreas Korzowski¹, Patrick Schuenke¹, Mark E. Ladd¹, Peter Bachert¹

¹ *Division of Medical Physics in Radiology, German Cancer Research Center (DKFZ), Heidelberg, Germany*

Synopsis

In this study, we propose a novel approach to determine the steady-state of CEST experiments without the application of prolonged saturation periods. This is achieved by numerically calculating the steady-state from a measurement with a reduced saturation period (in the order of the water proton T_1). This may allow quantitative CEST measurements, capable of providing information about pH and metabolite concentrations, in a reasonable and clinical relevant time frame.

Introduction

Quantitative chemical exchange saturation transfer (CEST) imaging has been shown to in principle allow absolute pH imaging and determination of metabolite concentrations^{B1,B2}. However, most of these techniques rely on the steady-state CEST signal, which requires a long saturation period in the order of 3-5 times the longitudinal relaxation time of water (T_{1w})^{B3}. For clinical applications a compromise has therefore to be made between a sufficiently long contrast preparation and feasible examination times^{B3}. Here we present an approach, which can bypass this obstacle by determining the steady-state of CEST experiments without the application of saturation in compliance with the steady-state criterion. Methods

Methods

During a pulsed CEST experiment (Fig. B.1a) the initial Z -magnetization Z_{init} can be assumed to mono-exponentially decay – via the so-called transient-state Z – towards the steady-state Z_{pulsed}^{ss} with the effective decay rate $R_{1\rho,pulsed}$ (Fig. B.1b)^{B4,B5}.

$$Z(\Delta\omega) = Z_{pulsed}^{ss} + (Z_{init} - Z_{pulsed}^{ss})e^{-t_{sat} \cdot R_{1\rho,pulsed}} \quad (B.1)$$

Z_{pulsed}^{ss} itself depends on $R_{1\rho,pulsed}$ according to

$$Z_{pulsed}^{ss} = \frac{R_{1w}(1 - DC + \cos^2 \theta \cdot DC)}{R_{1\rho,pulsed}} \quad (B.2)$$

with the tilt angle of the effective field $\theta = \tan^{-1}(\omega_1/\Delta\omega)$. This mathematical relation can be exploited to reduce the number of unknown parameters in Eq. B.1. For a known Z_{init} , this allows determining Z_{pulsed}^{ss} from Z for an arbitrary saturation time. Solving Eq. B.2 for the denominator and insertion in Eq. B.1 yields Z as function of Z_{pulsed}^{ss} .

$$Z(\Delta\omega) = Z_{pulsed}^{ss} + (Z_{init} - Z_{pulsed}^{ss}) \cdot e^{-t_{sat} \cdot R_{1w}(1 - DC + \cos^2 \theta \cdot DC)/Z_{pulsed}^{ss}} \quad (B.3)$$

Eq. B.3 cannot be solved analytically for Z_{pulsed}^{ss} . However since Z is a strictly monotonously increasing function of Z_{pulsed}^{ss} , a numerical calculation can be applied. This calculus requires Z and Z_{init} for each frequency offset $\Delta\omega$. In addition, B_0 , B_1 and T_{1w} have to be determined once. Z_{init} can be estimated pixelwise by the preceding measurement according to $Z_{init,i+1} = P_1 \cdot Z_i + P_0$, where P_1 and P_0 are determined in a calibration with the same sequence timings. All MR measurements were performed on a 7T whole-body scanner (Siemens Healthineers, Germany). Pre-saturation was obtained by either 60 or 700 Gaussian-shaped pulses (mean $B_1 = 0.5 \mu T$, $t_{sat} = 15$ ms, duty cycle = 60%) leading to a saturation time of $t_{sat} = 1.5$ s and

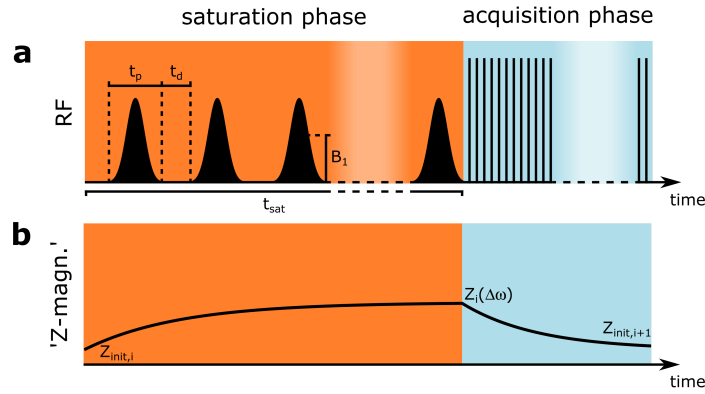


Figure B.1: (a) Sequence diagram of a typical CEST experiment, consisting of a saturation and subsequent acquisition phase. (b) During the saturation phase the initial Z -magnetization recovers towards the steady-state and is eventually read-out resulting in the initial magnetization for the next frequency offset.

17.5 s respectively. B_0 and B_1 were obtained using the WASABI approach^{B6} and T_{1w} with a saturation recovery sequence. Quantitative relayed nuclear Overhauser effect (rNOE)-CEST images were calculated using the apparent exchange-dependent relaxation rate (AREX)^{B5} with a 5-pool Lorentzian fit analysis.

Results

In a region of interest (ROI) analysis (Fig. B.2a), the conventional spectra exhibit strong differences in all ROIs (blue lines in Fig.B.2 b-d). On the contrary, the reconstructed Z -spectra (red lines) exhibit good agreement with negligible deviations in white matter (WM) and only minor ones in grey matter (GM) around $\Delta\omega = -3.5$ ppm. However, in cerebrospinal fluid (CSF) large differences can be observed. The calculated rNOE-CEST images display similar results for the novel approach compared to the steady-state with discrepancies only around the CSF, whereas the rNOE-CEST images acquired by the conventional method show significantly lower signal values across the entire image (Fig. B.3).

Discussion

In contrast to the conventional approach, the presented method was able to reproduce the steady-state in the main regions of the brain. As expected, the highest

agreement can be observed in WM due to a short T_{1w} of 1.4 s ($\approx t_{sat}$). The small deviations around $\Delta\omega = -3.5$ ppm in GM can potentially be explained by a comparably small exchange rate of the rNOE (around 5 Hz)^{B7} in combination with a longer T_{1w} . In this limit, the assumption of a mono-exponential decay does not hold anymore and rotation effects as well as exchange processes in the pauses would have to be considered^{B8}. In the reconstructed Z -spectrum of CSF considerable differences to the steady-state remain. This can be understood in terms of a partial volume effect, which does not allow assigning a single decay rate to each voxel and thereby prevents a correct reconstruction. However, in most CEST experiments the main emphasis is on the solid components of the brain (WM and GM) anyhow, for which the novel approach yields reliable results.

Conclusion

The proposed method was shown to enable steady-state CEST measurements without application of prolonged saturation periods. The resulting reduction in the required measurement time will eventually enable performing quantitative CEST examinations, allowing for example to assess pH, in a clinical relevant time frame.

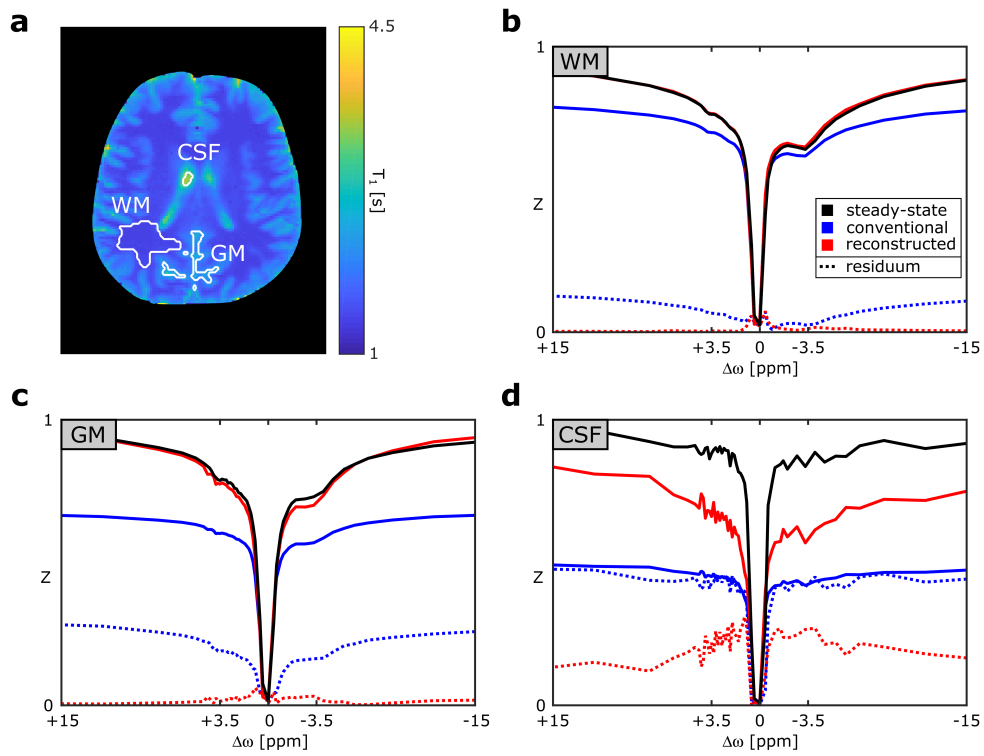


Figure B.2: (a) T1-map illustrating ROI evaluation for WM, GM and CSF of a healthy volunteer. (b-d) Strong deviations, plotted as residuum (dotted lines), between steady-state (black) and conventional (blue) Z-spectra in all ROIs are observable. By contrast, the novel approach (red) is able to reproduce the steady-state almost without deviations apart from CSF.

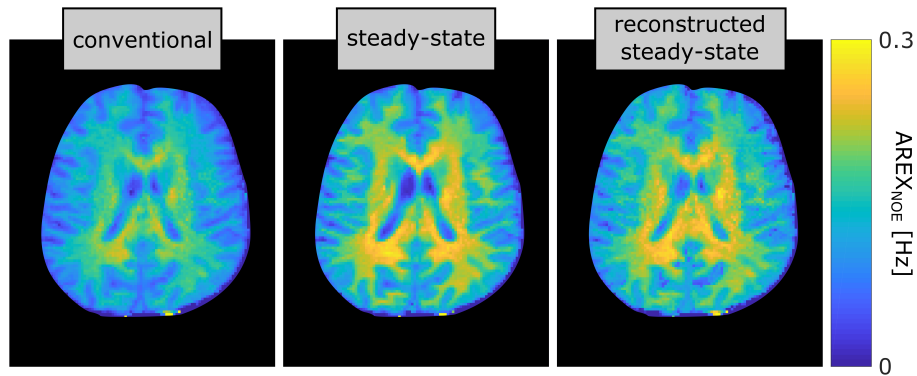


Figure B.3: Quantitative rNOE-CEST images show good agreement between the novel method and steady-state with larger deviations only observable around the CSF. In contrast, the images acquired by the conventional method show significantly lower signal values across the entire image.

Acknowledgements

JB acknowledges the financial support of the International Max Planck Research School for Quantum Dynamics in Physics, Chemistry and Biology.

References

- B1 McMahon, M. T. et al. Quantifying Exchange Rates in Chemical Exchange Saturation Transfer Agents Using the Saturation Time and Saturation Power Dependencies of the Magnetization Transfer Effect on the Magnetic Resonance Imaging Signal (QUEST and QUESP): pH Calibration for Poly-L-Lysine and a Starburst Dendrimer. *Magn Reson Med* 55, 836–847 (2006).
- B2 Sun PZ, Wang Y, Dai Z, Xiao G, Wu R. Quantitative chemical exchange saturation transfer (qCEST) MRI - RF spillover effect-corrected omega plot for simultaneous determination of labile proton fraction ratio and exchange rate. *Contrast Media Mol Imaging*. 2014 Jul;9(4):268–75.
- B3 Zaiss, M. & Bachert, P. Chemical exchange saturation transfer (CEST) and MR Z - spectroscopy in vivo : a review of theoretical approaches and methods. *Phys. Med. Biol.* 58, R221 (2013).
- B4 Santyr, G. E., Fairbanks, E. J., Kelcz, F. & Sorenson, J. A. Off-resonance spin locking for MR imaging. *Magn. Reson. Med.* 4. 32, 43–51 (1994).
- B5 Zaiss, M. et al. Inverse Z-spectrum analysis for spillover-, MT-, and T1-corrected steady-state pulsed CEST-MRI – application to pH-weighted MRI of acute stroke. *NMR Biomed.* 27, 240–252 (2014).
- B6 Schuenke, P. et al. Simultaneous mapping of water shift and B1(WASABI) – Application to field-Inhomogeneity correction of CESTMRI data. *Magn. Reson. Med.* 77, 571–580 (2017).
- B7 Friedman, J. I., Xia, D., Regatte, R. R. & Jerschow, A. Transfer Rate Edited experiment for the selective detection of Chemical Exchange via Saturation Transfer (TRE-CEST). *Journal of Magnetic Resonance* 256, 43–51 (2015).
- B8 Roeloffs, V., Meyer, C., Bachert, P. & Zaiss, M. Towards quantification of pulsed spinlock and CEST at clinical MR scanners: an analytical interleaved saturation–relaxation (ISAR) approach. *NMR Biomed.* 28, 40–53 (2015).

C. Application to patients with Alzheimer's disease

The specificity of dualCEST-MRI for the detection of changes in the concentration, molecular size, and folding state of mobile proteins is of particular interest as a marker for degenerative diseases such as Alzheimer's.³² In particular, it was possible to monitor the aggregation of amyloid beta and the formation of amyloid fibrils in vitro as decrease of the dualCEST signal.³³ Preliminary studies using the rather rudimentary APT-weighted CEST signal have revealed a signal increase in patients with however the origin not being unambiguously assignable to changes in the APT, rNOE or ssMT.¹⁴ Moreover, recently, a comparable decrease of conventional rNOE CEST signals was confirmed in an Alzheimer's disease transgenic mouse model.¹⁵ Examinations in human patients and volunteers are therefore of special interest to evaluate the potential of CEST- and in particular dualCEST-MRI for the diagnostic imaging of Alzheimer's and further more to investigate the underlying signal origin. In the following the first preliminary study results for dualCEST-MRI are presented.

Two patients with diagnosed Alzheimer's disease (56 and 68 years) and two healthy age-matched volunteers (56 and 57 years) were examined. Examinations were approved by the local ethics committee of the Medical Faculty of the University of Heidelberg and are in accordance with the relevant guidelines and regulations. Written informed consent was obtained prior to the examination.

All examinations were performed on a 3 T MR scanner (MAGNETOM Prisma; Siemens Healthineers, Erlangen, Germany) using the vendor's 64-channel head/neck coil. The imaging protocol consisted of (i) conventional T_2 -weighted, (ii) relaxation-compensated APT and rNOE CEST,⁹⁸ (iii) APT-weighted CEST, and (iv) dualCEST. With regard to the imaging protocol established in publication IV, only the denoising was altered and replaced by the advanced approach described in appendix A. The image data of the first three modalities have been submitted as a conference abstract to the *28th Annual Meeting of the International Society for Magnetic Resonance in Medicine, Paris, France 2020*.¹¹²

The dualCEST-MRI of healthy volunteers exhibits the expected contrast with a clearly delineated CSF and a slightly hyperintense WM compared to GM (cf. Figure C.1 and Figure 5 of publication IV). However, for the Alzheimer's patients an incoherent contrast behavior is observable. In patient one a global decrease of the dualCEST protein signal is apparent, indicating, as expected, a considerable degeneration of the proteins and decline of the brain structure. In contrast patient two exhibits no apparent abnormalities compared to the healthy volunteers. This differing behavior is however actually in coherence with the noticeable ventricle enlargement of patient one as compared to patient two and could therefore indicate a difference in the disease progression. Statistical analysis of the dualCEST contrast in the hippocampus (Figure C.1, magenta border) determined significantly different signal values for patient one compared to the other three subjects, with the mean being well outside of the other standard deviation ranges (Figure C.2). A similar tendency is apparent for the conventional rNOE CEST signal (Figure C.3) with however a less distinct and smaller effect size.

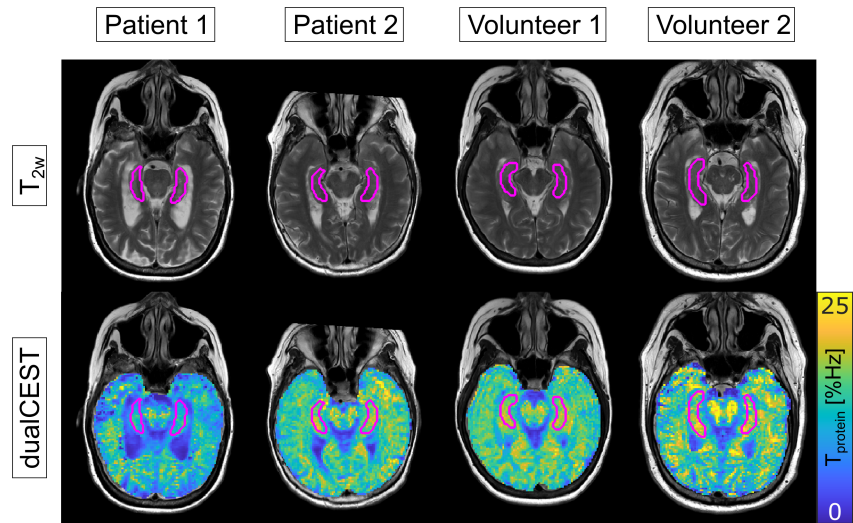


Figure C.1: Representative slices of the dualCEST-MRI examinations of two Alzheimer’s patients and two healthy volunteers. For statistical analysis, regions of interest in the hippocampus (magenta border) were defined on the anatomical T_2 -weighted images.

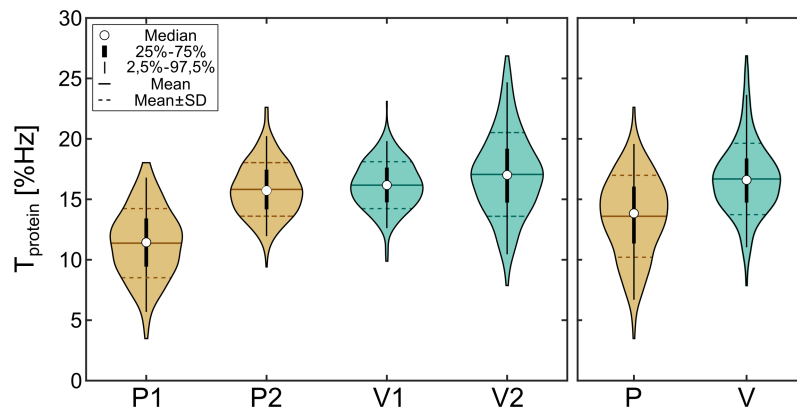


Figure C.2: Violin plots (i.e. extended box plots) depicting the data distribution of dualCEST voxel values inside the regions of interest (Fig. C.1). Data is shown for both, individual subjects (patients P1 and P2, volunteers V1 and V2) and for the overall data sets of patients (P) and volunteers (V). The plots include markers for median, interquartile ranges, mean and standard deviation (SD) ranges.

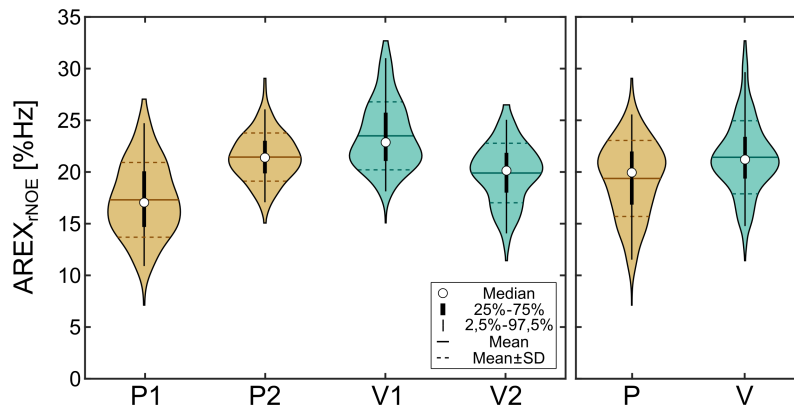


Figure C.3: Violin plots depicting the rNOE data distribution, equivalent to figure C.2.

The preliminary results support the potential of dualCEST-MRI for diagnostic imaging of Alzheimer's disease. The observed signal decrease in the first patient is in line with the results of the in vitro study³³ and moreover with the mouse model examined using conventional rNOE CEST.¹⁵ The differing contrast behavior of the second patient, exhibiting signal values very similar to the ones of volunteers, could potentially be explained by a difference in the disease progression. DualCEST-MRI might therefore have the potential to be used for assessing the severity of the disease. However, the study size (two patients and two volunteers) is yet too small to determine any statistical significance. In the future, inclusion of more participants with clearly defined disease progression states will be essential to assess the potential of dualCEST-MRI as a diagnostic tool.

Bibliography

- [1] Diagnostic imaging. World Health Organization. website https://www.who.int/diagnostic_imaging/en/. Accessed February 29, 2020.
- [2] Medical Imaging. U. S. Food and Drug Administration. website <https://www.fda.gov/radiation-emitting-products/radiation-emitting-products-and-procedures/medical-imaging/>. Accessed February 29, 2020.
- [3] Merboldt KD, Hänicke W, Frahm J. Self-diffusion NMR imaging using stimulated echoes. *Journal of Magnetic Resonance (1969)*. 1985;64(3):479–486.
- [4] Taylor DG, Bushell MC. The spatial mapping of translational diffusion coefficients by the NMR imaging technique. *Physics in Medicine and Biology*. 1985;30(4):345–349.
- [5] Frahm J, Bruhn H, Merboldt KD, Hänicke W. Dynamic MR imaging of human brain oxygenation during rest and photic stimulation. *Journal of Magnetic Resonance Imaging*. 1992;2(5):501–505.
- [6] Frahm J, Bruhn H, Gyngell ML, Merboldt KD, Hänicke W, Sauter R. Localized high-resolution proton NMR spectroscopy using stimulated echoes: Initial applications to human brain in vivo. *Magnetic Resonance in Medicine*. 1989;9(1):79–93.
- [7] Forsén S, Hoffman RA. Study of Moderately Rapid Chemical Exchange Reactions by Means of Nuclear Magnetic Double Resonance. *The Journal of Chemical Physics*. 1963;39(11):2892–2901.
- [8] Ward K, Aletras A, Balaban R. A New Class of Contrast Agents for MRI Based on Proton Chemical Exchange Dependent Saturation Transfer (CEST). *Journal of Magnetic Resonance*. 2000;143(1):79–87.
- [9] McMahon MT, Gilad AA, Bulte JW, van Zijl PC. *Chemical Exchange Saturation Transfer Imaging: Advances and Applications*. Singapore: Pan Stanford Publishing Pte Ltd; 1st ed.2017.
- [10] Zhou J, Payen JF, Wilson DA, Traystman RJ, van Zijl PCM. Using the amide proton signals of intracellular proteins and peptides to detect pH effects in MRI. *Nature Medicine*. 2003;9(8):1085–1090.
- [11] Yan K, Fu Z, Yang C, et al. Assessing Amide Proton Transfer (APT) MRI Contrast Origins in 9 L Gliosarcoma in the Rat Brain Using Proteomic Analysis. *Molecular Imaging and Biology*. 2015;17(4):479–487.

Bibliography

- [12] Jones CK, Huang A, Xu J, et al. Nuclear Overhauser enhancement (NOE) imaging in the human brain at 7 T. *NeuroImage*. 2013;77:114–124.
- [13] Zaiss M, Windschuh J, Paech D, et al. Relaxation-compensated CEST-MRI of the human brain at 7 T: Unbiased insight into NOE and amide signal changes in human glioblastoma. *NeuroImage*. 2015;112:180–188.
- [14] Wang R, Li SY, Chen M, et al. Amide Proton Transfer Magnetic Resonance Imaging of Alzheimer's Disease at 3.0 Tesla. *Chinese Medical Journal*. 2015;128(5):615–619.
- [15] Chen L, Wei Z, Chan KW, et al. Protein aggregation linked to Alzheimer's disease revealed by saturation transfer MRI. *NeuroImage*. 2019;188:380–390.
- [16] Zhou J, Lal B, Wilson DA, Laterra J, van Zijl PC. Amide proton transfer (APT) contrast for imaging of brain tumors. *Magnetic Resonance in Medicine*. 2003;50(6):1120–1126.
- [17] Zaiss M, Windschuh J, Goerke S, et al. Downfield-NOE-suppressed amide-CEST-MRI at 7 Tesla provides a unique contrast in human glioblastoma. *Magnetic Resonance in Medicine*. 2017;77(1):196–208.
- [18] Cai K, Haris M, Singh A, et al. Magnetic resonance imaging of glutamate. *Nature Medicine*. 2012;18(2):302–306.
- [19] Haris M, Nanga RPR, Singh A, et al. Exchange rates of creatine kinase metabolites: feasibility of imaging creatine by chemical exchange saturation transfer MRI. *NMR in Biomedicine*. 2012;25(11):1305–1309.
- [20] Chan KWY, McMahan MT, Kato Y, et al. Natural D-glucose as a biodegradable MRI contrast agent for detecting cancer. *Magnetic Resonance in Medicine*. 2012;68(6):1764–1773.
- [21] Walker-Samuel S, Ramasawmy R, Torrealdea F, et al. In vivo imaging of glucose uptake and metabolism in tumors. *Nature Medicine*. 2013;19(8):1067–1072.
- [22] Schuenke P, Paech D, Koehler C, et al. Fast and Quantitative T1p-weighted Dynamic Glucose Enhanced MRI. *Scientific Reports*. 2017;7(1):1–10.
- [23] van Zijl PC, Zhou J, Mori N, Payen JF, Wilson D, Mori S. Mechanism of magnetization transfer during on-resonance water saturation. A new approach to detect mobile proteins, peptides, and lipids. *Magnetic Resonance in Medicine*. 2003;49(3):440–449.
- [24] Henkelman RM, Huang X, Xiang QS, Stanisz GJ, Swanson SD, Bronskill MJ. Quantitative interpretation of magnetization transfer. *Magnetic Resonance in Medicine*. 1993;29(6):759–766.
- [25] Henkelman RM, Stanisz GJ, Graham SJ. Magnetization transfer in MRI: A review. *NMR in Biomedicine*. 2001;14(2):57–64.

- [26] Zaiss M, Zu Z, Xu J, et al. A combined analytical solution for chemical exchange saturation transfer and semi-solid magnetization transfer. *NMR in Biomedicine*. 2015;28(2):217–230.
- [27] Goerke S, Zaiss M, Bachert P. Characterization of creatine guanidinium proton exchange by water-exchange (WEX) spectroscopy for absolute-pH CEST imaging in vitro. *NMR in Biomedicine*. 2014;27(5):507–518.
- [28] Liepinsh E, Otting G. Proton exchange rates from amino acid side chains— implications for image contrast. *Magnetic Resonance in Medicine*. 1996;35(1):30–42.
- [29] Friedman JI, McMahon MT, Stivers JT, Van Zijl PC. Indirect detection of labile solute proton spectra via the water signal using frequency-labeled exchange (FLEX) transfer. *Journal of the American Chemical Society*. 2010;132(6):1813–1815.
- [30] Zu Z, Janve VA, Xu J, Does MD, Gore JC, Gochberg DF. A new method for detecting exchanging amide protons using chemical exchange rotation transfer. *Magnetic Resonance in Medicine*. 2013;69(3):637–647.
- [31] Xu J, Yadav NN, Bar-Shir A, et al. Variable delay multi-pulse train for fast chemical exchange saturation transfer and relayed-nuclear overhauser enhancement MRI. *Magnetic Resonance in Medicine*. 2014;71(5):1798–1812.
- [32] Goerke S, Breitling J, Zaiss M, et al. Dual-frequency irradiation CEST-MRI of endogenous bulk mobile proteins. *NMR in Biomedicine*. 2018;31(6):e3920.
- [33] Breitling J. Towards in vivo protein imaging by means of dualCEST [master's thesis]. Heidelberg, Germany: University of Heidelberg; 2017.
- [34] Gerlach W, Stern O. Der experimentelle Nachweis der Richtungsquantelung im Magnetfeld. *Zeitschrift für Physik*. 1922;9(1):349–352.
- [35] Rabi II, Zacharias JR, Millman S, Kusch P. A new method of measuring nuclear magnetic moment. *Physical Review*. 1938;53(4):318.
- [36] Bloch F, Hansen WW, Packard M. Nuclear Induction. *Physical Review*. 1946;69(3-4):127–127.
- [37] Purcell EM, Torrey HC, Pound RV. Resonance Absorption by Nuclear Magnetic Moments in a Solid. *Physical Review*. 1946;69(1-2):37–38.
- [38] Proctor WG, Yu FC. The Dependence of a Nuclear Magnetic Resonance Frequency upon Chemical Compound. *Physical Review*. 1950;77(5):717–717.
- [39] Dickinson WC. Dependence of the F19 nuclear resonance position on chemical compound. *Physical Review*. 1950;77(5):736–737.
- [40] Lauterbur PC. Image formation by induced local interactions: Examples employing nuclear magnetic resonance. *Nature*. 1973;242(5394):190–191.

Bibliography

- [41] Mansfield P, Grannell P. NMR 'diffraction' in solids. *Journal of Physics. C, Solid State Physics*. 1973;6(22):L422–L426.
- [42] Moon RB, Richards JH. Determination of Intracellular pH by ^{31}P Magnetic Resonance. *Journal of Biological Chemistry*. 1973;248(20):7276–7278.
- [43] Ren J, Shang T, Sherry AD, Malloy CR. Unveiling a hidden ^{31}P signal coresonating with extracellular inorganic phosphate by outer-volume-suppression and localized ^{31}P MRS in the human brain at 7T. *Magnetic Resonance in Medicine*. 2018;80(4):1289–1297.
- [44] Mulkern RV, Williams ML. The general solution to the Bloch equation with constant rf and relaxation terms: Application to saturation and slice selection. *Medical Physics*. 1993;20(1):5–13.
- [45] Zaiss M, Bachert P. Chemical exchange saturation transfer (CEST) and MR Z-spectroscopy in vivo: a review of theoretical approaches and methods. *Physics in Medicine and Biology*. 2013;58(22):R221–R269.
- [46] Overhauser AW. Polarization of Nuclei in Metals. *Physical Review*. 1953;92(2):411–415.
- [47] van Zijl PCM, Yadav NN. Chemical exchange saturation transfer (CEST): What is in a name and what isn't?. *Magnetic Resonance in Medicine*. 2011;65(4):927–948.
- [48] Kogan F, Haris M, Singh A, et al. Method for high-resolution imaging of creatine in vivo using chemical exchange saturation transfer. *Magnetic Resonance in Medicine*. 2014;71(1):164–172.
- [49] Rerich E, Zaiss M, Korzowski A, Ladd ME, Bachert P. Relaxation-compensated CEST-MRI at 7T for mapping of creatine content and pH - preliminary application in human muscle tissue in vivo. *NMR in Biomedicine*. 2015;28(11):1402–1412.
- [50] DeBrosse C, Nanga RPR, Bagga P, et al. Lactate Chemical Exchange Saturation Transfer (LATEST) Imaging in vivo A Biomarker for LDH Activity. *Scientific Reports*. 2016;6(1):1–10.
- [51] Haris M, Cai K, Singh A, Hariharan H, Reddy R. In vivo mapping of brain myo-inositol. *NeuroImage*. 2011;54(3):2079–2085.
- [52] Longo DL, Busato A, Lanzardo S, Antico F, Aime S. Imaging the pH evolution of an acute kidney injury model by means of iopamidol, a MRI-CEST pH-responsive contrast agent. *Magnetic Resonance in Medicine*. 2013;70(3):859–864.
- [53] Longo DL, Dastrù W, Digilio G, et al. Iopamidol as a responsive MRI-chemical exchange saturation transfer contrast agent for pH mapping of kidneys: In vivo studies in mice at 7 T. *Magnetic Resonance in Medicine*. 2011;65(1):202–211.

- [54] Jones CK, Schlosser MJ, van Zijl PC, Pomper MG, Golay X, Zhou J. Amide proton transfer imaging of human brain tumors at 3T. *Magnetic Resonance in Medicine*. 2006;56(3):585–592.
- [55] Wen Z, Hu S, Huang F, et al. MR imaging of high-grade brain tumors using endogenous protein and peptide-based contrast. *NeuroImage*. 2010;51(2):616–622.
- [56] Togao O, Yoshiura T, Keupp J, et al. Amide proton transfer imaging of adult diffuse gliomas: correlation with histopathological grades. *Neuro-Oncology*. 2014;16(3):441–448.
- [57] Takayama Y, Nishie A, Togao O, et al. Amide Proton Transfer MR Imaging of Endometrioid Endometrial Adenocarcinoma: Association with Histologic Grade. *Radiology*. 2018;286(3):909–917.
- [58] Zhou J, Tryggstad E, Wen Z, et al. Differentiation between glioma and radiation necrosis using molecular magnetic resonance imaging of endogenous proteins and peptides. *Nature Medicine*. 2011;17(1):130–134.
- [59] Mehrabian H, Desmond KL, Soliman H, Sahgal A, Stanisiz GJ. Differentiation between Radiation Necrosis and Tumor Progression Using Chemical Exchange Saturation Transfer. *Clinical Cancer Research*. 2017;23(14):3667–3675.
- [60] Meissner JE, Korzowski A, Regnery S, et al. Early response assessment of glioma patients to definitive chemoradiotherapy using chemical exchange saturation transfer imaging at 7 T. *Journal of Magnetic Resonance Imaging*. 2019;50(4):1268–1277.
- [61] Li C, Peng S, Wang R, et al. Chemical exchange saturation transfer MR imaging of Parkinson's disease at 3 Tesla. *European Radiology*. 2014;24(10):2631–2639.
- [62] Dula AN, Asche EM, Landman BA, et al. Development of chemical exchange saturation transfer at 7T. *Magnetic Resonance in Medicine*. 2011;66(3):831–838.
- [63] McConnell HM. Reaction Rates by Nuclear Magnetic Resonance. *The Journal of Chemical Physics*. 1958;28(3):430–431.
- [64] Zaiss M, Bachert P. Exchange-dependent relaxation in the rotating frame for slow and intermediate exchange - modeling off-resonant spin-lock and chemical exchange saturation transfer. *NMR in Biomedicine*. 2013;26(5):507–518.
- [65] Trott O, Palmer AG. $R1\rho$ Relaxation outside of the Fast-Exchange Limit. *Journal of Magnetic Resonance*. 2002;154(1):157–160.
- [66] Zaiss M, Xu J, Goerke S, et al. Inverse Z -spectrum analysis for spillover-, MT-, and T1 -corrected steady-state pulsed CEST-MRI - application to pH-weighted MRI of acute stroke. *NMR in Biomedicine*. 2014;27(3):240–252.
- [67] Goerke S. Einfluss von Entfaltung und Aggregation auf den ^1H -Magnetisierungstransfer zwischen Proteinen und freiem Wasser [dissertation]. Heidelberg, Germany: University of Heidelberg; 2015.

Bibliography

- [68] Neuhaus D, Williamson MP. *The nuclear Overhauser effect in structural and conformational analysis*. VCH; 1989.
- [69] Breitling J, Goerke S, Ladd ME, Bachert P, Korzowski A. Two-stage denoising of CEST-MRI data by principal component analysis of spectral groups. In: Proceedings of the 28th Annual Meeting of the International Society for Magnetic Resonance in Medicine. Paris, France; 2020.
- [70] Breitling J, Goerke S, Meissner JE, et al. Steady-state CEST-MRI using a reduced saturation period. In: Joint Annual Scientific Meeting ISMRM-ESMRMB. Paris, France; 2018.
- [71] Zaiss M, Ehse P, Scheffler K. Snapshot-CEST: Optimizing spiral-centric-reordered gradient echo acquisition for fast and robust 3D CEST MRI at 9.4 T. *NMR in Biomedicine*. 2018;31(4):e3879.
- [72] Hotelling H. Analysis of a complex of statistical variables into principal components. *Journal of Educational Psychology*. 1933;24(6):417–441.
- [73] Nelson LR. Some Observations on the Scree Test, and on Coefficient Alpha. *Journal of Educational Research and Measurement*. 2005;3(1):1–17.
- [74] Malinowski ER. Determination of the number of factors and the experimental error in a data matrix. *Analytical Chemistry*. 1977;49(4):612–617.
- [75] Manjón JV, Coupé P, Buades A. MRI noise estimation and denoising using non-local PCA. *Medical Image Analysis*. 2015;22(1):35–47.
- [76] Balvay D, Kachenoura N, Espinoza S, et al. Signal-to-Noise Ratio Improvement in Dynamic Contrast-enhanced CT and MR Imaging with Automated Principal Component Analysis Filtering. *Radiology*. 2011;258(2):435–445.
- [77] Lee JS, Khitrin AK, Regatte RR, Jerschow A. Uniform saturation of a strongly coupled spin system by two-frequency irradiation. *The Journal of Chemical Physics*. 2011;134(23):234504.
- [78] Prevost V, Girard O, Mchinda S, Varma G, Alsop D, Duhamel G. Optimization of inhomogeneous magnetization transfer (ihMT) MRI contrast for preclinical studies using dipolar relaxation time (T1D) filtering. *NMR in Biomedicine*. 2017;30(6):e3706.
- [79] Koo TK, Li MY. A Guideline of Selecting and Reporting Intraclass Correlation Coefficients for Reliability Research.. *Journal of chiropractic medicine*. 2016;15(2):155–63.
- [80] Wüthrich K. *NMR of proteins and nucleic acids*. New York: Wiley; 1986.
- [81] Ladd ME, Bachert P, Meyerspeer M, et al. Pros and cons of ultra-high-field MRI/MRS for human application. *Progress in Nuclear Magnetic Resonance Spectroscopy*. 2018;109:1–50.

- [82] van Zijl PC, Lam WW, Xu J, Knutsson L, Stanisz GJ. Magnetization Transfer Contrast and Chemical Exchange Saturation Transfer MRI. Features and analysis of the field-dependent saturation spectrum. *NeuroImage*. 2018;168:222–241.
- [83] Windschuh J, Zaiss M, Meissner JE, et al. Correction of B1-inhomogeneities for relaxation-compensated CEST imaging at 7 T. *NMR in Biomedicine*. 2015;28(5):529–537.
- [84] Katscher U, Börnert P. Parallel RF transmission in MRI. *NMR in Biomedicine*. 2006;19(3):393–400.
- [85] Keupp J, Baltes C, Harvey PR, van den Brink J. Parallel RF Transmission based MRI Technique for Highly Sensitive Detection of Amide Proton Transfer in the Human Brain at 3T. In: Proceedings of the 19th Annual Meeting of the International Society for Magnetic Resonance in Medicine. Montreal, Canada; 2011.
- [86] Liebert A, Zaiss M, Gumbrecht R, et al. Multiple interleaved mode saturation (MI-MOSA) for B1+ inhomogeneity mitigation in chemical exchange saturation transfer. *Magnetic Resonance in Medicine*. 2019;82(2):693–705.
- [87] Schmitt B, Zaiss M, Zhou J, Bachert P. Optimization of pulse train presaturation for CEST imaging in clinical scanners. *Magnetic Resonance in Medicine*. 2011;65(6):1620–1629.
- [88] Gudbjartsson H, Patz S. The rician distribution of noisy mri data. *Magnetic Resonance in Medicine*. 1995;34(6):910–914.
- [89] Aja-Fernández S, Tristán-Vega A, Hoge WS. Statistical Noise Analysis in GRAPPA Using a Parametrized Noncentral Chi Approximation Model. *Magnetic resonance in medicine : official journal of the Society of Magnetic Resonance in Medicine / Society of Magnetic Resonance in Medicine*. 2011;65(4):1195.
- [90] Döpfert J, Witte C, Kunth M, Schröder L. Sensitivity enhancement of (Hyper-)CEST image series by exploiting redundancies in the spectral domain. *Contrast Media & Molecular Imaging*. 2014;9(1):100–107.
- [91] Foi A. Noise estimation and removal in MR imaging: The variance-stabilization approach. In: :1809–1814IEEE; 2011.
- [92] Wech T, Köstler H. Robust motion correction in CEST imaging exploiting low-rank approximation of the z-spectrum. *Magnetic Resonance in Medicine*. 2018;80(5):1979–1988.
- [93] Zaitsev M, Dold C, Sakas G, Hennig J, Speck O. Magnetic resonance imaging of freely moving objects: prospective real-time motion correction using an external optical motion tracking system. *NeuroImage*. 2006;31(3):1038–1050.

Bibliography

- [94] Simegn GL, Van der Kouwe AJ, Robertson FC, Meintjes EM, Alhamud A. Real-time simultaneous shim and motion measurement and correction in glycoCEST MRI using double volumetric navigators (DvNavs). *Magnetic Resonance in Medicine*. 2019;81(4):2600–2613.
- [95] Zhang L, Dong W, Zhang D, Shi G. Two-stage image denoising by principal component analysis with local pixel grouping. *Pattern Recognition*. 2010;43(4):1531–1549.
- [96] Zhang X, Peng J, Xu M, et al. Denoise diffusion-weighted images using higher-order singular value decomposition. *NeuroImage*. 2017;156:128–145.
- [97] Brender JR, Kishimoto S, Merkle H, et al. Dynamic Imaging of Glucose and Lactate Metabolism by ¹³C-MRS without Hyperpolarization. *Scientific Reports*. 2019;9(1):3410.
- [98] Goerke S, Soehngen Y, Deshmane A, et al. Relaxation-compensated APT and rNOE CEST-MRI of human brain tumors at 3 T. *Magnetic Resonance in Medicine*. 2019;82(2):622–632.
- [99] Friedman JI, Xia D, Regatte RR, Jerschow A. Transfer Rate Edited experiment for the selective detection of Chemical Exchange via Saturation Transfer (TRE-CEST). *Journal of Magnetic Resonance*. 2015;256:43–51.
- [100] Roeloffs V, Meyer C, Bachert P, Zaiss M. Towards quantification of pulsed spinlock and CEST at clinical MR scanners: An analytical interleaved saturation-relaxation (ISAR) approach. *NMR in Biomedicine*. 2015;28(1):40–53.
- [101] Snoussi K, Gillen JS, Horska A, et al. Comparison of brain gray and white matter macromolecule resonances at 3 and 7 Tesla. *Magnetic Resonance in Medicine*. 2015;74(3):607–613.
- [102] Neeb H, Zilles K, Shah N. A new method for fast quantitative mapping of absolute water content in vivo. *NeuroImage*. 2006;31(3):1156–1168.
- [103] Bland JM, Altman DG. Statistical methods for assessing agreement between two methods of clinical measurement. *The Lancet*. 1986;327(8476):307–310.
- [104] Dula AN, Dewey BE, Arlinghaus LR, et al. Optimization of 7-T Chemical Exchange Saturation Transfer Parameters for Validation of Glycosaminoglycan and Amide Proton Transfer of Fibroglandular Breast Tissue. *Radiology*. 2015;275(1):255–261.
- [105] Evans VS, Torrealdea F, Rega M, et al. Optimization and Repeatability of Multipool Chemical Exchange Saturation Transfer MRI of the Prostate at 3.0 T. *Journal of Magnetic Resonance Imaging*. 2019;:jmri.26690.
- [106] Nanga RPR, DeBrosse C, Kumar D, et al. Reproducibility of 2DGluCEST in healthy human volunteers at 7 T. *Magnetic Resonance in Medicine*. 2018;80(5):2033–2039.

- [107] Yuan J, Chen S, King AD, et al. Amide proton transfer-weighted imaging of the head and neck at 3 T: a feasibility study on healthy human subjects and patients with head and neck cancer. *NMR in Biomedicine*. 2014;27(10):1239–1247.
- [108] Lee JB, Park JE, Jung SC, et al. Repeatability of amide proton transfer-weighted signals in the brain according to clinical condition and anatomical location. *European Radiology*. 2020;30(1):346–356.
- [109] Togao O, Hiwatashi A, Keupp J, et al. Scan-rescan reproducibility of parallel transmission based amide proton transfer imaging of brain tumors. *Journal of Magnetic Resonance Imaging*. 2015;42(5):1346–1353.
- [110] Eisenberg DTA. Telomere length measurement validity: the coefficient of variation is invalid and cannot be used to compare quantitative polymerase chain reaction and Southern blot telomere length measurement techniques. *International Journal of Epidemiology*. 2016;45(4):1295–1298.
- [111] Nestor SM, Rupsingh R, Borrie M, et al. Ventricular enlargement as a possible measure of Alzheimer’s disease progression validated using the Alzheimer’s disease neuroimaging initiative database. *Brain*. 2008;131(9):2443–2454.
- [112] Goerke S, Breitling J, Kubera KM, et al. Protein-sensitive CEST-MRI of Alzheimer’s patients at 3 T. In: Proceedings of the 28th Annual Meeting of the International Society for Magnetic Resonance in Medicine. Paris, France; 2020.

List of Scientific Contributions

Journal articles

Korzowski, Andreas; Weinfurtner, Nina; Mueller, Sebastian; **Breitling, Johannes**; Goerke, Steffen; Schlemmer, Heinz-Peter; Ladd, Mark E.; Paech, Daniel and Bachert, Peter: Volumetric Mapping of Intra- and Extracellular pH in the Human Brain using ^{31}P MRSI at 7 T. *Magnetic Resonance in Medicine*. 2020. doi:10.1002/mrm.28255.

Breitling, Johannes; Meissner, Jan-Eric; Zaiss, Moritz; Paech, Daniel; Ladd, Mark E.; Bachert, Peter and Goerke, Steffen: Optimized dualCEST-MRI for imaging of endogenous bulk mobile proteins in the human brain. *NMR in Biomedicine*. 2020;33:4262.

Boyd, Philip S.; **Breitling, Johannes**; Zimmermann, Ferdinand; Korzowski, Andreas; Zaiss, Moritz; Schuenke, Patrick; Weinfurtner, Nina; Schlemmer, Heinz-Peter; Ladd, Mark E.; Bachert, Peter; Paech, Daniel and Goerke, Steffen: Dynamic Glucose-Enhanced (DGE) MRI in the human brain at 7 T with reduced motion-induced artifacts based on quantitative $R_{1\rho}$ mapping. *Magnetic Resonance in Medicine*. 2020;84:182–191.

Zimmermann, Ferdinand; Korzowski, Andreas; **Breitling, Johannes**; Meissner, Jan-Eric; Schuenke, Patrick; Loi, Lisa; Zaiss, Moritz; Bickelhaupt, Sebastian; Schott, Sarah; Schlemmer, Heinz-Peter; Paech, Daniel; Ladd, Mark E.; Bachert, Peter and Goerke, Steffen: A novel normalization for APT-CEST MRI to correct for fat-signal-induced artifacts — application to human breast cancer imaging. *Magnetic Resonance in Medicine*. 2020;83:920–934.

Breitling, Johannes; Deshmane, Anagha; Goerke, Steffen; Korzowski, Andreas; Herz, Kai; Ladd, Mark E.; Scheffler, Klaus; Bachert, Peter and Zaiss, Moritz: Adaptive denoising for chemical exchange saturation transfer MR imaging. *NMR in Biomedicine*. 2019;32:e4133.

Goerke, Steffen; Soehngen, Yannick; Deshmane, Anagha; Zaiss, Moritz; **Breitling, Johannes**; Boyd, Philip S.; Herz, Kai; Zimmermann, Ferdinand; Klika, Karel D.; Schlemmer, Heinz-Peter; Paech, Daniel; Ladd, Mark E. and Bachert, Peter: Relaxation-compensated APT and rNOE CEST-MRI of human brain tumors at 3 T. *Magnetic Resonance in Medicine*. 2019;82:622–632.

Meissner, Jan-Eric; Korzowski, Andreas; Regnery, Sebastian; Goerke, Steffen; **Breitling, Johannes**; Floca, Ralf O.; Debus, Jürgen; Schlemmer, Heinz-Peter; Ladd, Mark E.; Bachert, Peter; Adeberg, Sebastian and Paech, Daniel: Early Response Assessment of

Glioma Patients to Definitive Chemoradiotherapy Using Chemical Exchange Saturation Transfer Imaging at 7 T. *Journal of Magnetic Resonance Imaging*. 2019;50:1268-1277.

Goerke, Steffen; **Breitling, Johannes**; Zaiss, Moritz; Windschuh, Johannes; Kunz, Patrick; Schuenke, Patrick; Paech, Daniel; Longo, Dario L.; Klika, Karel D.; Ladd, Mark E. and Bachert, Peter: Dual-frequency irradiation CEST-MRI of endogenous bulk mobile protons. *NMR in Biomedicine*. 2018;31:e3920.

Conference and workshop contributions

Breitling, Johannes; Goerke, Steffen; Ladd, Mark E.; Bachert, Peter and Korzowski, Andreas: Two-stage denoising of CEST MRI data by principal component analysis of spectral groups. *Proceedings of the 28th Annual Meeting of the International Society for Magnetic Resonance in Medicine, Paris, France 2020*; Abstract #453.

Goerke, Steffen; **Breitling, Johannes**; Kubera, Katharina M.; Zaiss, Moritz; Hirjak, Dusan; Wolf, Robert C.; Tavakoli, Anoshirwan A.; Schlemmer, Heinz-Peter; Paech, Daniel; Ladd, Mark E. and Bachert, Peter: Protein-sensitive CEST-MRI of Alzheimer's patients at 3 T. *Proceedings of the 28th Annual Meeting of the International Society for Magnetic Resonance in Medicine, Paris, France 2020*; Abstract #40.

Boyd, Philip S.; **Breitling, Johannes**; Ladd, Mark E.; Bachert, Peter and Goerke, Steffen: Concentration-independent absolute pH mapping using amide CEST-MRI at 9.4 T. *Proceedings of the 28th Annual Meeting of the International Society for Magnetic Resonance in Medicine, Paris, France 2020*; Abstract #4889.

Korzowski, Andreas; **Breitling, Johannes**; Franke, Vanessa L.; Ladd, Mark E. and Bachert, Peter: Accelerating volumetric ³¹P MRSI of the human calf muscle at 7 Tesla: can low-rank denoising filters replace the need for signal averaging?. *Proceedings of the 28th Annual Meeting of the International Society for Magnetic Resonance in Medicine, Paris, France 2020*; Abstract #3720.

Loi, Lisa; Zimmermann, Ferdinand; Korzowski, Andreas; Meissner, Jan-Eric; **Breitling, Johannes**; Bachert, Peter; Ladd, Mark E.; Schlemmer, Heinz-Peter; Schott, Sarah; Bickelhaupt, Sebastian; Goerke, Steffen and Paech, Daniel: Investigating the dependence of APT-CEST imaging in the human breast at 7 Tesla on the menstrual cycle. *Proceedings of the 28th Annual Meeting of the International Society for Magnetic Resonance in Medicine, Paris, France 2020*; Abstract #5940.

Meissner, Jan-Eric; Korzowski, Andreas; Regnery, Sebastian; Goerke, Steffen; **Breitling, Johannes**; Debus, Jürgen; Schlemmer, Heinz-Peter; Ladd, Mark E.; Bachert, Peter; Adeb-berg, Sebastian and Paech, Daniel: Nuclear-Overhauser-Effekt (NOE) CEST MRT ermöglicht frühe Beurteilung des Therapieansprechens bei Gliompatienten. *Proceedings of the 50th Annual Scientific Meeting DGMP, Stuttgart, Germany 2019*; Oral presentation #58.

Meissner, Jan-Eric; **Breitling, Johannes**; Zimmermann, Ferdinand; Goerke, Steffen; Korzowski, Andreas; Zaiss, Moritz; Ladd, Mark E. and Bachert, Peter: FullHD CEST Bildgebung des Gehirns bei 7T. *Proceedings of the 50th Annual Scientific Meeting DGMP, Stuttgart, Germany* 2019; Poster #79.

Breitling, Johannes; Deshmane, Anagha; Goerke, Steffen; Herz, Kai; Ladd, Mark E.; Scheffler, Klaus; Bachert, Peter and Zaiss, Moritz: Denoising of Z-spectra for stable CEST MRI using principal component analysis. *Proceedings of the 27th Annual Meeting of the International Society for Magnetic Resonance in Medicine, Montreal, Canada* 2019; Power Pitch Poster #0143.

Zimmermann, Ferdinand; Korzowski, Andreas; Loi, Lisa C.; **Breitling, Johannes S**; Meissner, Jan-Eric; Zaiss, Moritz; Bickelhaupt, Sebastian; Schlemmer, Heinz-Peter; Ladd, Mark E.; Bachert, Peter; Paech, Daniel; Schott, Sarah and Goerke, Steffen: Fat corrected APT-CEST in the human breast at 7 Tesla: application to mamma carcinoma and dependency on menstrual cycle. *Proceedings of the 27th Annual Meeting of the International Society for Magnetic Resonance in Medicine, Montreal, Canada* 2019; Power Pitch Poster #0148.

Boyd, Philip S.; **Breitling, Johannes**; Zimmermann, Ferdinand; Korzowski, Andreas; Zaiss, Moritz; Schuenke, Patrick; Weinfurter, Nina; Schlemmer, Heinz-Peter; Ladd, Mark E.; Bachert, Peter; Paech, Daniel and Goerke, Steffen: Acquisition protocol for glucoCESL MRI in the human brain at 7T with reduced motion-induced artifacts. *Proceedings of the 27th Annual Meeting of the International Society for Magnetic Resonance in Medicine, Montreal, Canada* 2019; Poster #5009.

Goerke, Steffen; Soehngen, Yannick; Deshmane, Anagha; Zaiss, Moritz; **Breitling, Johannes**; Boyd, Philip S.; Herz, Kai; Zimmermann, Ferdinand; Klika, Karel D.; Ladd, Mark E. and Bachert, Peter: Relaxation-compensated APT and rNOE CEST-MRI of human brain tumors at 3 T. *Proceedings of the 27th Annual Meeting of the International Society for Magnetic Resonance in Medicine, Montreal, Canada* 2019; Poster #4013.

Korzowski, Andreas; Weinfurter, Nina; Mueller, Sebastian; **Breitling, Johannes**; Goerke, Steffen; Schlemmer, Heinz-Peter; Ladd, Mark E.; Paech, Daniel and Bachert, Peter: Volumetric mapping of intra- and extracellular pH in glioma patients using 31P MRSI at 7 Tesla. *Proceedings of the 27th Annual Meeting of the International Society for Magnetic Resonance in Medicine, Montreal, Canada* 2019; Power Pitch Poster #0485.

Breitling, Johannes; Goerke, Steffen; Zaiss, Moritz, Soehngen, Yannick; Deshmane, Anagha; Herz, Kai; Boyd, Philip; Ladd, Mark E. and Bachert, Peter: Optimized dualCEST-MRI for imaging of endogenous bulk mobile proteins in the human brain. *Proceedings of the 7th International Workshop on Chemical Exchange Saturation Transfer Imaging, Beijing, China* 2018; Poster #4.

Zimmermann, Ferdinand; Korzowski, Andreas; Schuenke, Patrick; **Breitling, Johannes**; Zaiss, Moritz; Paech, Daniel; Ladd, Mark E.; Bachert, Peter and Goerke, Steffen: Fat corrected APT-CEST in the human breast. *Proceedings of the 7th International Workshop on Chemical Exchange Saturation Transfer Imaging, Beijing, China* 2018; Oral presentation.

List of Scientific Contributions

Meissner, Jan-Eric; **Breitling, Johannes**; Zimmermann, Ferdinand; Goerke, Steffen; Korzowski, Andreas; Zaiss, Moritz; Ladd, Mark E. and Bachert, Peter: FullHD CEST imaging in the human brain at 7T. *Proceedings of the 7th International Workshop on Chemical Exchange Saturation Transfer Imaging, Beijing, China* 2018; Poster #6.

Breitling, Johannes; Goerke, Steffen; Meissner, Jan-Eric; Korzowski, Andreas; Schuenke, Patrick; Ladd, Mark E. and Bachert, Peter: Steady-state CEST-MRI using a reduced saturation period. *Proceedings of the Joint Annual Scientific Meeting ISMRM-ESMRMB, Paris, France* 2018; Poster #2240.

Zimmermann, Ferdinand; Korzowski, Andreas; Schuenke, Patrick; **Breitling, Johannes**; Ladd, Mark E.; Bachert, Peter and Goerke, Steffen: A novel normalization to correct APT-CEST in the presence of fat. *Proceedings of the Joint Annual Scientific Meeting ISMRM-ESMRMB, Paris, France* 2018; Poster #2222.

Goerke, Steffen; **Breitling, Johannes**; Klika, Karel D.; Ladd, Mark E. and Bachert, Peter: Dependence of rNOE-CEST signals on molecular weight. *Proceedings of the Joint Annual Scientific Meeting ISMRM-ESMRMB, Paris, France* 2018; Poster #2228.

Goerke, Steffen; Zaiss, Moritz; Longo, Dario L.; Garello, Francesca; Di Gregorio, Enza; **Breitling, Johannes**; Ladd, Mark E. and Bachert, Peter: CEST Signals of Lipids. *Proceedings of the 25th Annual Meeting of the International Society for Magnetic Resonance in Medicine, Honolulu, USA* 2017; Oral presentation #0201.

Zimmermann, Ferdinand; Goerke, Steffen; **Breitling, Johannes**; Klopries, Kerstin; Windschuh, Johannes; Schlemmer, Heinz-Peter; Ladd, Mark E.; Paech, Daniel and Bachert, Peter: Correction of fat artifacts for unbiased CEST-MRI of the human breast at 7T. *Proceedings of the 25th Annual Meeting of the International Society for Magnetic Resonance in Medicine, Honolulu, USA* 2017; Poster #3757.

Breitling, Johannes; Goerke, Steffen; Longo, Dario; Klika, Karel D.; Ladd, Mark E. and Bachert, Peter: Corrected dualCEST signal enables the unbiased detection of proteins in vivo. *Proceedings of the 58th Experimental Nuclear Magnetic Resonance Conference, Pacific Grove, USA* 2017; Poster #204.

Breitling, Johannes; Goerke, Steffen; Zaiss, Moritz; Windschuh, Johannes; Klika, Karel D. and Bachert, Peter: Inhomogeneous magnetization transfer detection by dual frequency CEST spectroscopy. *Proceedings of the 33rd Annual Scientific Meeting of the European Society for Magnetic Resonance in Medicine and Biology, Vienna, Austria* 2016; *Magnetic Resonance Materials in Physics, Biology and Medicine* 2016;29:265-266.

Acknowledgements

A PhD is not something that happens in a vacuum, but rather involves the work and help of many people. I would like to take this opportunity to thank everyone who supported me during this time and made it a great experience.

First and foremost, I would like to thank you, Prof. Bachert, for giving me the chance to continue my academic journey and remain part of your research group. Your trust and endless support allowed me to explore my own projects and ideas, and at the same time I knew I could always ask for your scientific expertise if needed. Thank you.

Furthermore, I would like to thank Prof. Schad for taking the time and kindly accepting to be the second referee for my dissertation.

Steffen, I will never be able to thank you enough for the past five years. You've been the starting point of this whole journey by letting me in on the fascinating concept of two-dimensional CEST. Thank you for always being there, whether it was as an inspiration, support, critic, motivator, mentor, or friend. And thank you for basically teaching me everything I know about illustrating, presenting, and writing down scientific concepts. Thank you.

A special thanks belongs to all current and former colleagues: in particular, Andi, Jan, Ferdi, Dominik, Sarah, Vanessa, Philip, Joe, Patrick, Johnny, and Moritz. Each and every one of you made DKFZ so much more than just a workplace. By now, I have realized that such a beautiful, relaxed, and at the same time fruitful working atmosphere is not something which should be taken for granted. I am more than grateful to have been able to work with all of you guys.

I would like to express my deep gratitude to the International Max-Planck Research school for Quantum Dynamics for financially supporting me throughout my studies and providing me with many opportunities for presenting and discussing my research project.

And now to all my friends, whether I met them at home, university, scouts, or somewhere else. Thank you for reminding me every now and then that there is more to life than just work and science.

Finally, I would like to thank my parents and family for the never-ending support and encouragement to always pursue my dreams. And Rachel, thank you for coming into my life. It seems like sometimes you have to travel to the other side of the world to find what you were missing all along.

Thank you

Johannes

Easter 2020, Heidelberg during the Covid-19 lockdown